Generation and fiber-based distribution of high-bandwidth entanglement for continuous variable quantum key distribution

Dissertation
zur Erlangung des Doktorgrades
an der Fakultät für Mathematik, Informatik und Naturwissenschaften
Fachbereich Physik
der Universität Hamburg

vorgelegt von

Benedict Tohermes

Hamburg

2025

Gutachter/innen der Dissertation:	Prof. Dr. Roman Schnabel Prof. Dr. Oliver Gerberding
Zusammensetzung der Prüfungskommission:	Prof. Dr. Ludwig Mathey Prof. Dr. Roman Schnabel Prof. Dr. Oliver Gerberding Prof. Dr. Peter Schauss Prof. Dr. Dieter Jaksch
Vorsitzende/r der Prüfungskommission:	Prof. Dr. Ludwig Mathey
Datum der Disputation:	17.10.2025
Vorsitzender Fach-Promotionsausschuss PHYSIK:	Prof. Dr. Wolfgang J. Parak
Leiter des Fachbereichs PHYSIK:	Prof. Dr. Markus Drescher
Dekan der Fakultät MIN:	Prof. Dr.-Ing. Norbert Ritter

Abstract

Entanglement is a key resource in many quantum information tasks, from quantum computing to quantum key distribution. In quantum key distribution in particular, use of entanglement enables protocols that are one-sided device independent. The source of its security are the inability to clone a quantum state as stated by the no-cloning theorem, as well as that the entanglement strength monotonically decreases if information is lost. The total decoherence experienced by the entangled state places an upper bound on the information an adversary could have gained while eavesdropping. Use of high bandwidth entangled states increases the key rate of such a protocol.

During this thesis I investigated the feasibility of distributing a continuous variable Einstein-Podolski-Rosen entangled state over a noisy channel for use in a one-sided device independent quantum key distribution protocol in an applied setting. To maximize the potential data rate I designed and set up two GHz bandwidth homodyne detectors as well as two GHz bandwidth monolithic squeezed light sources which constituted the entanglement source. The squeezed light sources individually produced states exhibiting a noise reduction of up to 6.5 dB compared to shot noise at 30 MHz and 2.9 dB at a frequency above 1 GHz. By combining the two squeezed states I produced an entangled state that showed a 4.2 dB reduced variance relative to the combined shot noise of the measured light. This allowed to infer a violation of the EPR-Reid criterion. I distributed the entangled state between two separate buildings on campus via a 1 km long optical fiber link. Transmitting one part of the entangled state through the fiber link, the entanglement showed little degradation. The peak relative noise reduction remained at up to 3.7 dB below the combined shot noise over a 10 MHz wide frequency band. I used this band to generate a raw key pair at 336 kbit s^{-1}. Additionally, a 250 MHz wide frequency band remained free of other noise sources at more than 2.0 dB below combined shot noise. Improving the initial squeezing factor of both sources can extend the violation of the EPR-Reid criterion to this band, enabling its use for key generation and thus increasing the key rate.

This result demonstrates the viability of a continuous variable quantum key distribution protocol based on two-mode squeezed states in the presence of typical environmental noise sources. Stabilizing the readout quadrature would further increase the raw key rate to 50 Mbit s^{-1}.

Kurzfassung

Verschränkung bildet eine der zentralen Resourcen der Quanteninformation, mit Anwendungen in Quantencomputern und Quantenschlüsselverteilung. Besonders in der Quantenschlüsselverteilung ermöglicht der Einsatz von Verschränkung einseitig geräteunabhängige Protokolle. Ursprung dieser erhöhten Sicherheit ist, dass die Stärke der Verschränkung monoton mit Informationsverlust abnimmt, sowie das No-Cloning Theorem, welches es verbietet eine exakte Kopie eines beliebigen Quantenzustands zu erzeugen. Die Gesamtdekohärenz der verschränkten Zustände setzt eine obere Grenze für die Information, die bei einem Abhörversuch erlangt worden sein kann. Die Schlüsselrate dieser Protokolle skaliert dabei mit der Bandbreite der Verschränkung.

In dieser Doktorarbeit untersuchte ich die Realisierbarkeit der Verteilung eines Einstein-Podolski-Rosen verschränkten Zustands über einen realen rauschbehafteten Kanal. Der explizite Schwerpunkt lag auf der Verwendung der Zustands in einem einseitig geräteunabhängigen Quantenschlüsselverteilungsprotokol. In dieser Zeit entwarf ich zwei Quetschlichtquellen, die den verschränkten Zustand erzeugten, sowie zwei Homodyndetektoren, um diesen zu vermessen. Dabei wählte ich die Bandbreite von Lichtquellen und Detektoren im GHz Bereich, um die erreichbare Schlüsselrate zu maximieren. Einzeln vermessen produzierten die Quetschlichtquellen Zustände mit einem reduzierten Quantenrauschen von bis zu 6.5 dB unter dem Schrotrauschen bei 30 MHz Seitenbandfrequenz, sowie eine Reduktion von 2.9 dB über 1 GHz Seitenbandfrequenz. Durch Überlagerung der beiden gequetschten Zustände erzeugte ich einen verschränkter Zustand, der eine Varianz von 4.2 dB unter dem kombinierten Schrotrauschen des gemessenen Lichts erreichte. Daraus konnte ich eine Veletzung des EPR-Reid Kriteriums ableiten. Den verschränkte Zustand verteilte ich zwischen zwei unterschiedlichen Gebäuden auf dem Campus mittels einer 1 km langen optischen Glasfaser. Nach der Transmission durch die Faser sank der Spitzenwert auf 3.7 dB, gemessen über ein 10 MHz breites Frequenzband. Dieses Frequenzband nutzte ich, um einen Rohschlüssel mit einer Rohschlüsselrate von 336 kbit s^{-1} zu generieren. Ein weiteres 250 MHz breites Frequenzband zeigte eine Varianz von mehr als 2.0 dB unter dem kombinierten Schrotrauschen. Ein höherer initialer Quetschfaktor kann eine Verletzung des EPR-Reid Kriterium in diesem Frequenzband ermöglichen. Dies würde das Frequenzband zusätzlich für die Schlüsselgenerierung eröffnen und so die Schlüsselrate zu erhöhen.

Die Ergebnisse dieser Arbeit demonstrieren die Umsetzbarkeit eines Quantenschlüsselverteilungsprotokolls basierend auf Zwei-Moden gequetschten Zuständen in einer verrauschten Umgebung. Durch Stabilisierung der Auslesequadratur kann die Rohschlüsselrate weiter auf bis zu 50 Mbit s^{-1} erhöht werden.

Contents

Acronyms

CV continuous variable

DAQ data acquisition

DV discrete variable

EOM electro-optic modulator

EPR Einstein-Podolsky-Rosen

FFT fast Fourier transform

FSR free spectral range

GKP Gottesman-Kitaev-Preskill

IQP Institut für Quantenphysik

KTP potassium titanyl phosphate

LO local oscillator

NTC negative temperature coefficient

OsDI one-sided device independent

PCB printed circuit board

PDC parametric down-conversion

PDH Pound-Drever-Hall

PID proportional-integral-derivative

PPKTP periodically-poled potassium titanyl phosphate

QKD quantum key distribution

QRNG quantum random number generator

RNG random number generator

RoC radius of curvature

SHG second-harmonic generation

ZOQ Zentrum für optische Quantentechnologien

Pictogram glossary


Photodiode


Piezo driven mirror / phase shifter


Polarizing beam splitter


Dichroic beam splitter


Half wave plate

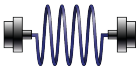
Optical fiber


Beam block


Laser

PID controller


Electro-optic modulator


Frequency generator


Frequency mixer


Low-pass filter

Coherent light

Squeezed light / vacuum state

1550 nm light

775 nm light

Chapter 1

Introduction

Cryptography, the task of transmitting a message while keeping other parties from accessing it, is a topic that has occupied humanity throughout history, with early reported examples dating back to ancient Rome and Greece around 600 BC and even earlier. In modern times it has become more relevant than ever with the rise of the internet, as vast amounts of messages are being sent every second. Hybrid cryptosystems form the backbone of internet traffic. They consist of a public-key step to establish a shared secret between two parties for later use in a symmetric-key algorithm that encrypts the bulk of the communication. The security of current public-key cryptosystems is based on computationally hard problems, making message decryption by an adversary within a reasonable time frame unlikely. However, development of a large enough quantum computer running Shor's algorithm [Sho94] would be able to break the security offered by currently implemented public-key cryptosystems.

The ever increasing computing power of classical computers, as well as advances in scaling the size and improving the fault tolerance of quantum computers have led to increased interest in the development of quantum safe encryption methods [Aru19; Zho20]. While the security of symmetric-key algorithms is impacted less by quantum computers, a post-quantum scenario requires a new solution to establish a shared secret.

Research is being conducted in the direction of classical-computation based post-quantum cryptosystems. However, the field of quantum key distribution (QKD) offers an approach that allows for information-theoretically secure communication without placing bounds on the computation power of an adversary. Its security is based on quantum mechanical principles in combination with a one-time pad encryption scheme. QKD is based on the transmission of a quantum state over an unsafe quantum channel, typically an optical fiber or free space. The important principles of quantum mechanics that make such a protocol secure are: 1. A measurement of a quantum state disturbs it and 2. It is impossible to create an independent and identical copy of an arbitrary quantum state (no-cloning theorem). An eavesdropper who tries to gain information by performing a measurement on the quantum state necessarily announces their presence. In the case an eavesdropper's presence is detected by the

protocol, distributed keys can be discarded to ensure security.

The earliest QKD protocol (BB84) was proposed by Bennett and Brassard in 1984 based on discrete variable (DV) quantum states, polarized single photons [Ben14]. Further research in the following years lead to the development of many types of protocols that can be categorized by the type of distributed quantum states into DV protocols measuring discrete properties of a quantum state and continuous variable (CV) protocols, where information is encoded in or generated from some continuous property of the light field, e.g. quadrature amplitudes. QKD protocols can further be categorized by the security assumptions: Utilizing entangled states to perform a Bell test enables a device-independent protocol, where the correct working of the entanglement source and detection devices is ensured in the security proof. The downside to this is that performing a loophole-free Bell test is challenging and leads to lower overall key rates. Additionally, performing a Bell test with CV states is hard to achieve, requiring non-Gaussian operations [Wal16]. However, one can formulate a one-sided device-independent protocols, which relies on a less strict criterion, the EPR-Reid criterion, that is independent of devices on the receiver side. While this is a step down in security compared to a fully device independent protocol, it is more robust to side channel attacks and comes with a higher secret key rate potential.

The overall secret key rate of a QKD protocol can be modeled as the product of the amount of information transmitted per channel use and the channel bandwidth [Pir17]. Information per channel use typically scales inversely with lessened security assumptions, i.e. device independence, and is bounded by channel loss, most prominently introduced by transmission distance. The easiest way to increase the overall secret key rate of a protocol is thus to increase the channel bandwidth, e.g. by increasing the bandwidth of the entangled states.

In this thesis I focused on a one-sided device independent CV protocol described in [Fur12]. It can be implemented using a two-mode squeezed state — a CV entangled state that can be generated and detected with a high bandwidth — resulting in a high rate of raw samples for key generation. Setting up a source of high-bandwidth two-mode squeezed states was the first main goal of this thesis.

The protocol can only achieve one-sided device independence if the total detection loss, including transmission loss in the quantum channel, is less than 50 %, a consequence of the EPR-Reid criterion. Current optical fiber technology places a limit on the maximum distance on the scale of a few kilometers. Despite this limitation, its high bandwidth potential makes this protocol an attractive solution for a quantum network in a government district or a computing cluster.

Bringing this protocol to a close-to-application setting comes with additional challenges. A previous setup implemented the quantum channel as a fiber spooled up in the same laboratory, thus remaining in a low-noise and temperature controlled environment [Geh13]. This thesis brings the protocol one step closer to a real world

implementation by connecting two different buildings on campus via a 1 km long fiber link, of which approx. 100 m have been deployed in a noisy environment. Detection of the two-mode squeezed state was the second main goal of this thesis. Combined with the previous works of [Geh13], which implement additional steps that make the protocol secure, this demonstrates the viability of the CV QKD protocol in an applied setting.

Chapter 2

Theoretical background

Entanglement in the form of optical two-mode squeezed states comprised the core of this experiment. In the following chapter I give a theoretical description of them and how they can be produced in a nonlinear optical cavity.

I will first review the classical description of an optical cavity, deriving the quantities I considered when designing the nonlinear cavity in Ch. 2.1. This is followed by the quantum mechanical description of the most important states for this experiment — coherent states, squeezed states, and two-mode squeezed states — and how they can be detected in Ch. 2.2 and 2.3. I then briefly discuss nonlocality criteria for entanglement and how they can be utilized for quantum key distribution in Ch. 2.4. Lastly, I give a description of the two nonlinear effects that were relevant for this thesis in Ch. 2.5

2.1 Optical cavity

An essential component for the setup of this experiment is the optical cavity. Here I give a classical description that will adhere closely to what can be found in [Bac04]. I will derive the most important quantities needed to describe the cavities found in the experiment.

An optical cavity consists of a set of two or more mirrors with power reflectivity R_j (transmissivity T_j) that are placed such that an incident beam transmitted through one mirror gets reflected back onto itself after propagating inside the cavity for one (or more) round trip. There are two classes of cavities: Linear cavities and ring cavities. A linear cavity is formed by placing two mirrors along one optical axis. One property of this configuration is that a beam which is reflected at the first mirror (the coupling mirror) overlaps spatially with the incoming beam. If access to the reflected beam is desired, a ring cavity can be used. It is formed by three or more mirrors such that the light inside the cavity travels on a ring path. The two configurations are illustrated in Fig. 2.1.

Light transmitted through the first mirror interferes with light that has circulated inside the cavity and is reflected at the first mirror. The circulating light can be represented by multiple partial waves, one from each round trip. Each partial wave

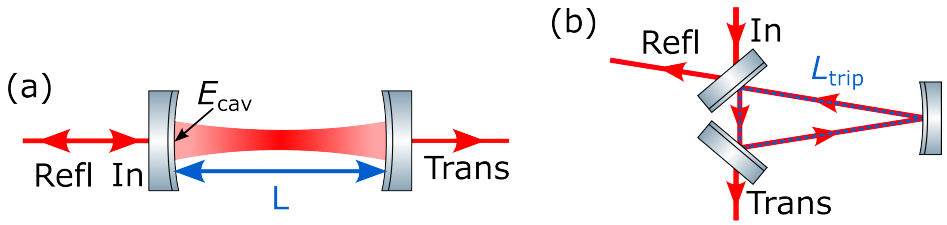

Figure 2.1: (a) Linear cavity and (b) ring cavity.

experiences amplitude loss from transmissivity of the mirrors and from power absorption $e^{-\alpha_{trip}}$, which is useful to combine as a gain factor

$$g^2 = e^{-\alpha_{trip}} \prod_j R_j \tag{2.1}$$

per round trip.

A side note: For a classical cavity this factor is smaller than 1. The name 'gain factor' becomes more reasonable for a non-linear cavity that also produces or converts some electric field per round trip in this mode. Here the gain factor gets modified to include an additional factor to account for the produced field and can become larger than 1.

The electric field at the coupling mirror E_{cav} is given by the sum of those partial waves

$$\begin{aligned} E_{cav} &= \sqrt{T_1} E_0 (\underbrace{1}_{\text{incident wave}} + \underbrace{g e^{i\phi_{trip}}}_{\text{first round trip}} + \underbrace{g^2 e^{i2\phi_{trip}}}_{\text{second round trip}} + \dots) \\ &= \sqrt{T_1} E_0 \sum_{n=0}^{\infty} \left(g e^{i\phi_{trip}} \right)^n \\ &= \frac{\sqrt{T_1} E_0}{1 - g e^{i\phi_{trip}}} \qquad \text{for } g < 1, \end{aligned} \tag{2.2}$$

with the amplitude of the incident electric field E_0. Each partial wave accrues a phase ϕ_{trip} per round trip. The cavity is resonant when all partial waves interfere constructively with each other and the incident light. This is the case when ϕ_{trip} is equal to an integer multiple m of 2π. Neglecting phase shifts at the mirror, this is the case when the length per round trip L_{trip} is a multiple of the light's wavelength in vacuum λ_0. In the presence of a medium, the round trip length is modified by the medium's refractive index n such, that the condition becomes

$$L_{trip} = \frac{m\lambda_0}{n} \tag{2.3}$$

or expressed as frequencies of the incident light ν_{res} for which the cavity is resonant

$$\nu_{\mathrm{res}} = \frac{mc}{nL_{\mathrm{trip}}}. \tag{2.4}$$

The resonance condition can be achieved by changing either the cavity length or the light's frequency ν such that it matches the cavity's resonance frequency. When changing the light's frequency, the distance between two longitudinal resonances is called one free spectral range (FSR)

$$\nu_{\mathrm{FSR}} = \frac{c}{nL_{\mathrm{trip}}}. \tag{2.5}$$

In the special case of a linear cavity, the round trip length is twice the mirror separation L so that the FSR is $\frac{c}{2nL}$.

The in-phase interference of incident and circulating light leads to a power buildup inside the cavity. On resonance the power inside the cavity is

$$P_{\mathrm{res}} = \left(\frac{\sqrt{T_1}E_0}{1-g}\right)^2. \tag{2.6}$$

It is reduced by the light lost per round trip and scaling proportionally to the power $T_1 E_{0,\mathrm{in}}^2$ transmitted into the cavity through the coupling mirror. Changing the light's frequency ν continuously around the cavity resonance, the intra cavity power follows a Lorentzian shape

$$P = \frac{P_{\mathrm{res}}}{1+(2\mathcal{F}/\pi)^2 \sin^2(\pi\nu/\nu_{\mathrm{res}})}, \tag{2.7}$$

which is visualized in Fig. 2.2. Here $\mathcal{F}$ is the cavity's finesse, which is often defined as the ratio of linewidth to FSR

$$\mathcal{F} = \frac{\nu_{\mathrm{FSR}}}{\delta\nu} = \frac{\pi\sqrt{g}}{1-g} \tag{2.8}$$

and can be interpreted as an optical analog to the quality factor of a mechanical oscillator.

The gain factor g limits the amplitude of the partial waves that interfere and determines how fast the series from Eq. 2.2 converges. Depending on the gain a small deviation of the phase shift per round trip from $2\pi m$ still results in a buildup of an electric field inside the cavity. Thus, frequencies with a small deviation from a resonance frequency can still couple into the cavity at reduced amplitude due to destructive interference of the partial waves. When scanning the light's frequency this becomes visible as a broadening of the resonance peak with increasing losses. The cavity's linewidth $\delta\nu$ is commonly measured as the full width at half maximum

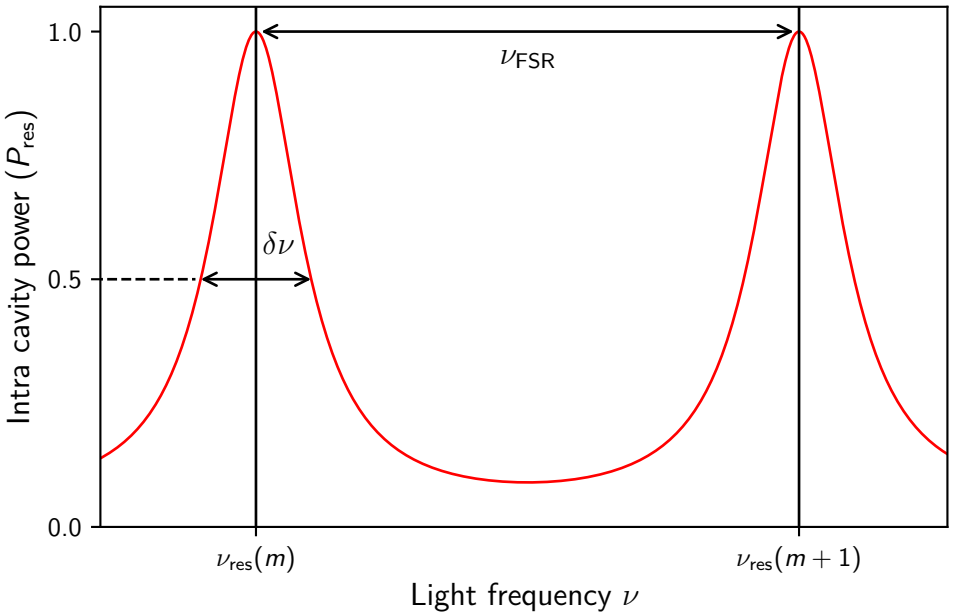

Figure 2.2: Cavity resonance when scanning the incident lights frequency for a cavity finesse of $\mathcal{F} = 14$. Also indicated are the cavity linewidth and the length of one FSR.

of the resonance peak. Calculating it from the finesse and free spectral range via Eq. 2.8 gives

$$\delta\nu = \frac{c(1-g)}{\pi n \sqrt{g} L_{\text{trip}}}. \tag{2.9}$$

This expression captures the case we observed here, i.e. that the linewidth becomes small in the lossless case with high reflectivities ($g \simeq 1$), and broadens for lower reflectivities.

2.2 Quantum mechanical description of light

In the following I want to give a brief quantum mechanical description of the electromagnetic field which will follow chapter 2 from [Ger05]. It covers the basic quantum states used to describe my experiment.

2.2.1 Creation & annihilation operators and number states

We start the derivation with the Maxwell equations:

$$\begin{aligned} \nabla \cdot D &= \rho, \\ \nabla \cdot B &= 0, \\ \nabla \times E &= -\frac{\partial B}{\partial t}, \\ \nabla \times H &= \frac{\partial D}{\partial t} + J, \end{aligned} \tag{2.10}$$

which we consider in the sourceless case, i.e. $\rho = 0$ and $J = 0$, where $D = \epsilon_0 E$, and $B = \mu_0 H$, with the electric field E, the magnetic field B, the vacuum permittivity ϵ_0 and permeability μ_0, and the speed of light $c = \frac{1}{\sqrt{\epsilon_0 \mu_0}}$. Next let us consider a light field that is confined to an optical cavity formed between two perfectly conducting mirrors. We assume the optical axis of this cavity is located along the z-axis and only consider a light field with an electric field polarized along the x-axis. The cavity imposes the boundary condition that the electric field is 0 at the mirror surfaces. One solution for an electric field that satisfies the Maxwell equations as well as the boundary condition is the mode

$$E_x(z,t) = \left(\frac{2\omega^2}{V\epsilon_0}\right)^{1/2} q(t)\sin(kz)\hat{e}_x, \tag{2.11}$$

$$B_y(z,t) = \frac{\mu_0\epsilon_0}{k}\left(\frac{2\omega^2}{V\epsilon_0}\right)^{1/2} p(t)\cos(kz)\hat{e}_y, \tag{2.12}$$

with the frequency of the mode $\omega = 2\pi\nu$ and the corresponding wave vector $k = \frac{\omega}{c}$, the effective volume of the cavity V, and the unit vectors $\hat{e}_x, \hat{e}_y$. $q(t)$ acts as a canonical position and $p(t) = \dot{q}(t)$ as a canonical momentum. The classical field energy of this mode is given by the Hamiltonian H according to

$$\begin{aligned} H &= \frac{1}{2}\int dV \left[\epsilon_0 E_x^2(z,t) + \frac{1}{\mu_0} B_y^2(z,t)\right] \\ &= \frac{1}{2}(p^2 + \omega^2 q^2), \end{aligned} \tag{2.13}$$

which assumes the same form as that of a harmonic oscillator. In order to quantize the Hamiltonian we can replace the canonical variables p and q by their operator equivalents $\hat{p}$ and $\hat{q}$ which satisfy the commutation relation $[\hat{q}, \hat{p}] = i\hbar$. With this the Hamiltonian of the mode inside the resonator becomes

$$\hat{H} = \frac{1}{2}(\hat{p}^2 + \omega^2 \hat{q}^2). \tag{2.14}$$

In full analogy to the harmonic oscillator we can introduce the creation and annihilation operators $\hat{a}^\dagger$ and $\hat{a}$ defined in terms of the canonical position and momentum as

$$\begin{aligned}\hat{a} &= \frac{1}{\sqrt{2\hbar\omega}}(\omega\hat{q} + i\hat{p}),\\ \hat{a}^\dagger &= \frac{1}{\sqrt{2\hbar\omega}}(\omega\hat{q} - i\hat{p}).\end{aligned} \tag{2.15}$$

These satisfy the commutation relation $[\hat{a}, \hat{a}^\dagger] = 1$. With these operators we can define the field operators from their classical counterparts from Eqs. 2.11 and 2.12 as

$$\hat{E}_x(z,t) = \mathcal{E}_0(\hat{a} + \hat{a}^\dagger)\sin(kz), \tag{2.16}$$

$$\hat{B}_y(z,t) = \mathcal{B}_0\frac{1}{i}(\hat{a} - \hat{a}^\dagger)\cos(kz), \tag{2.17}$$

where $\mathcal{E}_0 = \sqrt{\frac{\hbar\omega}{\epsilon_0 V}}$ and $\mathcal{B}_0 = \frac{\mu_0}{k}\sqrt{\frac{\epsilon_0\hbar\omega^3}{V}}$. With these, the Hamiltonian from Eq. 2.14 becomes

$$\hat{H} = \hbar\omega\left(\hat{a}^\dagger\hat{a} + \frac{1}{2}\right). \tag{2.18}$$

The physical meaning of these operators becomes clearer when considering them acting on eigenstates of the Hamiltonian. For an energy eigenstate $|n\rangle$ the eigenvalue equation reads

$$\hat{H}|n\rangle = \hbar\omega\left(\hat{a}^\dagger\hat{a} + \frac{1}{2}\right)|n\rangle = E_n|n\rangle. \tag{2.19}$$

Multiplying both sides by either $\hat{a}^\dagger$ or $\hat{a}$ yields two new eigenvalue equations for the eigenstates $(\hat{a}^\dagger|n\rangle)$ and $(\hat{a}|n\rangle)$

$$\begin{aligned}\hbar\omega\left(\hat{a}^\dagger\hat{a} + \frac{1}{2}\right)\hat{a}^\dagger|n\rangle &= (E_n + \hbar\omega)(\hat{a}^\dagger|n\rangle),\\ \hbar\omega\left(\hat{a}^\dagger\hat{a} + \frac{1}{2}\right)\hat{a}|n\rangle &= (E_n - \hbar\omega)(\hat{a}|n\rangle).\end{aligned} \tag{2.20}$$

We can see that the two operators acting on an energy eigenstate either increase or decrease its energy by one quantum of energy $\hbar\omega$ called a photon.

Applying the annihilation operator to the lowest-energy state cannot decrease its energy further and thus yields $\hat{a}|0\rangle = 0$. With this it becomes clear from Eq. 2.19 that the energy of the ground state $|0\rangle$ is $E_0 = \frac{1}{2}\hbar\omega$. Given that the creation operator generates one photon, and thus $E_{n+1} = E_n + \hbar\omega$, we see that the energy eigenvalues are

$$E_n = \hbar\omega\left(n + \frac{1}{2}\right), \tag{2.21}$$

and we can identify the action of the operator $\hat{a}^\dagger\hat{a}$ as the number operator $\hat{n} = \hat{a}^\dagger\hat{a}$

$$\hat{n}\,|n\rangle = n\,|n\rangle\,. \tag{2.22}$$

The states $|n\rangle$ are called number states. As described before, creation and annihilation operators act on the number states by creating or destroying one photon, i.e.

$$\hat{a}^\dagger\,|n\rangle = \sqrt{n+1}\,|n+1\rangle\,, \qquad \hat{a}\,|n\rangle = \sqrt{n}\,|n-1\rangle\,. \tag{2.23}$$

The coefficients on the right-hand side can be derived by calculating the inner product $\langle\psi|\psi\rangle$ for the two states $|\psi\rangle = \hat{a}\,|n\rangle$ and $|\psi\rangle = \hat{a}^\dagger\,|n\rangle$, additionally using the fact that the number states are normalized $\langle n|n\rangle$.

Any number state can be generated from the ground state by applying the creation operator n times

$$|n\rangle = \frac{(\hat{a}^\dagger)^n}{\sqrt{n!}}\,|0\rangle\,. \tag{2.24}$$

The number states are orthogonal

$$\langle n|m\rangle = \delta_{nm} \tag{2.25}$$

where δ_{nm} is the Kronecker-delta, and form a complete set

$$\sum_{n=0}^{\infty} |n\rangle\,\langle n| = 1. \tag{2.26}$$

2.2.2 Coherent states

The basis for many quantum optics experiments are laser beams. Laser beams don't have a defined number state and thus are described by coherent states $|\alpha\rangle$ instead of number states. Coherent states can be defined as eigenstates of the annihilation operator, i.e.

$$\hat{a}\,|\alpha\rangle = \alpha\,|\alpha\rangle\,. \tag{2.27}$$

In this eigenvalue equation the state can be expanded in the basis of number states by inserting Eq. 2.26

$$\begin{aligned}\hat{a}\,|\alpha\rangle &= \hat{a}\sum_{n=0}^{\infty} |n\rangle\,\underbrace{\langle n|\alpha\rangle}_{c_n} \\ &= \sum_{n=1}^{\infty} c_n\sqrt{n}\,|n-1\rangle = \alpha\sum_{n=0}^{\infty} c_n\,|n\rangle\,,\end{aligned} \tag{2.28}$$

where we see that the coefficients c_n in the last line must be equal, so

$$c_n\sqrt{n} = \alpha c_{n-1} \tag{2.29}$$

By repeatedly inserting c_n on the right side we eventually obtain

$$c_n = \frac{\alpha}{\sqrt{n}}c_{n-1} = \frac{\alpha^2}{\sqrt{n(n-1)}}c_{n-2} = \cdots = \frac{\alpha^n}{\sqrt{n!}}c_0, \tag{2.30}$$

so we see that the expansion of $|\alpha\rangle$ in the basis of number states reads

$$|\alpha\rangle = c_0 \sum_{n=0}^{\infty} \frac{\alpha^n}{\sqrt{n!}} |n\rangle . \tag{2.31}$$

We can obtain c_0 from the normalization requirement

$$\begin{aligned} 1 = \langle\alpha|\alpha\rangle &= |c_0|^2 \sum_{m=0}^{\infty}\sum_{n=0}^{\infty} \frac{\alpha^{\star m}\alpha^n}{\sqrt{m!n!}} \langle m|n\rangle \\ &= |c_0|^2 \sum_{n=0}^{\infty} \frac{|\alpha|^{2n}}{n!} = |c_0|^2 e^{|\alpha|^2} \\ \Leftrightarrow c_0 &= e^{-\frac{1}{2}|\alpha|^2}. \end{aligned} \tag{2.32}$$

With this Eq. 2.31 becomes

$$|\alpha\rangle = e^{-\frac{1}{2}|\alpha|^2} \sum_{n=0}^{\infty} \frac{\alpha^n}{\sqrt{n!}} |n\rangle . \tag{2.33}$$

We can obtain the mean photon number of this state by considering the expectation value of the number operator

$$\langle\alpha|\hat{n}|\alpha\rangle = \langle\alpha|\hat{a}^\dagger\hat{a}|\alpha\rangle = |\alpha|^2. \tag{2.34}$$

This gives us the energy difference of the state to the ground state, and we can in correspondence to the classical electric field interpret $|\alpha|$ as the classical amplitude of the light field.

The second way to define coherent states is by applying the displacement operator $\hat{D}(\alpha)$ to the vacuum, i.e.

$$|\alpha\rangle = \hat{D}(\alpha)|0\rangle , \tag{2.35}$$

with the displacement operator defined as

$$\hat{D}(\alpha) = \exp(\alpha\hat{a}^\dagger - \alpha^\star\hat{a}). \tag{2.36}$$

We can use the disentangling theorem to write it in another form. For two non-commuting operators $\hat{A}, \hat{B}$ with $[\hat{A}, \hat{B}] \neq 0$ that commute with their commutator ($[\hat{A}, [\hat{A}, \hat{B}]] = [\hat{B}, [\hat{A}, \hat{B}]] = 0$) it reads

$$e^{\hat{A}+\hat{B}} = e^{\hat{A}} e^{\hat{B}} e^{-\frac{1}{2}[\hat{A},\hat{B}]}. \tag{2.37}$$

With this we can write the displacement operator as

$$\hat{D}(\alpha) = e^{-\frac{1}{2}|\alpha|^2} e^{\alpha \hat{a}^\dagger} e^{-\alpha^\star \hat{a}}. \tag{2.38}$$

In this form we can apply it to the vacuum state and see that we obtain the same definition as Eq. 2.33

$$\begin{aligned}
\hat{D}(\alpha)|0\rangle = e^{-\frac{1}{2}|\alpha|^2} e^{\alpha \hat{a}^\dagger} e^{-\alpha^\star \hat{a}} |0\rangle &= e^{-\frac{1}{2}|\alpha|^2} e^{\alpha \hat{a}^\dagger} \underbrace{\sum_{n=0}^{\infty} \frac{(-\alpha^\star \hat{a})^n}{n!} |0\rangle}_{=|0\rangle} \\
&= e^{-\frac{1}{2}|\alpha|^2} \sum_{n=0}^{\infty} \frac{\alpha^n}{n!} (\hat{a}^{\dagger n} |0\rangle) \\
&= e^{-\frac{1}{2}|\alpha|^2} \sum_{n=0}^{\infty} \frac{\alpha^n}{\sqrt{n!}} |n\rangle = |\alpha\rangle .
\end{aligned} \tag{2.39}$$

This alternate definition is relevant when defining the squeezing operator, which takes a similar form as the displacement operator.

2.2.3 Quadrature operators

For continuous variable quantum optics the electric field operator from Eq. 2.16 is usually expressed in terms of dimensionless field amplitudes called quadratures. To arrive at their definition, we start by explicitly writing out the time dependence of the creation and annihilation operators, which in turn we can find by using Heisenberg's equation of motion [Coh19]. Applied to $\hat{a}$ it reads

$$\frac{\mathrm{d}\hat{a}}{\mathrm{d}t} = \frac{i}{\hbar}[\hat{H}, \hat{a}] = i\omega[\hat{n}, \hat{a}] = -i\omega\hat{a}. \tag{2.40}$$

This equation has the solution

$$\hat{a}(t) = \hat{a}(0) e^{-i\omega t}, \tag{2.41}$$

and analogously we can obtain the solution for $\hat{a}^\dagger$

$$\hat{a}^\dagger(t) = \hat{a}^\dagger(0) e^{i\omega t}. \tag{2.42}$$

Plugging this back into the electric field operator from Eq. 2.16 and assuming $\hat{a}(0) = \hat{a}$ and $\hat{a}^\dagger(0) = \hat{a}^\dagger$, we can write it as

$$\hat{E}_x = \mathcal{E}_0(\hat{a}e^{-i\omega t} + \hat{a}^\dagger e^{i\omega t})\sin(kz). \tag{2.43}$$

We can then introduce the quadrature operators

$$\hat{X} = (\hat{a} + \hat{a}^\dagger), \qquad \hat{Y} = \frac{1}{i}(\hat{a} - \hat{a}^\dagger) \tag{2.44}$$

and express the electric field operator in terms of these as

$$\hat{E}_x(t) = \mathcal{E}_0 \sin(kz)[\hat{X}\cos(\omega t) + \hat{Y}\sin(\omega t)]. \tag{2.45}$$

This equation clarifies the role of the quadrature operators $\hat{X}$ and $\hat{Y}$ as dimensionless field amplitudes that oscillate out of phase with each other. $\hat{X}$ and $\hat{Y}$ are called the amplitude and phase quadrature operator respectively.

Further it is useful to define a generic quadrature operator

$$\hat{X}(\phi) = \hat{a}e^{-i\phi} + a^\dagger e^{i\phi} \tag{2.46}$$

which we can interpret as a rotated quadrature operator. We see that $\hat{X}(0) = \hat{X}$ and $\hat{X}(\frac{\pi}{2}) = \hat{Y}$. Its usefulness will become clearer in the context of squeezed states and homodyne detection.

The amplitude and phase quadrature operators do not commute and follow the commutation relation

$$[\hat{X}, \hat{Y}] = 2i. \tag{2.47}$$

The Heisenberg uncertainty relation states that for a simultaneous measurement of two non-commuting observables, the measurement outcomes have a minimum uncertainty. In the case of the quadrature operators the uncertainty relation for an arbitrary state ψ is:

$$\mathrm{Var}(\hat{X})_\psi \,\mathrm{Var}(\hat{Y})_\psi \geq \frac{1}{4}|\langle[\hat{X}, \hat{Y}]\rangle_\psi|^2 = 1, \tag{2.48}$$

with the variances $\mathrm{Var}(\hat{X})_\psi = \langle\psi|\hat{X}^2|\psi\rangle - \langle\psi|\hat{X}|\psi\rangle^2$. The most relevant states for which to consider the uncertainty in the context of this thesis are the vacuum state $|0\rangle$, the coherent state $|\alpha\rangle$, and the squeezed state, which we will consider later in Ch. 2.3. For the vacuum state we can immediately see that the mean value of the

quadrature operators vanish,

$$\begin{aligned}\langle 0|\hat{X}|0\rangle &= \langle 0|\hat{a}+\hat{a}^\dagger|0\rangle = 0,\\ \langle 0|\hat{Y}|0\rangle &= \langle 0|\frac{1}{i}(\hat{a}-\hat{a}^\dagger)|0\rangle = 0,\end{aligned} \tag{2.49}$$

but for their squares we obtain

$$\begin{aligned}\langle 0|\hat{X}^2|0\rangle &= \langle 0|(\hat{a}+\hat{a}^\dagger)^2|0\rangle = 1\\ \langle 0|\hat{Y}^2|0\rangle &= 1\end{aligned} \tag{2.50}$$

so that their variances in the vacuum state are

$$\mathrm{Var}(X)_0 = \mathrm{Var}(Y)_0 = 1. \tag{2.51}$$

I want to note here that there are two conventions for defining the quadrature operator in quantum optics. In the other definition the uncertainty product equals $\frac{1}{16}$. I chose the definition for the uncertainty product to equal 1 as it simplifies shot noise normalization e.g. in squeezing measurements.

Performing the same computation for a general coherent state $|\alpha\rangle$ the mean value is

$$\begin{aligned}\langle\alpha|\hat{X}|\alpha\rangle &= 2\Re(\alpha),\\ \langle\alpha|\hat{Y}|\alpha\rangle &= 2\Im(\alpha).\end{aligned} \tag{2.52}$$

For the mean value of the squares we obtain

$$\begin{aligned}\langle\alpha|\hat{X}^2|\alpha\rangle &= \langle\alpha|\hat{a}^2+\hat{a}\hat{a}^\dagger+\hat{a}^\dagger\hat{a}+\hat{a}^{\dagger 2}|\alpha\rangle\\ &= \langle\alpha|\alpha^2+1+2|\alpha|^2+\alpha^{\star 2}|\alpha\rangle\\ &= 1+(2\Re(\alpha))^2, \qquad (2.53)\\ \langle\alpha|\hat{Y}^2|\alpha\rangle &= \langle\alpha|-\hat{a}^2+\hat{a}\hat{a}^\dagger+\hat{a}^\dagger\hat{a}-\hat{a}^{\dagger 2}|\alpha\rangle\\ &= \langle\alpha|-\alpha^2+1+2|\alpha|^2-\alpha^{\star 2}|\alpha\rangle\\ &= 1+(2\Im(\alpha))^2, \qquad (2.54)\end{aligned}$$

and so the variance is

$$\mathrm{Var}(X)_\alpha = \mathrm{Var}(Y)_\alpha = 1. \tag{2.55}$$

Thus, we can see that both the vacuum state and the coherent state minimize the uncertainty product from Eq. 2.48. As the coherent state is a good approximation of a classical state, we see that it allows for precise measurements in a pure classical setting.

2.3 Squeezed state

The Heisenberg uncertainty relation gives a lower limit for the variance product of two non-commuting observables. We have seen in the previous section that for the vacuum state and for coherent states the product is minimized with equal variances of each quadrature $\mathrm{Var}(X)_{0,\alpha} = \mathrm{Var}(Y)_{0,\alpha} = 1$. Quantum states which exhibit a smaller variance in one quadrature than the other are called squeezed states $|\xi\rangle$. For the uncertainty relation to still hold, we can define the variances of a squeezed minimum uncertainty state as

$$\mathrm{Var}(\hat{X})_\xi = e^{-2r}, \qquad \mathrm{Var}(\hat{Y})_\xi = e^{2r} \tag{2.56}$$

for some real valued r called the squeeze parameter, so that their product equals 1. From a theoretical perspective such a state can be constructed by introducing the squeezing operator

$$\hat{S}(\xi) = \exp\left[\frac{1}{2}(\xi^\star \hat{a}^2 - \xi \hat{a}^{\dagger 2})\right] \tag{2.57}$$

with $\xi = re^{i\theta}$, where θ is the squeezing angle. To generate a squeezed state we apply the squeezing operator to an arbitrary state, $|\xi\rangle = \hat{S}(\xi)|\psi\rangle$. In the special case that the state is the vacuum state, we call the resulting state a squeezed vacuum state $|\xi_{\mathrm{vac}}\rangle = \hat{S}(\xi)|0\rangle$.

We can immediately see that the squeezing operator is unitary by observing that $\hat{S}^\dagger(\xi) = \hat{S}(-\xi)$ and that the commutator of the exponents is zero. We can apply the Baker-Campbell-Hausdorff formula, i.e. $e^{\hat{X}}e^{\hat{Y}} = e^{\hat{X}+\hat{Y}}$ for $[\hat{X}, \hat{Y}] = 0$, and immediately see that

$$\hat{S}^\dagger(\xi)\hat{S}(\xi) = e^{\frac{1}{2}(-\xi^\star \hat{a}^2 + \xi \hat{a}^{\dagger 2})} e^{\frac{1}{2}(\xi^\star \hat{a}^2 - \xi \hat{a}^{\dagger 2})} = e^{\frac{1}{2}(-\xi^\star \hat{a}^2 + \xi \hat{a}^{\dagger 2} + \xi^\star \hat{a}^2 - \xi \hat{a}^{\dagger 2})} = 1. \tag{2.58}$$

To calculate the quadrature variances it is useful to first calculate how the squeezing operator transforms the creation operator, i.e. $\hat{S}^\dagger(\xi)\hat{a}\hat{S}(\xi)$ and $\hat{S}^\dagger(\xi)\hat{a}^2\hat{S}(\xi)$, and similar for the annihilation operator. These can be found by applying the Campbell identity, which for two arbitrary operators reads

$$e^{\hat{X}}\hat{Y}e^{-\hat{X}} = \sum_{n=0}^{\infty} \frac{[(\hat{X})^n, \hat{Y}]}{n!} \tag{2.59}$$

with the iterated commutator $[(\hat{X})^n, \hat{Y}] = [\hat{X}, \ldots [\hat{X}, [\hat{X}, \hat{Y}]] \ldots]$.

Let us first consider the iterative commutator from the Campbell identity for $\hat{X} = \hat{S}(-\xi)$ and $\hat{Y} = \hat{a}$. (The computation requires knowledge of the commutators

$[\hat{a}^2, \hat{a}^\dagger] = 2\hat{a}$ and $[\hat{a}^{\dagger 2}, \hat{a}] = -2\hat{a}^\dagger$.) It reads

$$\begin{aligned}\left[\frac{1}{2}(-\xi^\star \hat{a}^2 + \xi \hat{a}^{\dagger 2})^n, \hat{a}\right] &= [\ldots, \underbrace{[\frac{1}{2}(-\xi^\star \hat{a}^2 + \xi \hat{a}^{\dagger 2}), \hat{a}]}_{=\frac{1}{2}\xi[\hat{a}^{\dagger 2}, \hat{a}] = -\xi \hat{a}^\dagger} \ldots] \\ &= [\ldots, \underbrace{[\frac{1}{2}(-\xi^\star \hat{a}^2 + \xi \hat{a}^{\dagger 2}), -\xi \hat{a}^\dagger]}_{=\frac{1}{2}|\xi|^2[\hat{a}^2, \hat{a}^\dagger] = |\xi|^2 \hat{a}} \ldots] \\ &= \begin{cases} |\xi|^n \hat{a} & \text{for even } n \\ -\xi |\xi|^{n-1} \hat{a}^\dagger & \text{for odd } n. \end{cases} \end{aligned} \tag{2.60}$$

With this we can write

$$\begin{aligned}\hat{S}^\dagger(\xi) \hat{a} \hat{S}(\xi) &= \sum_{n=0}^{\infty} \frac{|\xi|^{2n}}{(2n)!} \hat{a} - \sum_{n=0}^{\infty} \frac{\xi |\xi|^{2n}}{(2n+1)!} \hat{a}^\dagger \\ &= \hat{a} \cosh r - \hat{a}^\dagger e^{i\theta} \sinh r, \end{aligned} \tag{2.61}$$

$$\hat{S}^\dagger(\xi) \hat{a}^\dagger \hat{S}(\xi) = \hat{a}^\dagger \cosh r - \hat{a} e^{-i\theta} \sinh r. \tag{2.62}$$

Now we can calculate the quadrature variances of the squeezed vacuum state by making use of the squeezing operators unitarity

$$\begin{aligned}\mathrm{Var}(\hat{X})_{\xi_{\mathrm{vac}}} &= \langle \xi_{\mathrm{vac}} | \hat{X}^2 | \xi_{\mathrm{vac}} \rangle - \langle \xi_{\mathrm{vac}} | \hat{X} | \xi_{\mathrm{vac}} \rangle^2 \\ &= \langle 0 | \hat{S}^\dagger(\xi) \hat{X} \hat{S}(\xi) \hat{S}^\dagger(\xi) \hat{X} \hat{S}(\xi) | 0 \rangle - \underbrace{\langle 0 | \hat{S}^\dagger(\xi) \hat{X} \hat{S}(\xi) | 0 \rangle^2}_{=0, \text{ only terms } O(\hat{a}, \hat{a}^\dagger)} \\ &= \cosh^2 r + \sinh^2 r - 2 \sinh r \cosh r \cos\theta, \end{aligned} \tag{2.63}$$

$$\mathrm{Var}(\hat{Y})_{\xi_{\mathrm{vac}}} = \cosh^2 r + \sinh^2 r + 2 \sinh r \cosh r \cos\theta. \tag{2.64}$$

For a squeezing angle $\theta = 0$ we obtain the result from Eq. 2.56

$$\mathrm{Var}(\hat{X}) = e^{-2r}, \qquad \mathrm{Var}(\hat{Y}) = e^{2r}. \tag{2.65}$$

For other squeezing angles $\theta \neq 0$ squeezing might not be observable in the $\hat{X}$ or $\hat{Y}$ quadrature. Instead, it is visible in the variance of the rotated quadrature operator $\hat{X}(\phi)$ from Eq. 2.46

$$\mathrm{Var}(\hat{X}(\phi))_{\xi_{\mathrm{vac}}} = \cosh^2 r + \sinh^2 r - 2 \sinh r \cosh r \cos(\theta - 2\phi), \tag{2.66}$$

which has extreme values of e^{-2r} at $\phi = \theta/2$ and e^{2r} at $\phi = \theta/2 - \pi/2$.

Note that for a squeezed state, combining Eq. 2.65 and the uncertainty relation from Eq. 2.48 yields an ellipse in the $\hat{X}, \hat{Y}$ phase space with its axes aligned with the

rotated quadratures $\hat{X}(\theta/2), \hat{X}(\theta/2+\pi/2)$.

Distinguishing between a rotated squeezing operator and a rotated quadrature operator might seem arbitrary for a squeezed vacuum state. It becomes more meaningful when considering that a squeezed state may also be displaced. A displaced squeezed vacuum state $|\alpha, \xi_{\text{vac}}\rangle$ can be generated by applying the squeezing operator and the displacement operator consecutively

$$|\alpha, \xi_{\text{vac}}\rangle = \hat{D}(\alpha)\hat{S}(\xi)\,|0\rangle\,. \tag{2.67}$$

The resulting state has the same displacement as a coherent state with amplitude α with squeezed quadrature variances. Here the squeezing angle describes the rotation between the axes of the squeezing ellipse and the coherent state's phase.

It is helpful to visualize these states as a phasor in the $(\hat{X}, \hat{Y})$ phase space. In this picture we can obtain the electric field at a given time t by rotating the reference frame by $\frac{\omega}{2\pi}t$ and projecting the phasor onto the $\hat{X}$-axis. For the amplitude quadrature squeezed ($\theta = 0$) displaced vacuum state shown in 2.3c this results in reduced uncertainty around the extreme values of the cosine. The phase space pictures and electric field of a coherent state, a squeezed vacuum state, and a displaced squeezed vacuum state are visualized in Fig. 2.3.

Experimentally a squeezed state is often characterized by the amount of noise reduction compared to the shot noise measured in decibel. It is calculated as the ratio of noise power levels of squeezed state and shot noise. We can obtain the decibel value by using $\text{dB} = 10\log_{10}(\text{Var}(\hat{X})_\xi / \text{Var}(\hat{X})_0)$. A squeeze factor of 0.46 is equivalent to a noise reduction of 4 dB.

The characteristics of a squeezed state for each sideband frequency can be obtained from the quantum mechanical description of a single-sided cavity. A detailed description can be found in [Wal08; Bau16], which in the end yields the output spectra

$$\begin{aligned}
\text{Var}(\hat{X}(\nu))_{\xi_{\text{vac}}} &= 1 - \frac{4P/P_{\text{thr}}}{1 + (P/P_{\text{thr}})^2 + 4(\nu/\delta\nu)^2}, \\
\text{Var}(\hat{Y}(\nu))_{\xi_{\text{vac}}} &= 1 + \frac{4P/P_{\text{thr}}}{1 - (P/P_{\text{thr}})^2 + 4(\nu/\delta\nu)^2},
\end{aligned} \tag{2.68}$$

where $\delta\nu$ is the cavity linewidth. They are shown graphically in Fig. 2.4. The maximum amount of squeezing is produced at zero sideband frequency and is determined by how close the input pump power P at the harmonic wavelength is to the lasing threshold P_{thr} of the cavity. The lasing threshold is reached at the point where the gain per cavity round trip in the fundamental mode due to conversion is equal to the loss per round trip from absorption and transmission through the coupling mirror, i.e. at a gain factor of 1 as defined in Eq. 2.1.

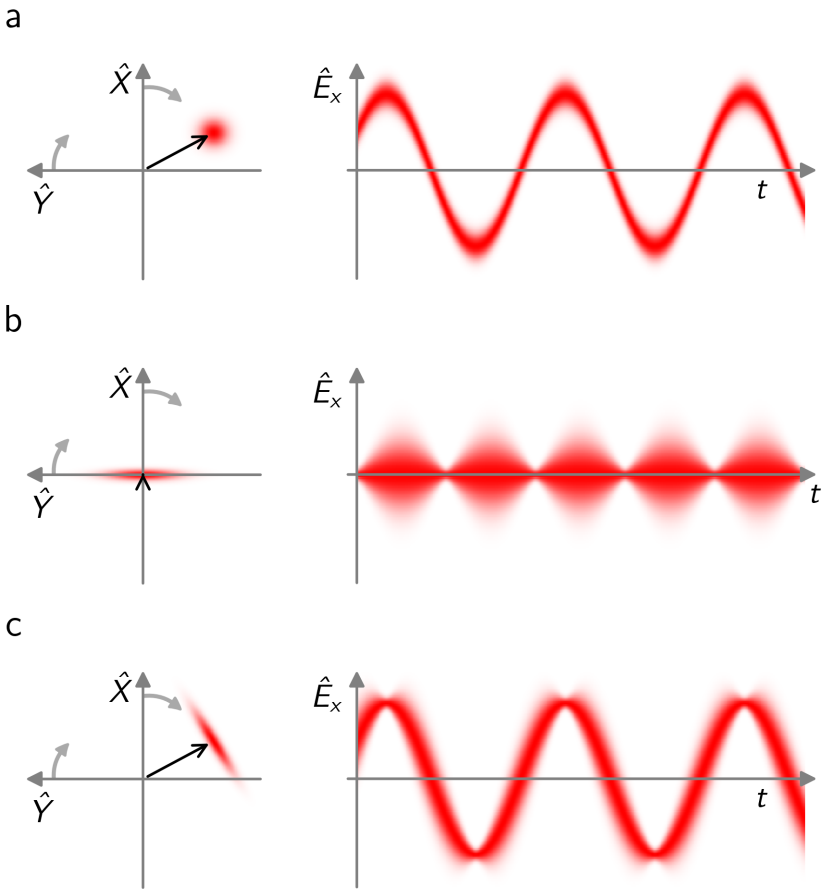

Figure 2.3: Phase space pictures and electric field over time displaying the uncertainty of three minimum uncertainty states. (a) A coherent state $|\alpha\rangle$ with $|\alpha| = 6$, $\theta_\alpha = 60°$, and $\mathrm{Var}(X)_\alpha = 1$. (b) A squeezed vacuum state $|\xi_{\mathrm{vac}}\rangle$ with $r = 0.46$ equivalent to 4 dB noise reduction, $\theta = 0°$. (c) An amplitude squeezed displaced vacuum state $|\alpha, \xi_{\mathrm{vac}}\rangle$ with $|\alpha| = 6, \theta_\alpha = 60°, r = 0.46, \theta = 0°$. The axes rotate with frequency $\frac{\omega}{2\pi}$.

2.3.1 Balanced homodyne detection

A common way to detect a squeezed state is using balanced homodyne detection, see Fig. 2.5. It is based on mixing the signal field, in this case a squeezed state, with a strong coherent field at the same wavelength called the local oscillator (LO) on a balanced beam splitter, i.e. a mirror with power reflectivity $R = 0.5$. Let us call the input modes of the beam splitter $|\alpha\rangle$ and $|\beta\rangle$, and the output modes $|\gamma\rangle$ and $|\delta\rangle$. The output modes are fully detected by two photo diodes. They each produce a photo current proportional to the intensity of that output $I_c \sim \langle \hat{n}_\gamma \rangle = \langle \hat{c}^\dagger \hat{c} \rangle$ and $I_d \sim \langle \hat{n}_\delta \rangle = \langle \hat{d}^\dagger \hat{d} \rangle$. $\hat{c}^\dagger, \hat{c}, \hat{d}^\dagger, \hat{d}$ are the creation and annihilation operators of the respective modes, the operators for different modes commute, i.e. $[\hat{c}, \hat{d}] = [\hat{c}, \hat{d}^\dagger] = 0$.

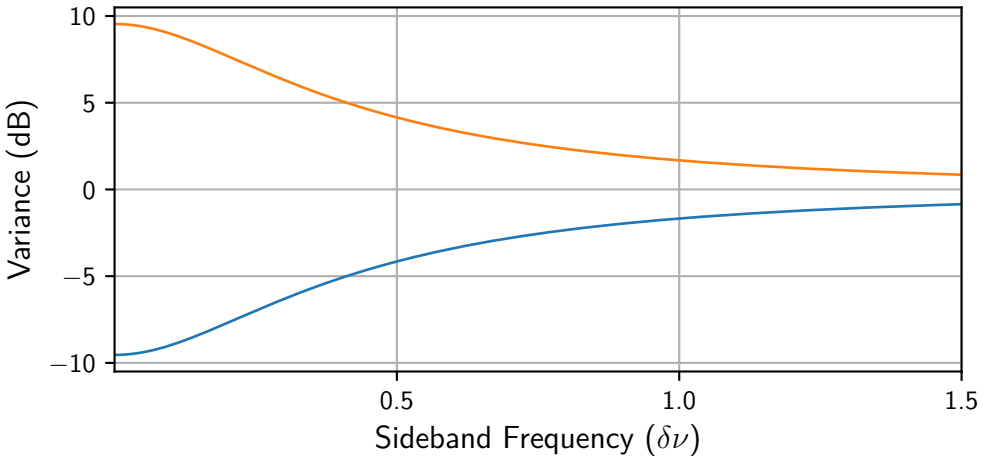

Figure 2.4: Sideband frequency dependence of a lossless squeezed state from a cavity in units of its linewidth $\delta\nu$ pumped at 50 % of its threshold power $P/P_{\text{thr}} = 0.5$.

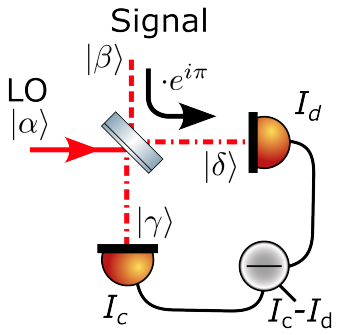

Figure 2.5: Schematic setup of balanced homodyne detection.

We can write the output mode operators in terms of the input modes as

$$\begin{pmatrix} \hat{c} \\ \hat{d} \end{pmatrix} = \frac{1}{\sqrt{2}} \begin{pmatrix} 1 & 1 \\ 1 & -1 \end{pmatrix} \begin{pmatrix} \hat{a} \\ \hat{b} \end{pmatrix}, \tag{2.69}$$

where I chose a specific matrix representation for the beam splitter with a phase shift of $e^{i\pi}$ for one reflected beam. Let us look at the difference of the two photo currents:

$$\begin{aligned} I_c - I_d \sim \langle \hat{n}_\gamma - \hat{n}_\delta \rangle &= \langle \hat{c}^\dagger \hat{c} - \hat{d}^\dagger \hat{d} \rangle \\ &= \langle \hat{a}^\dagger \hat{b} + \hat{b}^\dagger \hat{a} \rangle . \end{aligned} \tag{2.70}$$

If we make the assumption that the LO input $|\alpha\rangle$ is a coherent state $|\alpha_{\text{LO}} e^{-i\omega t}\rangle$ and express α_{LO} in polar form $\alpha_{\text{LO}} = |\alpha_{\text{LO}}| e^{i\phi}$ we get

$$\langle \hat{n}_\gamma - \hat{n}_\delta \rangle = |\alpha_{\text{LO}}| \langle \hat{b} e^{i\omega t} e^{-i\phi} + \hat{b}^\dagger e^{-i\omega t} e^{i\phi} \rangle . \tag{2.71}$$

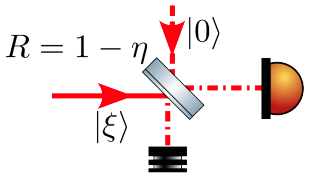

Figure 2.6: Model of optical loss as a vacuum state coupling in on a beam splitter.

Considering only a signal field at the same optical frequency ω we can write $\hat{b} = \hat{b_0} e^{-i\omega t}$ and the currents as

$$\langle \hat{n}_\gamma - \hat{n}_\delta \rangle = |\alpha_{\mathrm{LO}}| \, \langle \hat{X}_\beta(\phi) \rangle \tag{2.72}$$

with the rotated quadrature operator from Eq. 2.46. We can see that the photo current difference is proportional to the quadrature of the signal field amplified by the amplitude of the LO. Adjusting the phase ϕ between LO and signal field allows changing the measured quadrature.

2.3.2 Effect of loss

Experimentally any optical beam is always subject to some amount of loss, be it through imperfect reflectivities of mirrors, scattering, absorption, mode mismatch, or detection efficiency of the photodetectors. Squeezed states are sensitive to optical loss. The effect of loss on a squeezed state (or any other optical state) can be modeled as a vacuum state overlapped with the squeezed state on a beam splitter with power reflectivity $1-\eta$ as shown in Fig. 2.6, where η is the total detection efficiency. In this model the detected variances of an amplitude quadrature squeezed state read

$$\begin{aligned} \mathrm{Var}(\hat{X})_{\xi_{\mathrm{vac}},\eta} &= \eta \underbrace{\mathrm{Var}(\hat{X})_{\xi_{\mathrm{vac}}}}_{e^{-2r}} + (1-\eta) \underbrace{\mathrm{Var}(\hat{X})_0}_{=1} \\ &= (1-\eta) + \eta e^{-2r} \qquad (2.73) \\ \mathrm{Var}(\hat{Y})_{\xi_{\mathrm{vac}},\eta} &= (1-\eta) + \eta e^{2r}. \qquad (2.74) \end{aligned}$$

Loss affects the squeezed and anti-squeezed variance asymmetrically, which is shown in Fig. 2.7 for three squeezed states with $-5\,\mathrm{dB}$, $-10\,\mathrm{dB}$, and $-15\,\mathrm{dB}$ of initial squeezing, equivalent to a squeeze factor $r = 0.58, 1.15$, and 1.7. On a logarithmic scale the squeezed variance is affected much more by loss than the anti-squeezed variance. For a given measured pair of squeezed and anti-squeezed variances we can calculate the detection efficiency by assuming the same squeeze factor r for both Eqs.

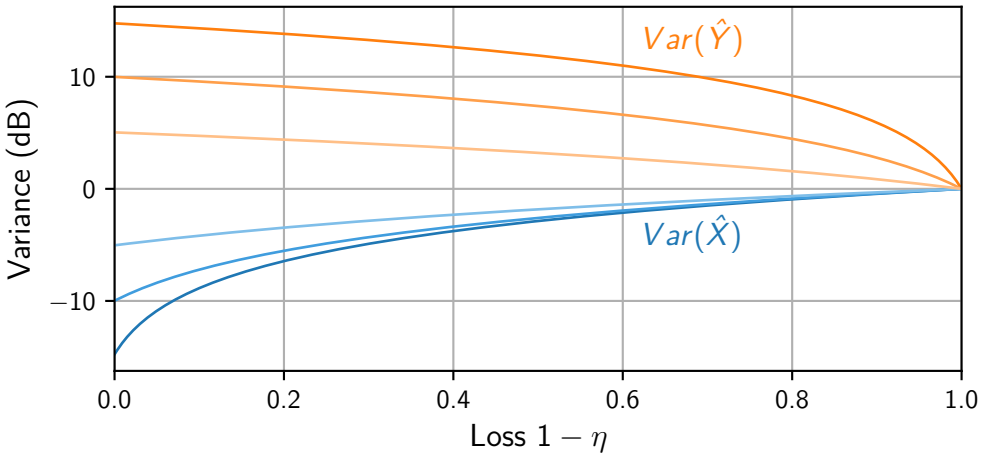

Figure 2.7: Variances of a squeezed state for three different squeeze factors ($r = 0.58, 1.15$, and 1.7) vs detection loss.

2.73 and 2.74 and solving for η, which yields

$$\eta = \frac{\left(\mathrm{Var}(X)_{\xi_{\mathrm{vac}},\eta} - 1\right)\left(\mathrm{Var}(Y)_{\xi_{\mathrm{vac}},\eta} - 1\right)}{2 - \mathrm{Var}(X)_{\xi_{\mathrm{vac}},\eta} - \mathrm{Var}(Y)_{\xi_{\mathrm{vac}},\eta}}. \tag{2.75}$$

It is of note that the minimum squeezed variance that can be reached is limited by the detection efficiency, e.g. for $\eta = 0.5$ the minimum squeezed variance regardless of squeeze factor is $-3\,\mathrm{dB}$.

The effect of loss modifies the expressions for the spectra from Eq. 2.68 by adding a factor of η in front of the (anti-) squeezing term:

$$\mathrm{Var}(\hat{X}(\nu))_{\xi_{\mathrm{vac}}} = 1 - \eta \frac{4P/P_{\mathrm{thr}}}{1 + (P/P_{\mathrm{thr}})^2 + 4(\nu/\delta\nu)^2}, \tag{2.76}$$

$$\mathrm{Var}(\hat{Y}(\nu))_{\xi_{\mathrm{vac}}} = 1 + \eta \frac{4P/P_{\mathrm{thr}}}{1 - (P/P_{\mathrm{thr}})^2 + 4(\nu/\delta\nu)^2}. \tag{2.77}$$

2.3.3 Phase noise in squeezing detection

The presence of phase noise in the detection process is detrimental to the amount of squeezing that is visible. Its effect is similar to that of detection loss, affecting the squeezing level more significantly than the anti-squeezing level. Optical fibers in particular introduce phase noise, which makes it relevant to discuss here.

We can imagine phase noise as the squeezing ellipse jittering in the $\hat{X}\hat{Y}$-phase space, causing a small misalignment between the readout quadrature $\hat{X}(\phi)$ and the squeezing angle θ. The detector averages the quadrature over the non-zero time that a measurement takes. Jittering of the ellipse causes the orthogonal quadrature to

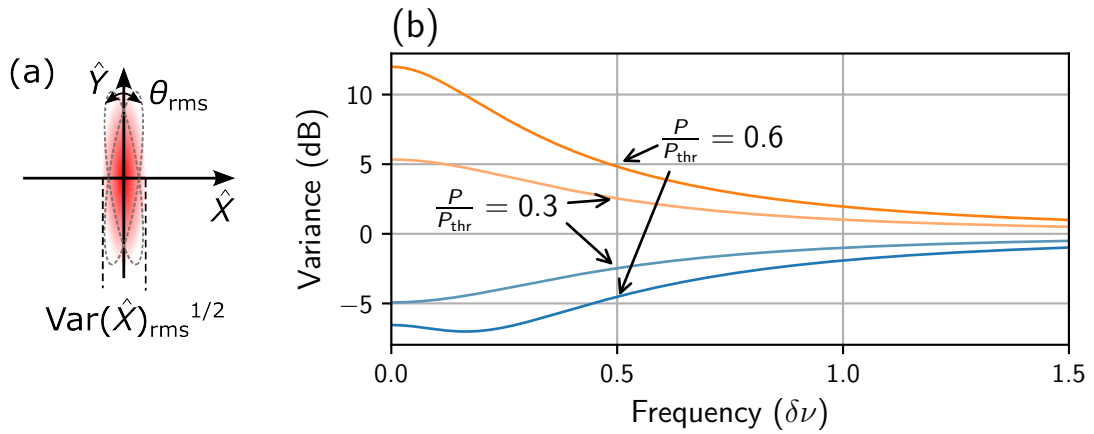

Figure 2.8: (a) Phase noise in the phase space picture, where it leads to a larger squeezed variance compared to the no-noise case. (b) Effect of phase noise on the squeezing spectrum. Lower frequencies experience higher apparent loss due to a higher amount of anti-squeezing contaminating the squeezed quadrature. The effect is more noticeable for higher squeezing values, i.e for the curves with $\frac{P}{P_{\text{thr}}} = 0.6$. I assumed a phase noise amplitude of $\theta_{\text{rms}} = 0.1\,\text{rad}$ for both curves.

contaminate the measurement quadrature. Modeling the phase noise as Gaussian with a root-mean-square amplitude θ_{rms}, the measured quadrature variance can be obtained as in Ref. [Oel16] as

$$\text{Var}(\hat{X})_{\theta_{\text{rms}}} = \text{Var}(\hat{X})\cos^2\theta_{\text{rms}} + \text{Var}(\hat{Y})\sin^2\theta_{\text{rms}}. \tag{2.78}$$

Squeezed and anti-squeezed variance are affected by this asymmetrically. As the squeezed variance is small, adding part of the larger anti-squeezed variance has a larger effect than the inverse. This makes the effect of phase noise especially relevant for a high anti-squeezed variance. Interestingly when considering the squeezing spectrum produced by a cavity from Eq. 2.68, phase noise can appear to introduce frequency dependent loss, as shown in Fig. 2.8.

2.3.4 Two-mode squeezed state

Similar to the squeezing operator we can define a two-mode squeezing operator

$$\hat{S}_{ab}(\xi) = \exp\left[(\xi^\star \hat{a}\hat{b} - \xi\hat{a}^\dagger\hat{b}^\dagger)\right] \tag{2.79}$$

acting on two separate modes $|a\rangle$, $|b\rangle$. Its action on a vacuum state in both modes produces a two-mode squeezed vacuum state

$$|\xi\rangle_{ab,\text{vac}} = \hat{S}_{ab}(\xi)\,|00\rangle_{ab} \tag{2.80}$$

with the squeeze factor $\xi = re^{i\theta}$ in polar form. The state does not factor into two single modes and thus creates entanglement between the two modes.

As we will see later, correlations can be observed in the superposition quadrature operators that can be constructed as the superposition of single-mode quadrature operators. The rotated superposition quadrature operator reads

$$\hat{X}_{ab}(\phi,\psi) = \frac{1}{\sqrt{2}}(\hat{X}_a(\phi) + \hat{X}_b(\psi)) \tag{2.81}$$

with readout quadrature angles ϕ and ψ. It is useful to introduce the shorthand

$$\hat{X}^{\pm}_{ab}(\phi) = \hat{X}_{ab}(\phi, \pm\phi) \tag{2.82}$$

where we get the sum of the non-rotated single-mode quadrature operators as $\hat{X}^{+}_{ab} = \hat{X}^{+}_{ab}(0°)$ and $\hat{Y}^{+}_{ab} = \hat{X}^{+}_{ab}(90°)$. These fulfill the same commutation relation as the single-mode operators, i.e. $[\hat{X}_{ab}, \hat{Y}_{ab}] = 2i$, from which the analogous uncertainty relation

$$\mathrm{Var}(\hat{X}_{ab})_\psi \,\mathrm{Var}(\hat{Y}_{ab})_\psi \geq 1 \tag{2.83}$$

follows, and we can quickly see that the two-mode vacuum $|00\rangle_{ab}$ minimizes the inequality with equal variances of 1 for both quadratures.

Analogous to the single-mode squeezing case, to calculate the variances of a two-mode squeezed state for different operators we first need to calculate how the operators $\hat{a}, \hat{b}$ transform with $\hat{S}_{ab}(\xi)$, i.e.

$$\begin{aligned} \hat{S}^{\dagger}_{ab}(\xi)\hat{a}\hat{S}_{ab}(\xi) &= \hat{a}\cosh r - e^{i\theta}\hat{b}^{\dagger}\sinh r, \\ \hat{S}^{\dagger}_{ab}(\xi)\hat{b}\hat{S}_{ab}(\xi) &= \hat{b}\cosh r - e^{i\theta}\hat{a}^{\dagger}\sinh r. \end{aligned} \tag{2.84}$$

If we consider the variance of a single-mode quadrature operator, e.g. of mode $|a\rangle$, we see that

$$\mathrm{Var}(\hat{X}_a(\phi))_{\xi_{ab,\mathrm{vac}}} = \cosh 2r \geq 1 = \mathrm{Var}(\hat{X}_a(\phi))_0. \tag{2.85}$$

We observe a variance greater than the variance of the vacuum state independent of both the phases of the two-mode squeezed state θ and of the readout quadrature ϕ. However, for the multimode quadrature operator we obtain

$$\mathrm{Var}(\hat{X}_{ab}(\phi,\psi))_{\xi_{ab,\mathrm{vac}}} = \cosh^2 r + \sinh^2 r - 2\sinh r\cosh r\cos(\theta - (\phi+\psi)) \tag{2.86}$$

which in the case of the sum quadrature operators gives

$$\begin{aligned} \mathrm{Var}(\hat{X}^+_{ab})_{\xi_{ab,\mathrm{vac}}} &= \cosh^2 r + \sinh^2 r - 2\sinh r \cosh r \cos\theta, \\ \mathrm{Var}(\hat{Y}^+_{ab})_{\xi_{ab,\mathrm{vac}}} &= \cosh^2 r + \sinh^2 r + 2\sinh r \cosh r \cos\theta, \end{aligned} \tag{2.87}$$

or

$$\mathrm{Var}(\hat{X}^+_{ab})_{\xi_{ab,\mathrm{vac}}} = e^{-2r}, \qquad \mathrm{Var}(\hat{Y}^+_{ab})_{\xi_{ab,\mathrm{vac}}} = e^{2r} \qquad \text{for } \theta = 0, \tag{2.88}$$

a similar result to the single-mode squeezing and quadrature operators. However, the difference here is that we observe a squeezed variance only in the superposition of the two modes a and b.

If we consider Eq. 2.86 and keep $\theta = 0$ fixed, we can see that in fact the variance is squeezed when $\phi = -\psi$ i.e. for the shorthand $\hat{X}^-_{ab}(\phi)$ we obtain $\mathrm{Var}(X^-_{ab})_{\xi_{ab,\mathrm{vac}}} = e^{-2r}$ for any readout angle ϕ.

There are different interpretations of modes the two-mode squeezing operator can act upon. Two examples: The operator arises in the description of a single parametric down-conversion (PDC) cavity between the upper and lower frequency sidebands around the fundamental frequency where it entangles the two frequency modes. It provides a description of the cavity's sideband spectrum within its linewidth in the (nearly) frequency degenerate case, as well as for the case of two distinct output frequencies, e.g. 810 nm and 1550 nm from [Sam12]. It also appears in the description of the spatial output modes of a balanced beam splitter with two squeezed inputs [Kim02]. Both are of particular interest for QKD as the two modes can be separated spatially by an arbitrary distance to perform a locality test.

2.4 Entanglement and non-locality criteria

In the early days of quantum mechanics when studying entanglement Einstein-Podolsky-Rosen (EPR) proposed a famous thought experiment [Ein35] that brought up the contradiction between local causality and the completeness of quantum mechanics. The experiment considers two entangled particles separated by an arbitrary distance. Two parties, Alice and Bob, perform a measurement on these particles and find that the outcomes they obtained are correlated. The EPR paradox concerns itself with the following: On the one hand quantum mechanics postulates that the measurement outcome is probabilistic and determined at the time of the measurement. On the other hand, for Alice's and Bob's measurements to be correlated, Alice's measurement must have instantly affected Bob's particle an arbitrary distance away, violating relativity. EPR originally concluded that quantum theory was incomplete, that "a more complete specification of the state" [Bel64] exists, i.e. that there are local hidden variables that decide the outcome of the measurement. Later Bell proposed a way to disprove this

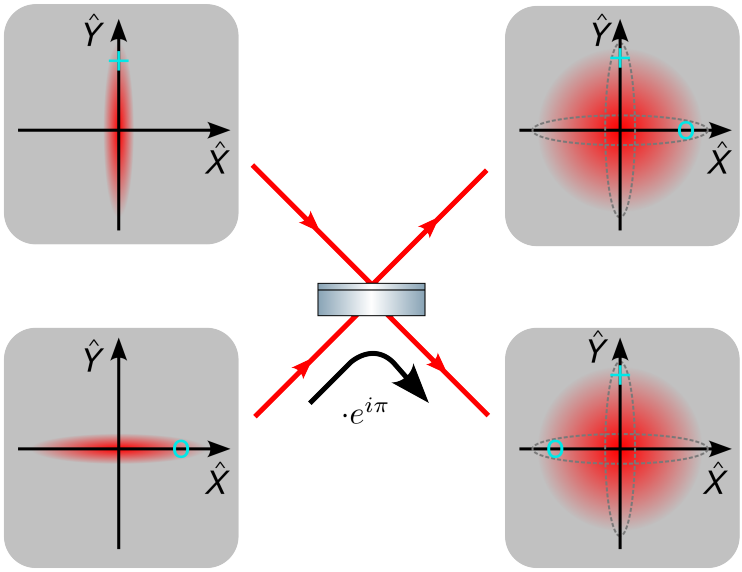

Figure 2.9: Phase space representation of two squeezed states overlapped at a beam splitter producing a two-mode squeezed state in the two output ports. Cross and circle indicate the axis across which the quadrature values are (anti-) correlated.

local hidden variable theory by performing a specific set of measurements called a Bell test, and thus ascribed a non-local nature to reality.

A weaker non-locality criterion was proposed by Reid [Rei89; Cav09], formulated for continuous non-commuting observables such as the quadratures $\hat{X}$ and $\hat{Y}$. They started by defining the inferred variance

$$\mathrm{Var}_{\mathrm{inf}}(X_B)_\psi = \langle (X_B - X_B^{\mathrm{est}}(X_A))^2 \rangle_\psi \tag{2.89}$$

as a measure of how well Alice can give an estimate X_B^{est} of Bob's measurement outcome X_B of the observable $\hat{X}_B$ given her own outcome X_A of $\hat{X}_A$. Depending on the quadrature the best estimate Alice can make is her own measurement outcome $X_B^{\mathrm{est}} = X_A$ or the negative in the other quadrature $Y_B^{\mathrm{est}} = -Y_A$. Non-locality is demonstrated if the inequality

$$\sqrt{\mathrm{Var}_{\mathrm{inf}}(X_B)_\psi \, \mathrm{Var}_{\mathrm{inf}}(Y_B)_\psi} < 1 \tag{2.90}$$

is fulfilled, the so called EPR-Reid criterion.

This criterion is weaker than that provided by a Bell test. This follows from the different conditions required for each of the criteria, which is summarized in [Cav09]: Whereas EPR's condition for reality considers "predict[ing] with certainty [...] the value of a physical quantity", Reid's extension loosens it to "predict [the quantity] with some specified uncertainty".

A violation of the EPR-Reid criterion is equivalent [Wis07; Cav09] to a phenomenon called steering. From Bob's perspective Alice can predict his measurement outcome better than the uncertainty of the vacuum state.

An even weaker criterion has been proposed by Duan [Dua00] which concerns the separability of the wave function, i.e. if it is possible to fully express it as the product of two individual subsystems. If there exists any degree of entanglement between the two subsystems, they are inseparable. The criterion formulated by Duan (and applied to quadratures) states that inseparability is shown when

$$\mathrm{Var}(X_A + X_B)_\psi + \mathrm{Var}(Y_A - Y_B)_\psi < 4 \tag{2.91}$$

or expressed with the inferred variances from above

$$\mathrm{Var}_{\mathrm{inf}}(X_B)_\psi + \mathrm{Var}_{\mathrm{inf}}(Y_B)_\psi < 4. \tag{2.92}$$

Let us compare what these criteria yield the vacuum state. The two vacuum modes of Alice and Bob are uncorrelated, so the inferred variance evaluates to

$$\mathrm{Var}(X_A + X_B)_0 = \underbrace{\mathrm{Var}(X_A)_0}_{=1} + \underbrace{\mathrm{Var}(X_B)_0}_{=1} = 2 = \mathrm{Var}(Y_A - Y_B) \tag{2.93}$$

and their sum equals 4. A state exhibiting stronger correlations than the vacuum must be inseparable. For a two-mode squeezed state we can use Eq. 2.86 to obtain

$$\mathrm{Var}(X_A + X_B)_{\xi_{\mathrm{vac}}} = 2\mathrm{Var}(\hat{X}^-_{ab}) = 2e^{-2r} = \mathrm{Var}(Y_A - Y_B) \tag{2.94}$$

for which their sum is smaller than 4 for any $r > 0$. However, beating the EPR-Reid criterion requires that their product

$$\sqrt{\mathrm{Var}(X_A + X_B)\mathrm{Var}(Y_A - Y_B)} = 2e^{-2r} < 1 \tag{2.95}$$

which requires a measured squeeze factor greater than 0.347 equal to a $-3\,\mathrm{dB}$ squeezed variance.

2.4.1 Application for quantum key distribution

The goal of QKD is to enable secret communication between two parties, Alice and Bob, without allowing an eavesdropper, Eve, to gain information. Showing that a non-locality criterion is beaten is useful for this, as well other quantum information tasks. Here it can be used to obtain a limit of how much of the quantum state was leaked to Eve during transmission and calculate a bound on the information Eve has access to. In particular, if the distributed quantum state can be used to beat the EPR-Reid criterion, this indicates that at most 50 % of the quantum state could have

been leaked, so that the majority of the quantum state is shared with Bob.

Building on this, a protocol can be formulated [Wal16; Fur12] that exploits this advantage to reduce Eve's information to an arbitrarily small proportion. Beating the criterion additionally lessens the security assumptions required of Bob's measurement station. It directly follows from beating the criterion, that the measurement was performed correctly and that the detector was not defective or tampered with by Eve beforehand. If the detector is compromised, the protocol aborts. This ensures security as long as no information is broadcast outside of Bob's measurement station.

The QKD protocol presented in [Wal16] considers Alice and Bob to each be located in a measurement station that is private, i.e. that does not leak any information to the outside. The stations are connected by a quantum channel and an authenticated classical channel. Alice's station contains a source that produces a state exhibiting EPR-like correlations, e.g. a two-mode squeezing source that produces states that beat the EPR-Reid criterion. Both stations also contain a detector and a way to generate random numbers, e.g. a quantum random number generator (QRNG). The protocol is then performed as follows:

State distribution and measurement: Alice sends one part of the two-mode squeezed state to Bob's station via the quantum channel and keeps the other for herself. To generate a data point, they both measure in either the $\hat{X}$ or $\hat{Y}$ quadrature chosen randomly, recording both the outcome and choice of measurement basis. They repeat this until they have acquired $2N$ data points.

Sifting: After the measurements have been performed they communicate their basis choices via the classical channel and keep the on average N data points where both chose the same measurement basis. Data points where different quadratures were chosen can be used in the parameter estimation step.

Parameter estimation: Alice and Bob randomly choose a subset of length L_p of the sifted data points and communicate it over the public channel. Combined with data points where different quadratures were measured they estimate the amount of information leaked to Eve, the expected error rate for error correction, as well as the shared information n per data point. Data points that were communicated are discarded.

Binning: Alice and Bob each convert their analog data points into a bit string of length n by dividing the expected distribution of data points into 2^n bins such that each bin contains the same amount of data points. They obtain a raw key of length $n(N - L_p)$

Error correction: Due to the finite squeeze factor the two raw bit strings are not identical. In this step they use an error correction algorithm, in the process exchanging a subset L_{err} of their bit strings over the classical channel. After this step Alice's and Bob's bit strings are identical assuming an ideal error correction algorithm.

Privacy amplification: To eliminate information known to Eve, Alice and Bob

calculate a secure key length based on the information leaked by the quantum channel and in the previous steps. The protocol succeeds if the secure key length is positive. Given a high loss during transmission it might become negative, in which case the protocol aborts. If successful they apply a two-universal hash function on their raw keys, which they use to shorten the bit strings to the calculated secure key length. It follows from the leftover hash lemma that this reduces the information known to Eve to a small margin ϵ [Imp89]. Given a positive key length, Alice and Bob then share a pair of secret keys they can use for one-time pad encryption or another symmetric key cryptosystem.

2.5 Nonlinear effects

In the presence of an intense light field some materials exhibit nonlinear effects, i.e. the electric field induces a polarization in the medium that includes new frequency components different from the ones incident on the material. To account for the nonlinear response of a material we consider that the electric flux density

$$D(t) = \epsilon_0 E(t) + P(t) \tag{2.96}$$

also contains a polarization vector $P(t)$ that depends nonlinearly upon the electric field. Next we expand $P(t)$ in orders of the electric field

$$\begin{aligned} P(t) &= P^{(1)}(t) + P^{(2)}(t) + \dots \\ &= \epsilon_0[\chi^{(1)}E(t) + \chi^{(2)}E^2(t) + \dots] \end{aligned} \tag{2.97}$$

with $\chi^{(i)}$ the i-th order optical susceptibilities of the material. Linear optical processes are described by the first order $P^{(1)}$. Processes described by higher orders are of particular interest as they can be used to generate light at a different frequency, both higher and lower than the carrier, change photon statistics and thus noise characteristics, and create ultrashort pulses.

In a general description the susceptibility $\chi^{(2)}$ needs to be considered as a tensor. For a given fixed geometry can instead be described by an effective coupling coefficient d_{eff}. With it, we can write the oscillating part from above as

$$P^{(2)} = 2\epsilon_0 d_{\text{eff}}(E_0^2 e^{-i2\omega t} + c.c.). \tag{2.98}$$

Two second order nonlinear processes are of note in the context of this thesis. The first process is second-harmonic generation (SHG) which produces light at double the frequency of the input light. It was used in the experiment to generate a pump beam for the second process of (degenerate) PDC which generated squeezed states. The descriptions of these processes closely follow [Boy08; Wal08].

2.5.1 Second-harmonic generation

Let us consider the second order term of the nonlinear polarization's series expansion from Eq. 2.97 in the presence of an incident optical field $E(t) = E_0 e^{-i\omega t} + E_0^\star e^{+i\omega t}$ at a single fundamental frequency ω. Explicitly expanding the second order term gives

$$P^{(2)}(t) = 2\epsilon_0 d_{\text{eff}}(E_0 E_0^\star + E_0^2 e^{-i2\omega t} + E_0^{\star 2} e^{+i2\omega t}). \tag{2.99}$$

Most notable are the two latter terms that are oscillating at frequency 2ω. These generate a field at the second-harmonic frequency that is proportional to the nonlinearity of the material as well as the power E_0^2 of the incident field. Only the oscillating terms lead to the generation of radiation at the second-harmonic frequency of the fundamental field. In the photon picture, this process combines two photons at the fundamental frequency with energy $\hbar\omega_f$ into one photon at double the frequency and energy $2\hbar\omega$.

2.5.2 Parametric down conversion

It is possible to also drive the inverse process to SHG in a nonlinear medium in which a single photon at the second harmonic frequency 2ω is converted into two photons. Energy is conserved in the process, i.e. $\hbar(\omega_1 + \omega_2) = 2\hbar\omega$, and in general the frequency of the two photons is different. However, let us here only consider the degenerate case where $\omega_1 = \omega_2$.

For a simple model of this process let us consider a nonlinear medium pumped by a strong field at the second harmonic frequency 2ω. We can treat this as a classical field. Interesting effects are present when we describe the fundamental mode quantum mechanically. We can write down the Hamiltonian for the interaction between the two fields

$$H = \hbar\omega \hat{a}^\dagger \hat{a} - i\hbar\frac{\chi}{2}\left(\hat{a}^2 e^{2i\omega t} - a^{\dagger 2} e^{-2i\omega t}\right) \tag{2.100}$$

with the annihilation operator $\hat{a}$ of the fundamental mode and the constant

$$\chi \sim d_{\text{eff}} E_{0,\text{h}} \tag{2.101}$$

proportional to the susceptibility and the amplitude of the harmonic pump field $E_{0,\text{h}}$. We can identify two terms in Eq. 2.100, a time dependent term on the right side perturbing an independent term on the left. By switching to the interaction picture, we can consider the perturbing Hamiltonian

$$H_1 = -i\hbar\frac{\chi}{2}(\hat{a}^2 - \hat{a}^{\dagger 2}) \tag{2.102}$$

without its time dependence ([Sch07] p. 293) . In the interaction picture the equations of motion are given by

$$\begin{aligned}\frac{\mathrm{d}\hat{a}}{\mathrm{d}t} &= \frac{1}{i\hbar}[\hat{a}, H_1] = \chi\hat{a}^\dagger \\ \frac{\mathrm{d}\hat{a}^\dagger}{\mathrm{d}t} &= \frac{1}{i\hbar}[\hat{a}^\dagger, H_1] = \chi\hat{a}.\end{aligned} \tag{2.103}$$

These have the solution

$$\hat{a}(t) = \hat{a}(0)\cosh(\chi t) + \hat{a}^\dagger(0)\sinh(\chi t) \tag{2.104}$$

which is the same form as the transformation generated by the squeezing operator from Eq. 2.61. We can see that the interaction described by the Hamiltonian produces squeezing in the fundamental mode by checking the quadratures form Eq. 2.44 for which the equations of motion read

$$\frac{\mathrm{d}\hat{X}}{\mathrm{d}t} = \chi\hat{X}, \qquad \frac{\mathrm{d}\hat{Y}}{\mathrm{d}t} = -\chi\hat{Y}, \tag{2.105}$$

which have the solutions

$$\hat{X}(t) = e^{\chi t}\hat{X}(0), \qquad \hat{Y}(t) = e^{-\chi t}\hat{Y}(0) \tag{2.106}$$

We see that the amount of squeezing is proportional to d_{eff}, the amplitude of the pump field, and the interaction time.

2.5.3 Phase matching

The given descriptions of the two effects mostly consider conversion at a single position in the nonlinear medium and in isolation. It neglects that the converted field at a given position is a superposition of all partial fields produced at previous positions in regard to the propagation direction. To achieve constructive interference we need to consider the phase that the partial fields accumulate during propagation. While the following only explicitly considers the SHG process, it also applies to the generation of squeezing via degenerate PDC.

Critical phase matching

The phase matching consideration for SHG can be described by considering the wave vectors

$$k_j = \frac{n_j\omega_j}{c}, \qquad j \in \{\mathbf{f}\text{undamental}, \mathbf{h}\text{armonic}\}, \tag{2.107}$$

with refractive index n_j and frequency ω_j, and their mismatch

$$\Delta k = 2k_\mathrm{f} - k_\mathrm{h}. \tag{2.108}$$

The produced wave's amplitude scales according to

$$E_\mathrm{h}(L) = \frac{2i\omega_\mathrm{h}E_\mathrm{f}^2}{k_\mathrm{h}c^2} d_\mathrm{eff}\left(\frac{e^{i\Delta kL}-1}{i\Delta k}\right) \tag{2.109}$$

over the interaction length L. We can obtain the wave's intensity by calculating

$$I_\mathrm{h} = 2n_\mathrm{h}\epsilon_0 c|E_\mathrm{h}|^2 = \frac{8d_\mathrm{eff}^2\omega_\mathrm{h}^2 I_\mathrm{f}^2}{n_\mathrm{f}^2 n_\mathrm{h}\epsilon_0 c^2} L^2 \operatorname{sinc}^2\left(\frac{\Delta kL}{2}\right), \tag{2.110}$$

which for plane waves is optimal for a wave vector mismatch of $\Delta k = 0$ and grows monotonically with the interaction length. To achieve the maximum, the refractive indices for the fundamental and harmonic field must be the same ($n_\mathrm{f} = n_\mathrm{h}$). If we instead consider Gaussian beams the different Gouy-phases of fundamental and harmonic light lead to an optimum at $\Delta k > 0$, such that the harmonic light's phase velocity is slightly higher than the fundamental light's [Las07].

For most materials and wavelength pairs such a refractive index combination is not trivially fulfilled. One common way to match the refractive indices is to make use of a birefringent material for a conversion process in which the converted light is polarized perpendicular to the pump light. The material exhibits an ordinary refractive index $n_o(\omega)$ along its optical axis and an extraordinary refractive index $n_e(\omega)$ on the perpendicular axis. A common way to match the refractive indices is by adjusting the angle between the optical axis and the polarization axis. At a given angle θ the refractive index is given by

$$\frac{1}{(n_\theta(\omega))^2} = \frac{\sin^2(\theta)}{n_e(\omega)^2} + \frac{\cos^2(\theta)}{n_o(\omega)^2}. \tag{2.111}$$

Given a large enough difference between n_o and n_e at each wavelength and a small enough dispersion, i.e. small enough difference between $n_o(\omega)$ and $n_o(2\omega)$, it may be possible to find a θ such that the wave vector mismatch vanishes.

Quasi phase matching

The critical phase matching technique is limited to processes that produce light of perpendicular polarization and to material and wavelength pairings that exhibit suitable refractive index properties. Quasi phase matching enables the use of some processes and materials where this is not the case.

Instead of changing the refractive index, the concept of this technique is to

change the sign of the nonlinear coupling constant periodically over the length of the medium. The period length Λ of these domains is chosen such that the harmonic waves produced at each edge of the domain have a phase difference of 180° with respect to each other. These wave pairs experience destructive interference. Pairs closer towards the middle of the domain experience partial destructive interference. This reduces effective coupling constant d_Q for quasi phase matching compared to the critical one

$$d_Q = \frac{2}{\pi} d_{\text{eff}}. \tag{2.112}$$

The periodic poling assumption leads to an extra term in the derivation of the wave vector mismatch

$$\Delta k_Q = 2k_f - k_h - \frac{2\pi}{\Lambda} \tag{2.113}$$

which allows for the compensation of the different refractive indices of fundamental and harmonic light. Solving for the period length yields

$$\Lambda = \frac{2\pi}{2k_f - k_h}. \tag{2.114}$$

For the crystals used in the experiment made of potassium titanyl phosphate (KTP), and wavelengths $\lambda_f = 1550\,\text{nm}$ and $\lambda_h = 775\,\text{nm}$ we obtain a length of $\Lambda = 25\,\mu\text{m}$.

A comparison of the phase matching cases is shown in Fig. 2.10. While the slope of the critical phase matching curve is larger than that of quasi phase matching, this assumes equal effective nonlinear coefficients d_{eff}. There are some processes that exhibit much larger d_{eff} that require all interacting waves to be polarized in the same direction, and thus cannot make use of critical phase matching.

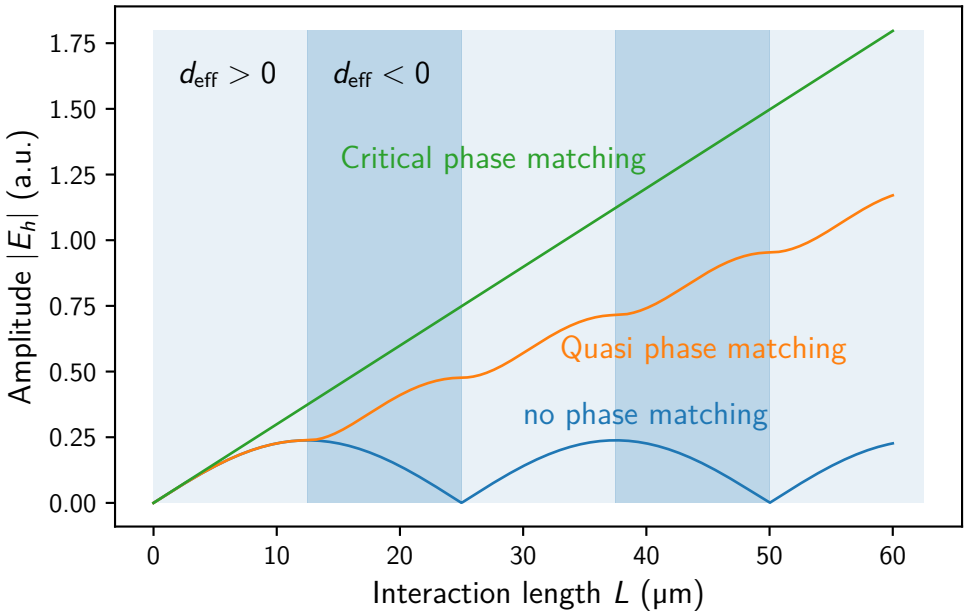

Figure 2.10: Harmonic field amplitude produced by SHG vs interaction length for three different phase matching cases. The sign change of d_{eff} is only applied in the quasi phase matching case. I used the refractive index of KTP and fundamental and harmonic wavelengths of 1550 nm and 775 nm respectively, which were the same parameters used in the experiment.

Chapter 3

High-bandwidth squeezed light

Squeezed light has found a variety of applications in metrology, quantum information, and biomedical fields, one prominent recent example being gravitational wave detection. While a low bandwidth is sufficient for that field, high bandwidth squeezing sources are desirable quantum computing and QKD. Squeezed light has been used in a quantum processor to realize qubits in the form of Gottesman-Kitaev-Preskill (GKP) states [Tak23] and cluster states [Lar19; Yuk08]. In the case of GKP states, a higher bandwidth increases the success rate of state generation. For cluster states, it increases the number of input modes that can be coupled. This in turn increases the computation depth, allowing for more quantum operations to be applied to the input. In a CV QKD protocol squeezed states can be used to generate entanglement in the form of a two-mode squeezed state which I will present in chapter 5. There, a high bandwidth improves the rate at which data points can be produced, increasing the key rate independently of the efficiency per data point.

At 1550 nm, high bandwidth squeezed states were previously reported in a fiber coupled PPLN waveguide, reaching a noise reduction of 6 dB and a bandwidth of 2.5 THz [Kas20], as well as by a previous experiment in this group in a monolithic cavity in periodically-poled potassium titanyl phosphate (PPKTP) coupled to free-space, reaching a noise reduction of up to 4.8 dB with a bandwidth of 1.2 GHz [Ast13]. Capitalizing on the waveguide source's much higher bandwidth requires a detector of similarly high bandwidth which is challenging to realize. Direct detection in the earlier experiments was performed with balanced homodyne detectors with 300 MHz and 1.2 GHz bandwidth respectively. The former experiment demonstrated a quantum noise suppression at higher frequencies by taking an indirect approach, which can not be easily incorporated into a QKD security proof. It thus remains an open question if the superior bandwidth can be utilized.

In the following chapter I present the development of two squeezed light sources based on the latter experiment's free-space monolithic cavity design, as well as two balanced homodyne detectors with a similar bandwidth. The two squeezing sources constituted the EPR entanglement source and were the central piece of this experiment. To detect their output their and the detector's design I iterated upon the previously mentioned works of [Ast13]. The results of this chapter were also published

in [Toh24].

The following chapter is split into three major sections: Sec. 3.1 contains characterization of the improved homodyne detectors. Sec. 3.2 deals with the considerations that went into the squeezing cavities design, including basic optical and mechanical factors, as well as the double resonance condition. In Sec. 3.3 I present the measurement results that characterize the two combined setups of squeezing cavity and detector.

3.1 GHz-bandwidth balanced homodyne detectors

During his thesis at the Leibniz Universität Hannover, Moritz Mehmet developed a homodyne detector with a bandwidth of 1.3 GHz while achieving a dark noise clearance of around 8 dB depending on frequency, which operated at 1064 nm wavelength with 4 mW of LO power, characterized in [Ast13]. Together with Justin Hohmann and Dieter Haupt, I worked on an iteration of this design. We initially planned to improve it in two ways:

Change wavelength from 1064 nm to 1550 nm: We assumed that excess heat was one of the limiting factors in photo diode saturation in the previous design. In the photo detection process, an incident photon excites a valence electron to the conduction band. To drive this excitation, the photon energy needs to be at least equal to the band gap. Any excess energy greater than the band gap is converted into heat. By increasing the laser wavelength at which we operated the experiment and thus reducing the photon energy we could reduce the amount of heat produced in the photo diode. The previous design used high quantum efficiency indium gallium arsenide (InGaAs) photo diodes, sensitive between 900 and 1700 nm with a specified quantum efficiency of 99 % at 1064 nm. We chose the same type of photo diodes for the new design but changed the wavelength to 1550 nm to reduce the heating by excess photon energy. The change was designed to increase the LO power to increases the signal amplitude and therefore the dark noise clearance.

Changing the wavelength was also motivated by lower losses when distributing the entangled states. 1550 nm is the standard wavelength for telecommunication because propagation losses are optimal at this wavelength in single mode fibers, which are low-cost and already in-use for many applications. This allows integration of the QKD protocol into already existing infrastructure.

Improved electronic components and PCB layout: The choice of amplifiers limited both bandwidth and dark noise clearance of the original design. We replaced the ERA-5XSM+ and MAR-6+ amplifiers in the signal path with the higher bandwidth model PSA-39+ which also has slightly more gain. We minimized trace length and added sets of bypass capacitors over multiple decades of capacitance to stabilize supply voltages. For better shielding from stray signals we put the circuits positive

and negative power supplies on two inner layers of the printed circuit board (PCB) with an additional ground layer on its backside. The updated circuit design is shown in the appendix in Fig. C.1.

As we needed one detector at Alice's and Bob's station respectively to measure the two parts of the entangled state Sophie Verclas and I each assembled and characterized one detector of the new design. I performed linearity measurements for both by blocking the signal field and sending only an LO onto the detector while increasing its power by factors of two. The measurement data is shown in Fig. 3.1.

For a shot noise limited detector, Eq. 2.72 shows that the homodyne detector's output signal should be directly proportional to the LO amplitude α. A scaling of more than 3 dB indicates the presence of other noise sources, while sub-3 dB scaling indicates saturation of the electronics which is expected at high LO powers.

The measured data additionally contains the detectors dark noise. To check if the detector is shot noise limited and behaving linearly, I subtracted the dark noise level (measured separately) then checked for 3 dB scaling. For a visual reference, the previous measurement is plotted relative to the noise level of the data with the highest LO power at which each detector still behaves linearly in Fig. 3.2.

This measurement shows, that the new detector design is sensitive up into the 1.5 GHz range. The two detectors we built behave slightly differently. Alice's detector shows 3 dB scaling up to 12 mW of LO power, while Bob's detector shows this scaling only up to 6 mW over most of the spectral range. I assume the sub-3 dB scaling at high LO power was caused by saturation of the photo diodes. Due to the higher LO power Alice's detector exhibits a higher dark noise clearance than Bob's over most of the detection band, with each showing 8 dB and 6 dB respectively. As the dark noise clearance was best at these LO powers, I performed the following measurements at these powers.

The spectrum contained numerous peaks from electronic signals picked up by the detector. The source of some peaks is known, e.g. the phase modulation for the Pound-Drever-Hall (PDH) error signal of this experiment's mode cleaning cavity at 18.75 MHz and SHG at 101.75 MHz. The source of other narrow peaks in the spectrum is not known, but likely to be caused by similar signals from surrounding laboratories. The large broad peak in the dark noise of both detectors around 1250 MHz and 1050 MHz is likely due to a self-induced oscillation in the detectors amplifiers.

The two detectors were sensitive up to a different maximum of 1.4 GHz and 1.7 GHz respectively. The different frequency dependence between Alice's and Bob's detectors stems from variations in the electrical components. In high frequency applications even small changes in capacitance affect the frequency response of a circuit. It is possible to match the response of both detectors to each other by

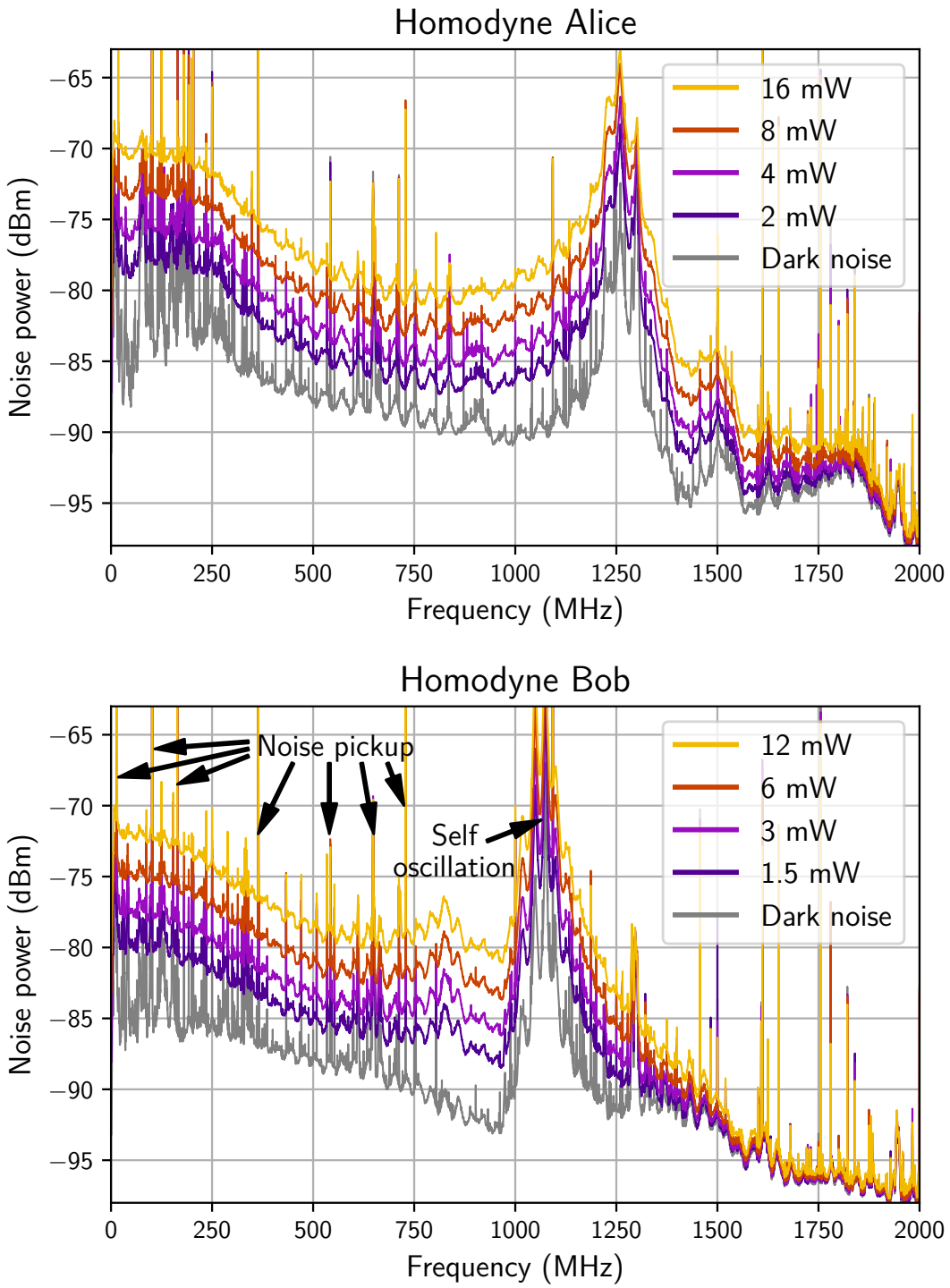

Figure 3.1: Shot noise measurement of Alice's and Bob's homodyne detector while doubling LO power until the detector no longer behaved linearly, up to 2 GHz sideband frequency. Acquired via spectrum analyzer, RBW = 300 kHz.

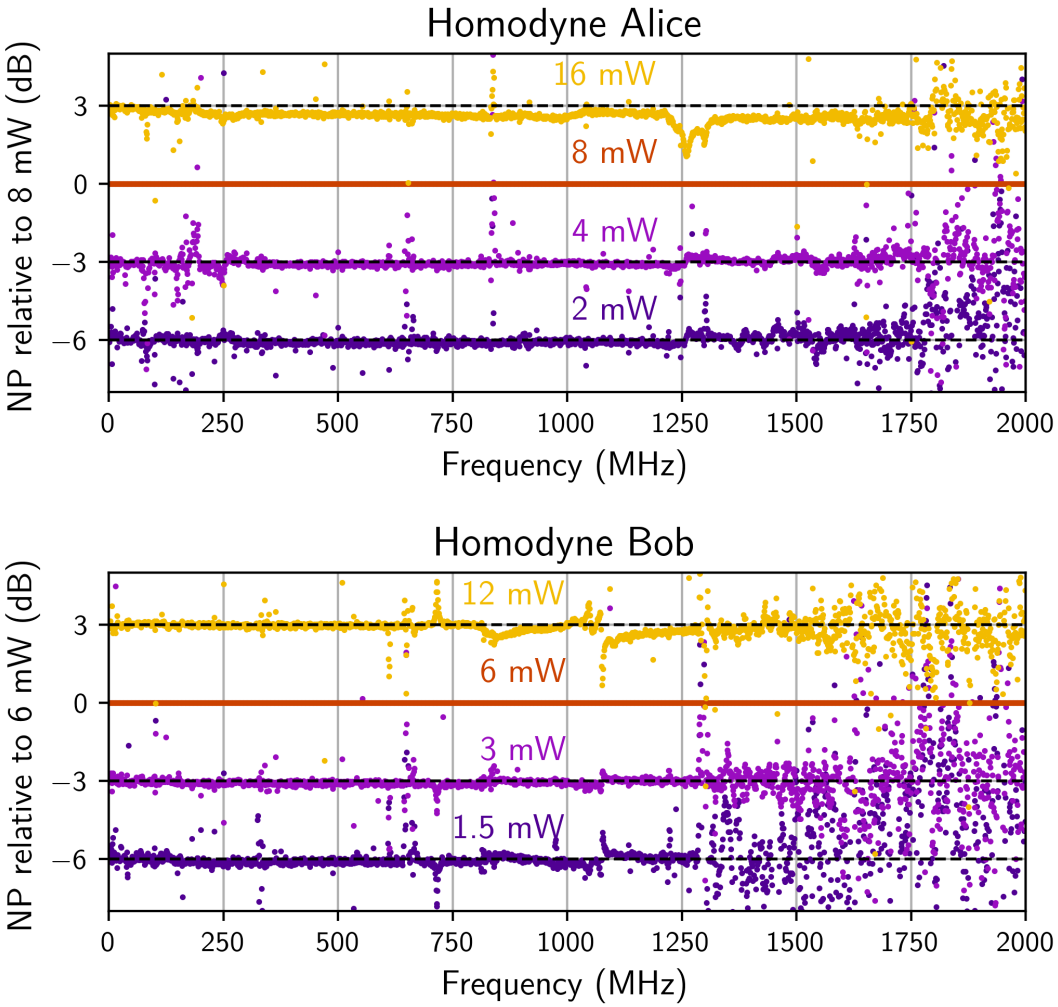

Figure 3.2: Shot noise measurement from Fig. 3.1, dark noise level subtracted and normalized to the shot noise at the highest, still linear LO power.

preselecting components. In our application an equal response was not critical, so I chose to keep the detectors with this performance.

I performed this linearity measurement near the end of the experimental part of this thesis in late 2023. I built Alice's detector at the beginning of the project in 2020 and characterized it multiple times. Over time I observed a decrease of the maximum LO power the detector could handle before it saturated from 24 mW to 8 mW. The source of this effect is unclear. I suspect that it is either due to aging of the photo diodes or the high frequency electronics used for signal amplification in the detectors output.

Compared to the previous design we were able to increase the detection bandwidth of the detector by more than 200 MHz. However, while we were able to increase the usable LO power before the detector saturated, the dark noise clearance was not

improved by this change. For the purpose of broadband entanglement detection we were satisfied with this result.

3.2 Squeezing cavity design

The goal of producing a high bandwidth EPR entangled state can be achieved by overlapping two squeezed states. Highly squeezed state can be efficiently produced in a nonlinear cavity by using the cavity-enhanced PDC process. To produce a squeezed field at the fundamental wavelength, here 1550 nm, a nonlinear crystal was pumped with light at the first harmonic wavelength at 775 nm. The squeezing cavity produced the squeezed state by degenerate cavity-enhanced PDC below the laser threshold. To define the spatial and frequency mode of the squeezed state and increase the effective nonlinearity of the material it is useful to design an optical cavity around the nonlinear medium.

3.2.1 Optical cavity parameters

The goal of a high bandwidth squeezed state constrains the design space of the squeezing cavity. The bandwidth of a squeezed state generated in a cavity is proportional to its linewidth $\Delta\nu$. The cavity linewidth in turn depends on the FSR ν_{FSR} and the finesse $\mathcal{F}$:

$$\Delta\nu = \frac{\nu_{\mathrm{FSR}}}{\mathcal{F}} \sim \frac{1/L}{R} \tag{3.1}$$

which each contain one free parameters. The FSR is inversely proportional to the round trip length L, the finesse is monotonically increasing with the reflectivity of the cavity's mirrors $R \sim R_1 R_2$. Thus, the squeezing bandwidth can be maximized by either reducing the reflectivity or the round trip length.

Minimizing the round trip length can be achieved by reducing the cavity length. The shortest practical cavity design has the crystal itself directly coated at the end faces, forming a monolithic cavity. Combined with a short crystal length this gives a short round trip length.

While a low finesse cavity is desirable from a bandwidth standpoint, it comes with the drawback of an increased threshold power for the pump field, since lower reflectivities increase the round trip losses. The closer to the threshold that the squeezing cavity operates, the larger the squeeze factor of the state it generates, so it should be as close to the threshold as possible. One way to compensate the increased threshold power due to the low fundamental finesse is to also have a cavity for the pump field, making it doubly resonant. The cavity for the pump field effectively enhances the circulating power which the nonlinear medium experiences at a given incident pump power, reducing the requirement on the external pump power provided by an SHG.

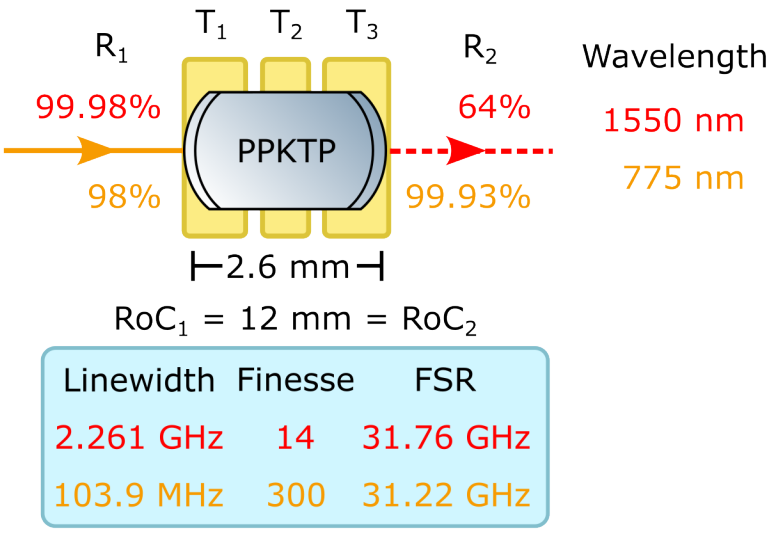

Figure 3.3: Cavity parameters of the monolithic squeezing cavities. Also shown are the temperature zones T_1 to T_3. The edge temperature zones each have a width of 0.8 mm, the middle zone has a width of 0.6 mm with gaps of 0.2 mm in between.

The above considerations led us to iterate on a previous design of a monolithic squeezing cavity [Ast13] from our group. Three unused nonlinear crystals made of periodically PPKTP remained from that experiment which were already cut to 2.6 mm length and polished with 12 mm radius of curvature (RoC) on both end faces. One of the end faces was also coated with power reflectivities of $R_{1,1550\,\mathrm{nm}} = 99.98\,\%$ and $R_{1,775\,\mathrm{nm}} = 98\,\%$. When choosing the reflectivity values of the second coating I considered that a small part of the pump field at 775 nm should be transmitted through the cavity for stabilizing both the cavity length and the relative phase between the two squeezed light sources that produce the entanglement. I chose a reflectivity of $R_{2,775\,\mathrm{nm}} = 99.93\,\%$ for the pump field's highly reflective coating, slightly lower than the typical highly reflective coating. This results in a transmissivity of the linear cavity of about $T_{775\,\mathrm{nm}} = 13\,\%$ on resonance. For the fundamental field I chose a reflectivity of $R_{2,1550\,\mathrm{nm}} = 64\,\%$ resulting in a cavity linewidth of $\Delta\nu_{1550\,\mathrm{nm}} = 2.261\,\mathrm{GHz}$. The cavity parameters are summarized in Fig. 3.3.

3.2.2 Three temperature zones

Directly coating the second end face of the crystal has the advantage that the cavity is more stable against vibrations compared to a hemilithic design. However, the cavity length is no longer a degree of freedom to be used for the purpose of alignment and tuning the cavity length onto resonance. Instead, I fine-tuned the cavity length by adjusting the crystal's temperature thereby changing its optical length via the thermo-optic coefficient $\frac{\mathrm{d}n}{\mathrm{d}T}$.

Typically, the crystal temperature is used to fine tune the domain length of the periodic poling to optimize phase matching for the conversion process in the squeezing cavity. Another monolithic cavity experiment [Hag24] used a design with three distinct temperature zones to adjust the quasi phase matching and cavity length independently of one another for a 9.3 mm long cavity. The nonlinear interaction is proportional to the intensity of the pump. Therefore, good phase-matching and subsequently the correct temperature is required around the focus, as the intensity is highest there. In a symmetrical setup it is located in the center. Due to lower intensities at the edges of the crystal an imperfect quasi phase matching has a negligible impact on the conversion process and can thus be used to tune the cavity length to achieve resonance without affecting the conversion.

To realize this temperature concept, I adapted the oven design from [Hag24] to these smaller crystals. The mechanical oven design shown consisted of the nonlinear crystal placed on the top side of a PCB as shown in Fig. 3.4 with three copper pads for the three temperature zones. These pads were each connected to a larger copper area with a Peltier element on the bottom side of the PCB for heating. The larger areas on top were connected to the bottom of the PCB with vertical interconnects to ensure good thermal conductivity. The temperature of each pad was monitored via a negative temperature coefficient (NTC) resistor positioned close to the crystal and connected to the large copper areas. Each temperature was feedback controlled to a constant temperature that could be adjusted by changing the control loop's set point. Due to the much lower thermal conductivity of the PCB in comparison to copper (around $1.1\,\mathrm{W\,m^{-1}\,K}$ for FR-4 laminate [Sar90] vs $401\,\mathrm{W\,m^{-1}\,K}$ [Sta]) there was little thermal cross talk in the plane of the PCB.

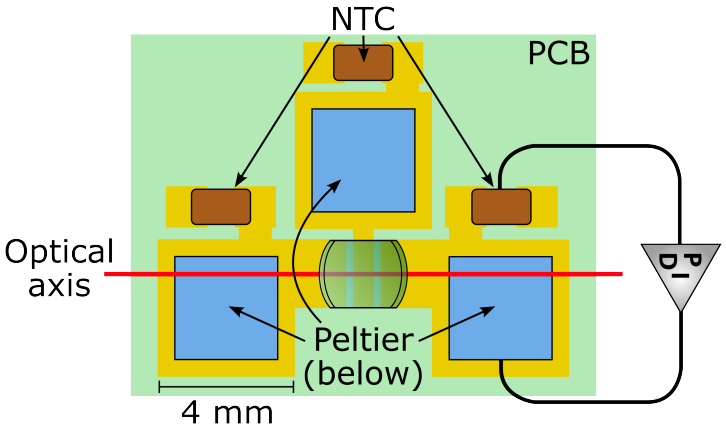

Figure 3.4: To scale top view of the squeezer oven. The nonlinear crystal (green) and NTC resistors (brown) were placed on the top side of the PCB, the Peltier elements (blue) on the bottom. All three copper pads were feedback controlled to a constant temperature, though only one is shown.

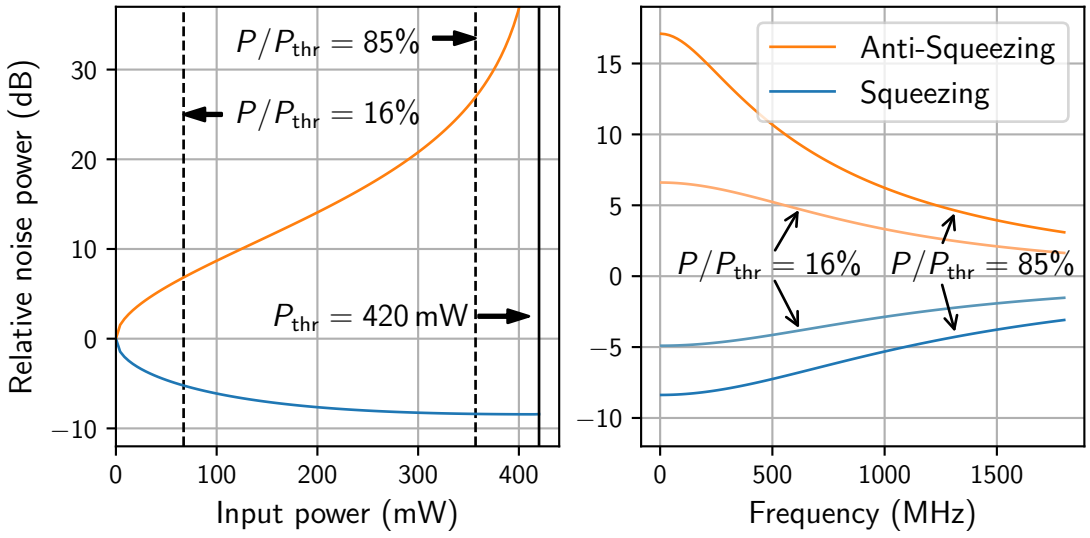

Figure 3.5: Left: Dependence of detected squeezing on the pump power at a low sideband frequency. Right: Detected squeezing by sideband frequency for two different pump powers. Simulated using NLCS.

3.2.3 Simulating pump threshold and squeezing bandwidth using NLCS

To further analyze the nonlinear cavity's performance I simulated it in the software NLCS [Las10]. With it, I examined the expected pump threshold and squeezing performance by frequency for the cavity parameters given above. The simulation required to additionally specify the material's nonlinearity which I chose close to the value from [Ast11] to be $\chi^{(2)} = 6.5 \times 10^{-12}\,\mathrm{m\,V^{-1}}$. The results of the simulation are displayed in Fig. 3.5. The percentages in the subscript denote the relative pump powers P/P_{thr} at which a squeezing factor similar to the measurements in Sec. 3.3 is reached.

The pump power dependence simulation yielded a pump threshold of 420 mW for the above cavity parameters. With the given detection efficiency of $\eta = 85\,\%$ the maximum squeezing value of −8.4 dB is achieved just below the threshold. However, from experimental experience it is unrealistic to achieve it, either because the cavity becomes unstable or phase noise couples anti-squeezing into the squeezed quadrature. The squeeze factor already reaches a similar level of −8 dB at 250 mW pump power. With the SHG limited to producing around 1 W of pump power, this threshold power allowed for the simultaneous operation of both squeezing cavities with a margin for deviations of the pump threshold.

From the simulation of squeezing vs sideband frequency we can see what squeeze factor we can reach at high frequencies. At 1 GHz it is −5.3 dB in the high pump power

case ($P/P_{\text{thr}} = 85\,\%$) and $-2.9\,\text{dB}$ in the low pump power case ($P/P_{\text{thr}} = 16\,\%$). Increasing the squeeze factor further at this high of a sideband frequency would require a larger cavity bandwidth.

It should be noted, that the pump power and frequency dependence plots in Fig. 3.5 are not in agreement with each other with respect to the produced anti-squeezing value at a given pump power. Also, the simulations are not in agreement with the theoretical model from Eq. 2.77. However, I believe it still gives some information about both the expected pump threshold and the shape of the frequency dependence. The values obtained here should be considered to have a large uncertainty.

3.2.4 Double resonance of a monolithic cavity

As stated in the previous section the crystals' end faces were coated such that they formed a cavity both for harmonic pump light and fundamental light. In this configuration both cavities are coupled and need to be on resonance at the same time. In the case of a cavity that contains a dispersive medium this is nontrivial. In the following I will first establish some basic definitions for a double cavity, then calculate the double resonance points that were available given the parameter ranges of the devices, and later present the double resonances that I achieved for the two cavities.

Resonances of a double cavity

Let us consider a double cavity defined as a set of two mirrors that are reflective for both a fundamental wavelength λ_f and its first harmonic $\lambda_h = \lambda_f/2$. The mirrors are separated by a length L and form a geometrically stable linear cavity, i.e. the mirrors are aligned on the optical axis and have RoC such that the cavity is stable. The resonance condition for each constituent cavity is

$$L_{\text{res}}(m) = \frac{m\lambda}{2n} \tag{3.2}$$

with the refractive index n, the wavelengths in vacuum λ and a positive integer m, which indicates the number of the resonance. Let me define this as the length

$$L_{\text{FSR}}(\lambda) = L_{\text{res}}(m+1) - L_{\text{res}}(m) = \frac{\lambda}{2n} \tag{3.3}$$

between two successive resonances, or the cavity length change equivalent to one FSR. For the trivial example of a double cavity without a medium ($n = 1$), the length change between two resonances for fundamental and harmonic is only different by a factor of two ($L_{\text{FSR}}(\lambda_h) = L_{\text{FSR}}(\lambda_f)/2$). The resonances of the fundamental coincide with every second resonance of the harmonic, as visualized in Fig. 3.6a. This also holds true for a cavity with a medium, as long as its refractive index is the same for

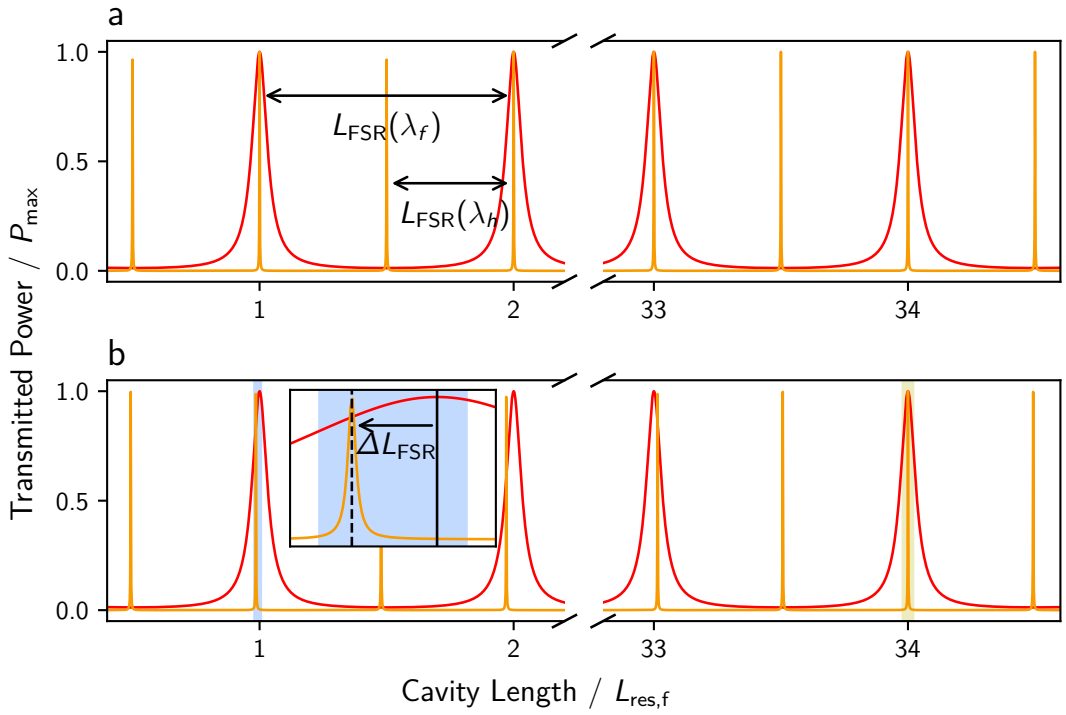

Figure 3.6: Resonances of a double cavity as a function of cavity length (a) with a dispersionless medium ($n_f = n_h$) and (b) with a medium with dispersion ($n_f < n_h$) inside the cavity. Fundamental resonances are shown in red, harmonic in orange. The different refractive indices for fundamental and harmonic wavelength cause a shift ΔL_{FSR} between their resonances. The values correspond to the cavity parameters given in the previous section.

both wavelengths, as is the case for example in a nonlinear cavity that uses critical phase matching.

In the general case of a double cavity with a dispersive medium the resonance length is no longer the same. The difference in resonance lengths of the second harmonic resonance relative to the fundamental leads to a shift between the peak position equal to

$$\Delta L_{\mathrm{FSR}} = 2L_{\mathrm{FSR}}(\lambda_h) - L_{\mathrm{FSR}}(\lambda_f) = \frac{\lambda_f(n_f - n_h)}{2n_h n_f}. \tag{3.4}$$

For materials that are typically used the refractive index at the harmonic is larger than at the fundamental wavelength, meaning that the shift is negative, as visualized in Fig. 3.6b. In this case there are more than two harmonic resonances per fundamental resonance.

For higher order of resonances the fundamental and harmonic resonances shift apart from each other by a multiple of the order $m_f \Delta L_{\mathrm{FSR}}$. Here m_f denotes the

order of the fundamental resonance. It is minimal when the shift is equal to the length of one FSR of the harmonic, $m_f \Delta L_{\mathrm{FSR}} = L_{\mathrm{FSR}}(\lambda_h)$ at which point the double cavity becomes resonant for both fundamental and harmonic. We can calculate the resonance order as $m_f = 0.5 n_f/(n_f - n_h)$. Double resonance occurs periodically approximately every integer multiple $j \cdot m_f$. Relating that back to the cavity length, we can see that the double cavity is double resonant every

$$L_{\mathrm{DR}} = m_f \frac{\lambda_f}{2}. \tag{3.5}$$

Performing this calculation for the double cavity parameters in the experiment, with a length of $L = 2.6\,\mathrm{mm}$ and PPKTP as the medium with the refractive indices from the z-axis Sellmeier equation provided in [Kat02]. Using these values double resonance occurs every $m_f = 34.5$ fundamental resonances or every 26.7 µm when only changing the cavity length.

Accessible double resonances

Changing a monolithic cavity's length after manufacturing is difficult. An approach to influence the resonance condition by pressing onto it with a piezoelectric actuator has been tried in [Ast15]. The main contribution in this case would however likely be from a change of the refractive index due to mechanical stress along the optical axis rather than from a length change. This brings up the question, what other parameters are available to tune the resonance conditions of fundamental and harmonic cavity?

The refractive index can be tuned more easily by adjusting the crystal temperature. As we can see from Eq. 3.5, the temperature contributes to ΔL_{FSR} via the thermo-optic coefficient $\partial n/\partial T$ as well as the relative thermal expansion of the material $(\partial L/\partial T)/L$. Changing the laser wavelength directly changes the double resonance through its dependence on λ_f and also through the refractive indices via both wavelength's $\partial n/\partial \lambda$.

In the following I estimate the impact of the wavelength and temperature changes that can be achieved with the components from this experimental setup. The crystal temperature could be changed between 20 °C and 80 °C and the wavelength by ±200 pm around the fundamental wavelength ($\Delta\lambda = 400\,\mathrm{pm}$). With the Sellmeier equations for KTP from Ref. [Kat02] we can calculate both $(\partial n/\partial \lambda)|_{\lambda=\lambda_f} = -2.3 \times 10^{-2}\,\mathrm{nm}^{-1}$ and $(\partial n/\partial T)|_{\lambda=\lambda_f} = 1.2 \times 10^{-5}\,\mathrm{K}^{-1}$ at $\lambda_f = 1550\,\mathrm{nm}$. A linear thermal expansion coefficient of $(\partial L/\partial T)/L = 2 \times 10^{-8}\,\mathrm{K}^{-1}$ has been reported for KTP in Ref. [Smi16]. With the parameter ranges above we get total relative changes

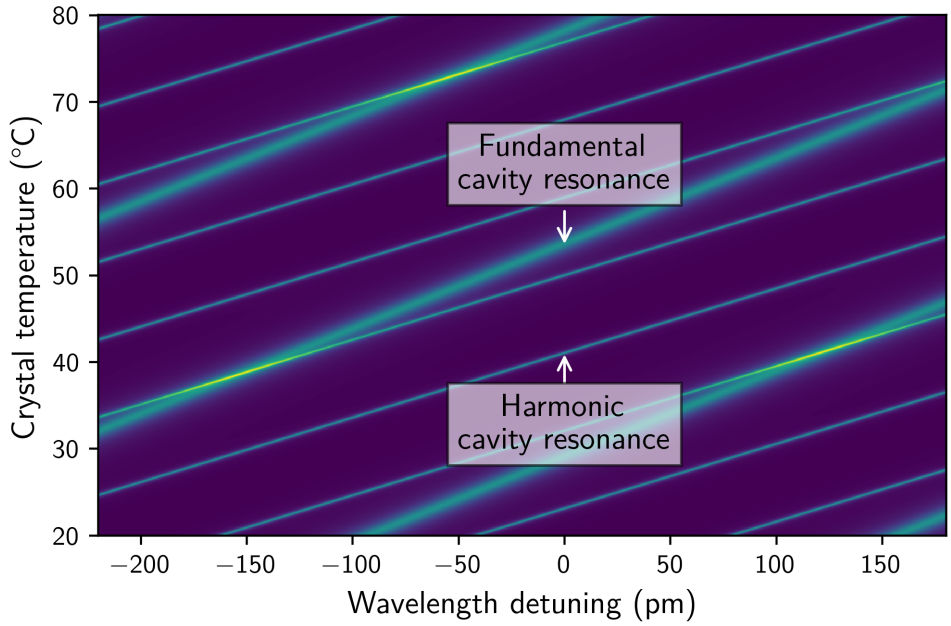

Figure 3.7: Calculated transmission for fundamental and harmonic wavelengths of the double cavity. The three wider lines correspond to the lower finesse fundamental cavity, the thin lines correspond to the harmonic cavity. Double resonance occurs at the crossing points. For better visualization the harmonic linewidth was increased.

of

$$\begin{aligned}
\frac{\partial n}{\partial T} \cdot \Delta T &= 7.2 \times 10^{-4}, \\
\frac{1}{\lambda} \cdot \Delta\lambda &= 2.6 \times 10^{-4}, \\
\frac{\partial n}{\partial \lambda} \cdot \Delta\lambda &= 9.2 \times 10^{-6}, \\
\frac{1}{L}\frac{\partial L}{\partial T} \cdot \Delta T &= 1.2 \times 10^{-6}.
\end{aligned}$$

We can see that the thermo-optic coefficient and the wavelength change offer a similar adjustment range.

To further evaluate the impact those parameters have on double resonance I plotted the fundamental and harmonic resonances of a double cavity with the given parameters and tuning ranges in Fig. 3.7. We can see that in the tuning ranges we expect to see 2 or 3 tuples (λ, T) where double resonance occurs. The position of the double resonances in this parameter space, and thus the number that is visible, also greatly depends on the microscopic crystal length. Changing it shifts the resonances' position in this periodic pattern.

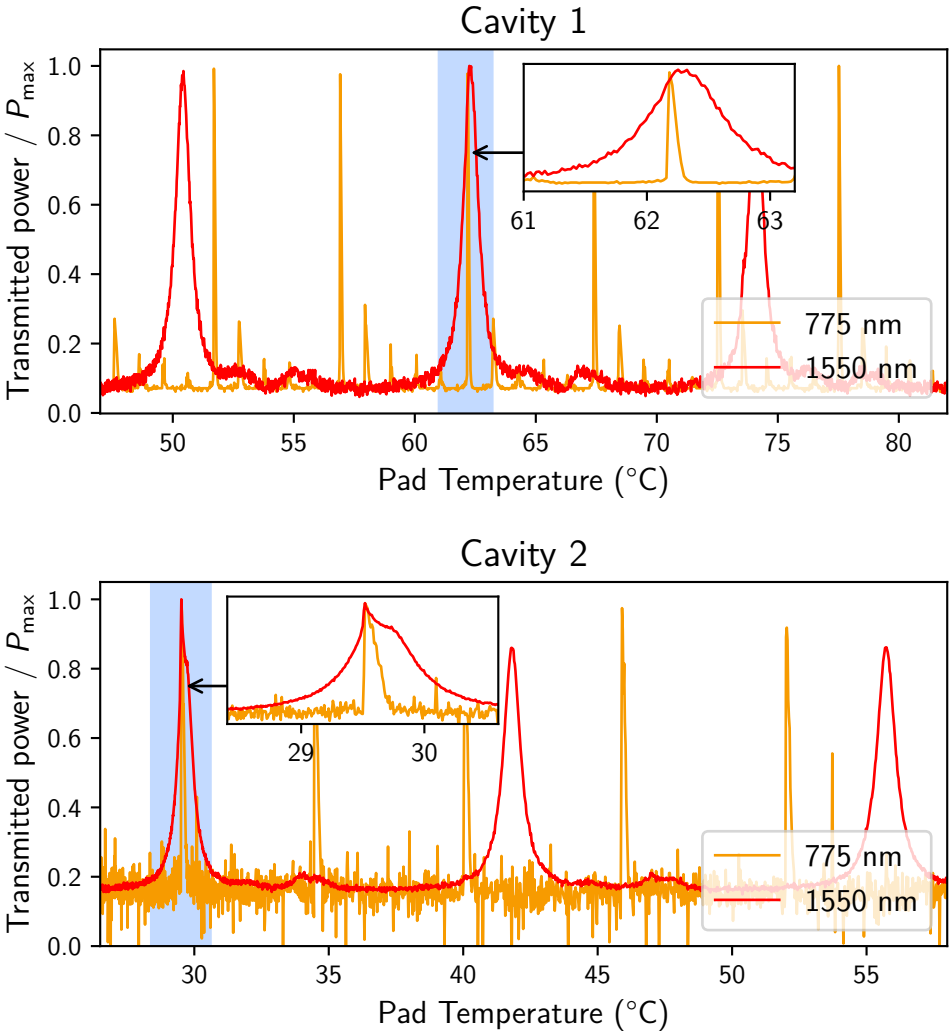

Figure 3.8: Double resonance measurement of the two monolithic squeezing cavities at low powers with the laser wavelength set to 1550 nm + 144 pm. Shown are the photo diode voltages that are proportional to the transmitted fundamental and harmonic light.

Double resonance measurement

In the experiment I used the crystal temperature to drive the cavity on resonance while keeping the laser wavelength constant. To find a good laser wavelength in the first place I changed it in 20 pm steps and scanned the crystal temperature of 1 for each setting. I monitored the transmitted power of the pump beam at 775 nm and a control beam at 1550 nm both sent onto the cavity from the $R_{775\,\mathrm{nm}} = 98\,\%$ side. I found a double resonance at two wavelength detunings at 144 pm and −200 pm, the measurement at 144 pm is shown in Fig. 3.8.

Experimentally I only found two double resonances compared to the three that

were expected from the previous calculation. This was likely due to a different cavity length compared to the design. This essentially shifted the whole picture from Fig. 3.7 to a higher temperature. As the highest temperature that could be achieved with the Peltier elements was around 80 °C, I could not observe the other double resonance points.

After performing this measurement the laser wavelength was set to (1550 + 0.144)nm and I used the crystal temperature to control the cavity resonance. Since the laser wavelength was now fixed I did not have this degree of freedom to control the double resonance of cavity 2. I chose 144 pm since I also observed a double resonance of cavity 2 there as can be seen in Fig. 3.8. It occurs at a lower temperature than for cavity 1, likely again due to a difference to the design cavity length. As the temperature at which double resonance occurs also set the phase matching temperature, the different values had implications for the crystals' maximum effective nonlinearity that could be achieved. For more detailed discussion see Ch. 3.3. As the two squeezing cavities were only required to have a double resonance at the same laser wavelength, I did not look for other double resonances of cavity 2.

The sensitivity of the photo diode that detected the harmonic light of cavity 2 was lower than for cavity 1. As a result I had to use a larger harmonic light power to observe the resonance peak while still obtaining a worse signal-to-noise ratio. Notably though this had the interesting side effect that I could observe parametric amplification of the fundamental light at the double resonance, which deformed the fundamental resonance peak.

3.2.5 Thermal effects near cavity resonance

In the double resonance measurements in Fig. 3.8 I could also observe thermal effects in the harmonic light. Due to the higher power used to pump it, these effects were more prominent for cavity 1 throughout operation and caused problems with its stability. During production of squeezed light the cavity was pumped with power on the order of 1 W. The pump cavity finesse caused the intra cavity power to build up to 185 W when the cavity was on resonance. With a beam diameters smaller than 70 µm over the whole cavity length, absorption in the bulk material and the coatings generated enough heat to significantly change the temperature and thus refractive index similar to the mechanism used to tune the cavity to be resonant.

When scanning the cavity resonances at high pump powers, depending on which way the pad temperature changed I could observe one of two effects visible in Fig. 3.9. When changing the pad temperature from high to low as in the double resonance measurement from Fig. 3.8, as the cavity approached a resonance peak more light power coupled into the cavity, leading to a temperature increase due to absorption. The heating from absorption counteracted the external cooling, causing a broadening of the 'hot' flank of the resonance. After reaching the peak, intra cavity power and

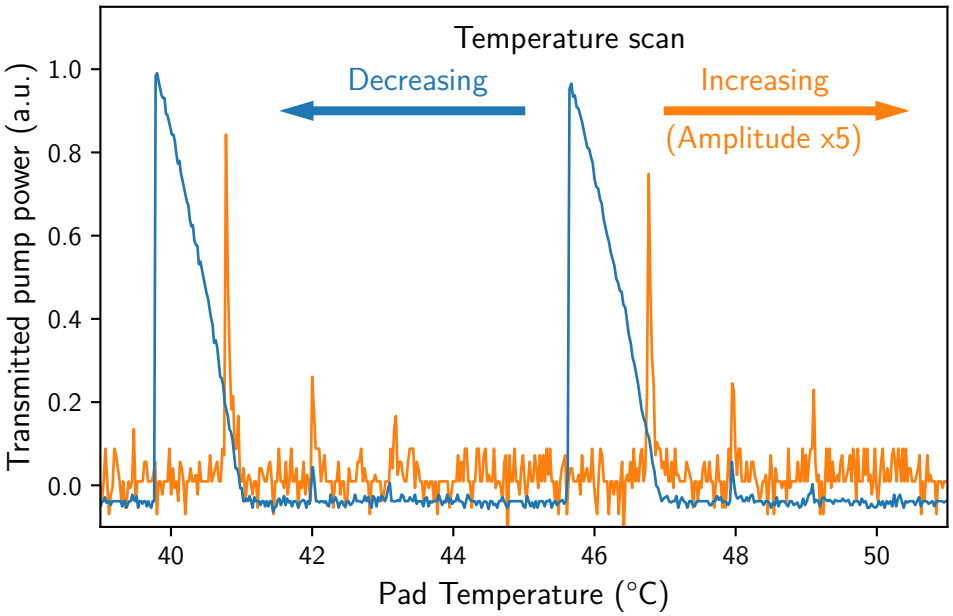

Figure 3.9: Scan of the cavity pump resonances acquired by either increasing or decreasing the pad temperature of cavity 2. The increasing temperature trace's amplitude is scaled up by a factor of 5.

thus absorbed power decreased leading to less heating which quickly pushed the cavity off resonance, creating a steeper 'cold' flank. Scanning in the other direction the same effects lead to the opposite outcome with regard to the peak shape. To summarize, external heating and heating caused by absorption compounded when approaching from the cold flank to cause a narrowing of the peak, while on the hot flank they counteracted, broadening the peak.

Comparing ascending and descending scan we can see a difference in position of the resonance peak evidenced by the maximum transmitted power. This is because of a difference between the measured temperature of the copper pads on which the crystal rests and the crystal temperature around the optical axis. In theory the crystal temperature at each resonance peak should be the same. The shift is caused by absorption heating the crystal, not detected at the copper pad, leading to a difference between crystal and measured pad temperature. The shift is much more pronounced in the decreasing temperature scan as the counteracting external cooling and absorption heating keep the cavity near the resonance longer.

The cavity resonance could only be approached from the hot side. There, external cooling compensated the added heat from absorption. However, the cavity was still highly unstable when close to the resonance peak. For all following measurements I operated the cavities at a value around 75 % of maximum transmitted pump light.

Furthermore, I implemented a control loop to stabilize the cavity close to resonance

by actuating the pad temperature. The error signal was generated in a PDH scheme using the transmitted light. As a modulation was already present on the 1550 nm light used to pump the SHG at a frequency within the SHG's linewidth, the modulation was converted by the SHG and was still present on the squeezing cavities' pump light. In transmission of the cavities, a photo diode could detect the modulation and demodulate it to create an error signal to feed back onto the pad temperature. Due to the inherent slowness of the temperature actuation this feedback loop could only prevent the cavity from drifting off the lock point over long timescales on the order of seconds. The monolithic cavity design made the cavity sufficiently stable once it was near resonance and in equilibrium.

3.3 Detection of GHz bandwidth squeezed light

I used a reduced setup shown in Fig. 3.10 to characterize the two squeezed light sources. I sent the output of each squeezing cavity onto a BHD where it was superimposed with a LO on a 50/50 beam splitter. To ensure a good spatial mode overlap between LO and squeezed field prior to every measurement I matched both beams to a reference cavity which could optionally be reached via a flip mirror. For alignment of the squeezed field I switched on a 1550 nm alignment beam which coupled in through the highly reflective side of the squeezing cavity. By tuning the cavity on resonance, it transmitted a part of the adjustment beam in the cavity mode, allowing to then match that mode to the reference cavity. After alignment, I removed the flip mirror and turned off the adjustment beam.

The pump light for the squeezing cavities was supplied by an SHG, which converted up to 900 mW of 1550 nm light derived from the same source laser as the LO to 775 nm. To drive the cavity onto the previously observed double resonance I adjusted its temperature going from high temperature to low, while monitoring the transmitted pump power. Once the cavity was near resonance I verified it was the correct resonance peak by checking the homodyne signal for squeezing.

I characterized both squeezing cavities in separate setups using the two different detectors previously characterized in 3.1, resulting in different dark noise levels (homodyne Alice measured cavity 1, Bob measured cavity 2). I captured the homodyne signal with a spectrum analyzer and performed a zero span measurement at 30 MHz center frequency shown in Fig. 3.11 as well as a full span spectrum measurement up to 1.8 GHz shown in Fig. 3.12 for each squeezing cavity.

3.3.1 Squeezing measurements

Before each measurement I adjusted the homodyne readout phase θ_p by hand via a piezo actuated mirror in the cavity's pump beam. I performed all measurements with-

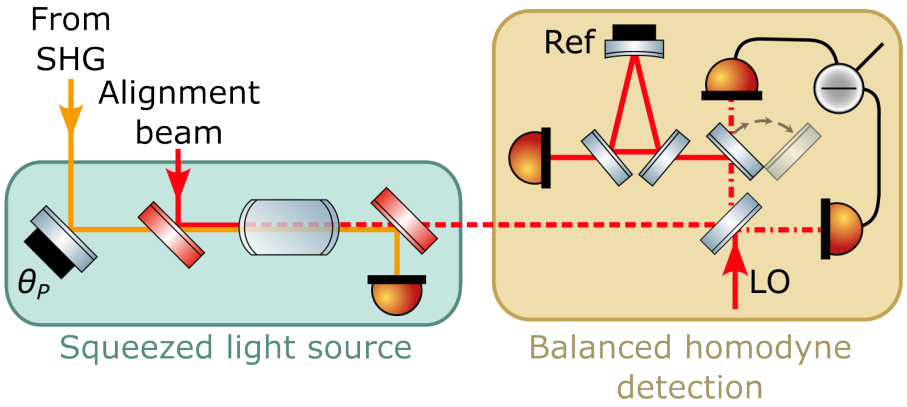

Figure 3.10: Setup for alignment of the squeezed light source. For alignment, I inserted a flip mirror in front of one photo diode, turned on the alignment beam and tuned the squeezing cavity on resonance so the alignment beam was transmitted. I then successively matched alignment beam and LO to the reference cavity (Ref). For squeezed light generation only 775 nm light was sent into the squeezed light source and the flip mirror was removed.

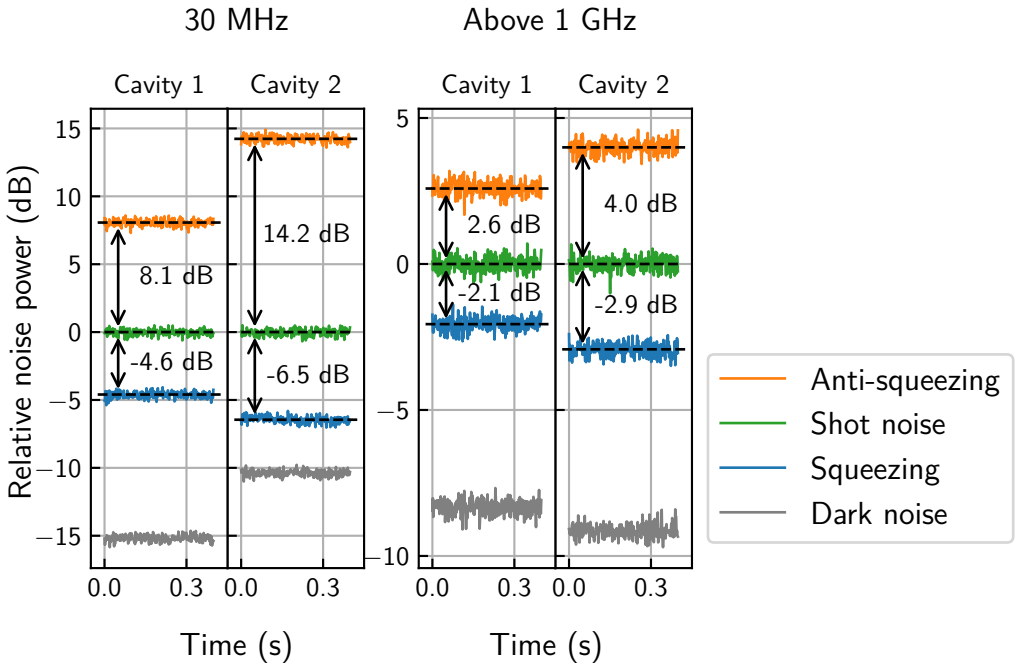

Figure 3.11: Squeezing zero span measurements of both squeezing cavities at 30 MHz and above 1 GHz sideband frequency (cavity 1: 1100 MHz, cavity 2: 1001 MHz) normalized to shot noise. All given (anti-) squeezing values have a standard deviation of 0.2 dB given by the standard deviation of the line. I chose different sideband frequencies above 1000 MHz because of features in the detector's sensitivity. Acquired via spectrum analyzer, RBW = 300 kHz.

out active phase stabilization, which could potentially lead to phase drifts. However, the experiment was contained in a closed-off housing, which minimized turbulence. I typically observed the phase being stable over multiple seconds. As the time required per measurement was less than a second, I assumed that the readout phase was constant during that time. The pump powers used were 600 mW for cavity 1 and 250 mW for cavity 2, which was close to the powers that were available during simultaneous operation.

In Fig. 3.11 I show zero span measurements of both squeezing cavities in the MHz and GHz region. At first glance, cavity 2 produces more squeezing at a lower pump power at both frequencies. Early on in the experiment I was able to reach the threshold power of cavity 2 at around 400 mW at which point it produced a bright field. For cavity 1 I was unable to experimentally reach the threshold due to instability of the cavity and thermal effects at high pump powers. It was potentially also limited by the maximum pump power of around 900 mW the SHG could provide.

I expected the threshold powers to be the same due to the identical cavity design, though we can see from the above measurement that this is not the case. The threshold condition is reached when the gain per round trip is equal to the losses per round trip, with the gain depending on the effective nonlinearity of the material as well as the finesse for the pump field, and the loss depending on the reflectivities at the squeezing wavelength as well as absorption in bulk material and coating. The most likely cause is that the value I assumed for the effective nonlinearity deviated from the real one. Presumably, the actual value was lower due to bad phase matching either from the crystal cut or poor adjustment of the phase matching temperature.

For maximum effective nonlinearity, the periodically poled material should be cut at the middle of a domain (neglecting phase flips or changes upon reflection due to propagation into the coating, etc.), so that the reflected beam effectively continues to see the same periodic poling. If the cut is at a boundary between two domains such that the reflected beam propagates twice through a domain poled in the same direction, then the field which is generated when propagating in one direction is out of phase with the field that is generated after the reflection, which leads to them interfering destructively. In this extreme case the effective nonlinearity of the material would be reduced to zero. Generally, a crystal cut away from the middle of a domain reduces its nonlinearity. This might have contributed to the lower effective nonlinearity of cavity 1, though I estimate the phase matching temperature discussed in the following to have a higher impact.

I initially planned to use the outer temperature zones to keep the cavity on resonance and the central temperature zone to adjust the quasi phase matching. From the squeezing measurement, however, it seemed the crystal was too short to achieve this decoupling. The center and edge temperatures could be independently adjusted, each compensating a change in the other regarding the cavity resonance.

Despite this, changing the center temperature did not affect the squeezing value. I assume this was the case because the intensity stayed mostly constant over the crystal length as it was shorter than the Rayleigh length of 4.6 mm. To be able to decouple the temperatures I assumed that the majority of the conversion process takes place in the center. As it instead happens over the whole crystal length, temperature changes at any position affect both phase matching and resonance. Thus, the crystal temperature was essentially one degree of freedom instead of two as initially assumed, which was required to adjust the cavity resonance. This gave a fixed temperature that was not optimized regarding quasi phase matching.

The manufacturer specified a phase matching temperature of $(40 \pm 10)\,^{\circ}\mathrm{C}$. For cavity 2 the double resonance temperature of 29 °C worked out to be close to this value, while for cavity 1 it was at 62 °C. I conclude that this mismatch of phase matching temperatures caused the lower effective nonlinearity of cavity 1.

Shown in Fig. 3.12 is the two squeezing cavities' performance by sideband frequency. Both cavities produce squeezing well into the GHz range. In the lower frequency range up to 200 MHz both spectra contain multiple sharp peaks that were caused by pickup of electronic signals. One part of the spectrum of each cavity contains an unexpected decrease of both squeezing and anti-squeezing level relative to the shot noise around 1 GHz and 820 MHz respectively. In the absolute noise level measurement, which is not shown here, it can be seen that both the shot noise and squeezed noise levels increase, while the dark noise level remains the same. Therefore, I assume that there was a phase difference between the two photo diode signals of each homodyne detector in this frequency range, which affected their balanced subtraction.

The dark noise clearance relative to the shot noise level of both detectors was between 6.5 dB in the 400 MHz to 600 MHz range and 10 dB below 200 MHz and around 1 GHz. Towards high frequencies the homodyne detectors are no longer sensitive.

When observing the detected squeeze factor by frequency range we can see that the squeeze factor for cavity 1 in the low frequencies up to around 800 MHz was limited the most by low parametric gain. In the same frequency range cavity 2 was limited by detection loss. For both cavities the distance between dark noise and squeezing was low and potentially limits the system from achieving higher squeezing values in the future. For frequencies above 1 GHz the limiting factor for both cavities was their optical bandwidth. Performance in this range can only be significantly improved by changing the cavity parameters.

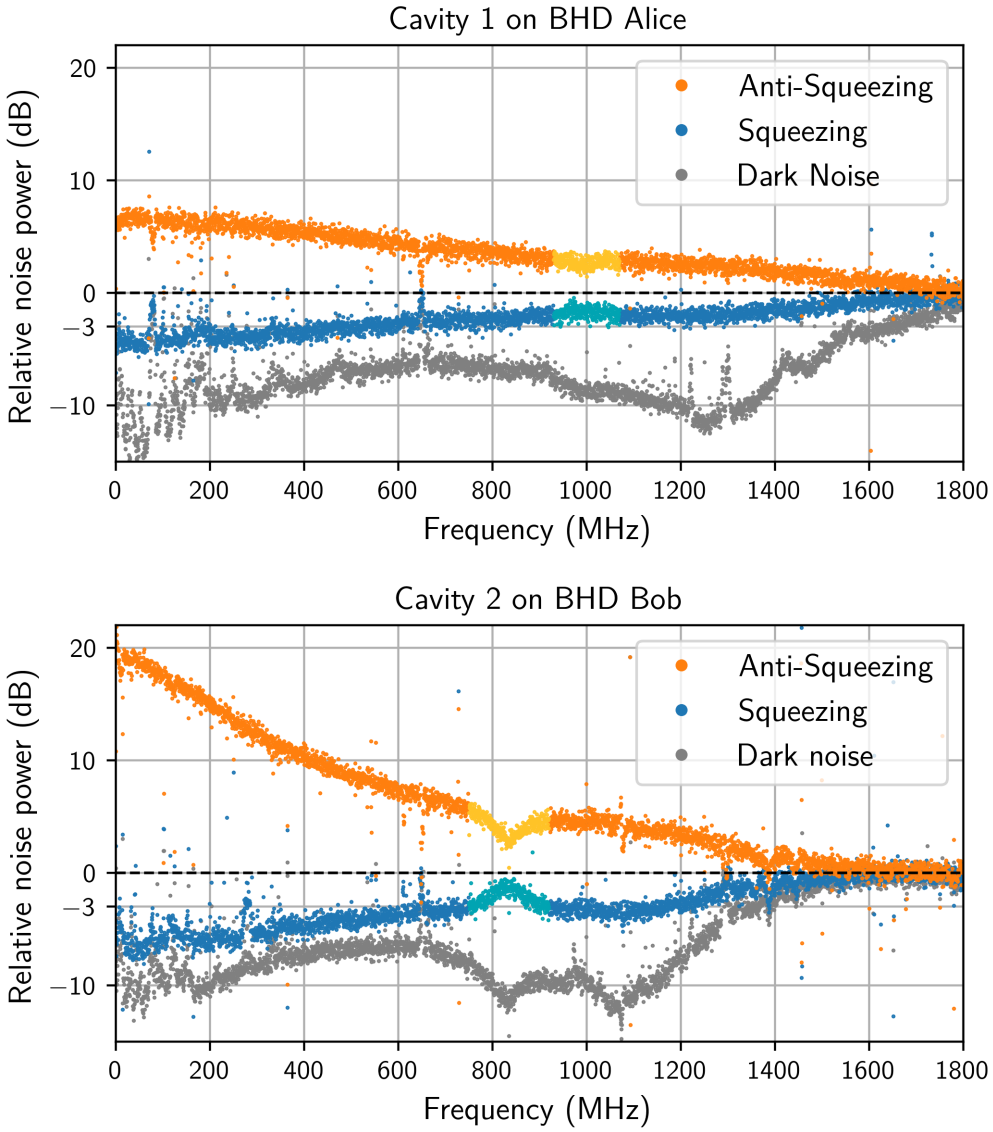

Figure 3.12: Full span squeezing measurements up to 1.8 GHz. Marked in another color is a deviation from the expected behavior which becomes more apparent when compared to the theoretical model in Fig. 3.13. At frequencies higher than 1.8 GHz both homodyne detectors are no longer sensitive. Acquired via spectrum analyzer, RBW = 300 kHz.

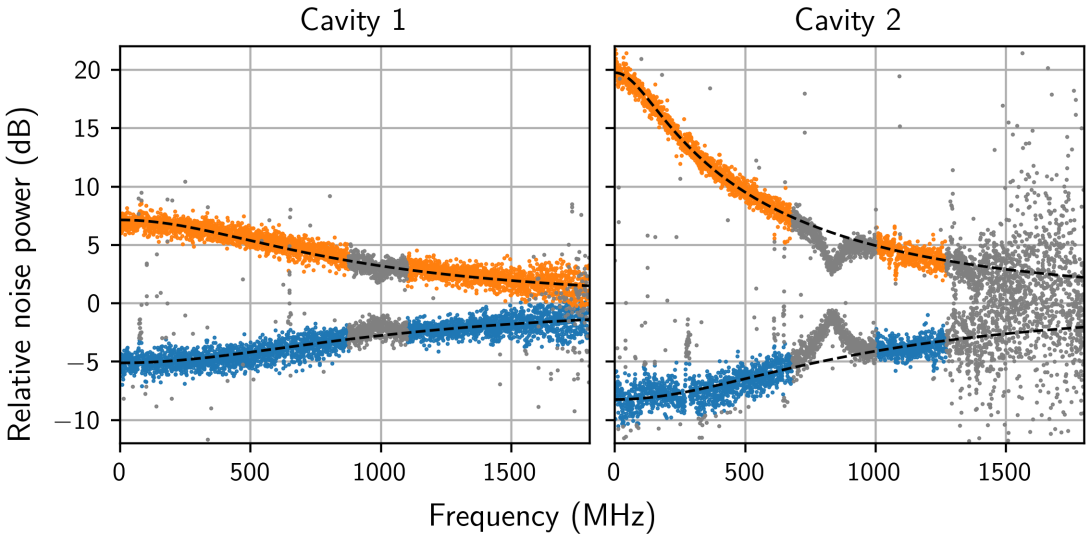

Figure 3.13: Squeezing full span measurements dark noise corrected and fitted with a theoretical model (dashed). Data points shown in gray are excluded from the fit due to features in the detector's sensitivity. Above 1.3 GHz cavity 2's dark noise clearance was negligible, resulting in high uncertainty after subtracting it.

3.3.2 Fit of theoretical model

In Fig. 3.13 I fitted the squeezing spectra with the function for the (anti-) squeezed variance by sideband frequency from Eq. 2.77, which reads

$$\mathrm{Var}(\hat{X}(\omega))_\xi = 1 \mp \eta \frac{4P/P_{\mathrm{thr}}}{(1 \pm P/P_{\mathrm{thr}})^2 + 4(\omega/\delta\nu)^2}. \tag{3.6}$$

I considered the pump power relative to the pump threshold P/P_{thr}, total detection efficiency η, and the cavity linewidth γ as free parameters. Here the upper sign corresponds to the squeezed quadrature $\hat{X}$ and the lower to the 90° out of phase anti-squeezed quadrature $\hat{Y}$, each at the sideband frequency ω. To be able to fit I first subtracted the dark noise level from all traces. Then I fitted both the squeezed and anti-squeezed trace simultaneously in linear units. As the anti-squeezing values were much larger than the squeezing values, minimizing the distance between the fit function and data points would be biased towards fitting the anti-squeezing data. To account for this effect, I scaled down the weight of its residual in the fitting algorithm. The fit results are given in table 3.1. Lastly I excluded data from the fit where there were electronic noise peaks from pickup, the prominent sensitivity change in the GHz region and at very high frequencies where there was little dark noise clearance.

From the fit I obtained a total detection efficiency η of 83.2 % and 85.7 % respectively. The known losses of the components used (imperfect HR and AR

	Cavity 1	Cavity 2
η	$(82.8 \pm 1.6)\,\%$	$(85.8 \pm 1.1)\,\%$
P/P_{thr}	$(42.15 \pm 0.79)\,\%$	$(82.58 \pm 0.10)\,\%$
γ	(2.053 ± 0.064) GHz	(1.750 ± 0.013) GHz

Table 3.1: Optimal parameters obtained from the curve fit of the squeezing spectra. The given uncertainties only include the uncertainties obtained from the fit.

coatings, photo diode quantum efficiency, and cavity escape efficiency) amount to 2 % of loss. Combined with an unbalance splitting of 0.1 % and the mode overlap of squeezed field and LO of $>$98 %, which I determined using the reference cavity during alignment, this gives an expected loss of 6 %. The source of the remaining 12 % loss is not known. A likely candidate is a worse mode overlap during operation compared to alignment. I considered a thermal lensing effect due to the high intra cavity pump power, which I tried to observe by checking the alignment on the reference cavity via the alignment beam while simultaneously sending in pump light. However, no higher order modes were visible. It might be plausible that the mode overlap inferred from the reference cavity mode matchings was not representative of the actual overlap. Another candidate would be a higher propagation loss caused by absorption or scattering on dirty optics on the way to the detector. Although the experiment was set up in a clean room, over time the optics still collected some dust on their surfaces. Intermittently we also noticed some liquid droplets on the coatings of both squeezing cavities. After some testing I found the source to be thermal paste used to ensure good thermal contact between Peltier elements and PCB. I removed the thermal paste and cleaned the coating, however some residue might still be present on the end faces and cause additional absorption.

For the generation of the entangled state both squeezing cavities ideally need to produce squeezed states with the same squeeze factor. Since the squeeze factor produced by cavity 1 was mostly limited by its effective nonlinearity rather than loss I chose not to investigate the unaccounted losses further. To produce the entangled states I operated cavity 2 at a lower pump power to match cavity 1's squeeze factor.

Comparing the fitted cavity linewidths to the calculated linewidth of 2.261 GHz we can see a major deviation even between the two squeezing cavities. We expected to see similar linewidth as both cavities were designed to be identical. The parameters that contribute to the linewidth are cavity length, reflectivity of the coupling mirror at 1550 nm, and intra cavity loss. Assuming the cavity length to be accurate within 100 µm, it alone can not explain a deviation of 10 %. The reflectivity was specified to be within one percentage point of the requested 64 % reflectivity. This also does not change the linewidth enough. As the linewidth is smaller than expected, the reflectivity would need to be higher than assumed by five percentage points to explain the value of cavity 2. Assuming this would be the case, the higher losses of cavity

1 compared to 2 would modify the linewidth in the right direction, increasing the linewidth. An increased loss of 5 %, if we model this as lowering the reflectivity of the $R = 99.98\,\%$ back mirror, would cause a broadening of the linewidth by 10 %. Assuming cavity length and reflectivity each vary in the right direction as well as an additional 5 % intra cavity loss for cavity 1 as obtained from the fitted spectra, this would explain the difference between the calculated cavity linewidth and the observed ones. Assuming the reflectivities to deviate the same seems reasonable as both crystals were coated in the same run. However, a deviation of 5 % with a manufacturer given uncertainty of 1 % seems unlikely.

Calculating the pump threshold was difficult because I could not accurately determine how much of the pump light coupled into the squeezing cavities. Due to the mentioned thermal effects I could not operate the cavities on resonance but had to settle on a lower value I estimated to be 75 % of the peak value. Determining the peak value itself however was difficult as well. For cavity 2 I could observe the highest transmitted power while driving the cavity on resonance, coming from the hot side of the resonance peak. Doing the same procedure for cavity 1 yielded a sharp peak while jumping over the cavity resonance which I could not accurately resolve, similar to the difference in peak height between the two directions from Fig. 3.9. I can thus only estimate the pump threshold of cavity 2 with good certainty to be around $(370 \pm 50)\,\mathrm{mW}$. This is in agreement with an observation we made early on where we could observe bright light being produced from cavity 2 for a short time while we drove it onto the resonance, while at the same time measuring high anti-squeezing values around 25 dB. The cavity was highly unstable and jumped off resonance. It is also in agreement with the value obtained from the simulation with NLCS from Ch. 3.2.3. The lower threshold of cavity 2 and its agreement with the simulation leads me to the conclusion that its temperature at which it was doubly resonant coincided well with the optimal phase matching temperature.

For cavity 1 by using the pump power given above and the relative pump threshold from the fit I obtain a threshold power in the order of $(1.5 \pm 0.5)\,\mathrm{W}$ assuming that the cavity was at 75 % of peak transmission. This value agrees with the observation that we were not able to reach its threshold but contains high uncertainty.

Ultimately the squeeze factor that could be used for entanglement generation was limited by cavity 1. For the entangled state the squeeze factor of both input states should be identical. I realized this by operating cavity 2 at a lower pump power, which limited it to a squeeze factor of $-5\,\mathrm{dB}$ for the input states.

3.3.3 Loss introduced by unwanted second harmonic generation

During operation of cavity 1 with high pump power we noticed that the cavity produced ultraviolet light in addition to the squeezed light at 1550 nm. This was also noticed in other experiments, e.g. [Ast15]. We observed it on a piece of paper, which showed fluorescence in the presence of UV light, and later attempted to quantify the amount with a power meter. We used a mirror with high reflectivity for 775 nm to separate pump light from UV. As the mirror's reflectivity for UV was not specified we estimated it by the brightness of the fluorescent spot on paper. From the power meter reading in transmission of the mirror we estimated the UV light's total power as about 2 mW. The UV light is most likely produced via second-harmonic generation from the 775 nm pump light. Under this assumption it would be at 387.5 nm wavelength which we could not verify experimentally. For cavity 2 we could also observe UV light generation although at reduced power due to lower pump power.

The generation of UV light in the cavity gives more possible explanations for the worse performance of cavity 1. Blue-light-induced infrared absorption (BLIIRA) has been reported in KTP [Wan17], which is a process where absorption in the infrared range is increased due to the presence of light in the blue or UV range. Furthermore, UV absorption itself can lead to damage in the nonlinear material in the form of to gray tracking, in particular due to the small beam waist of the UV light and the resulting intensity around 110 $\mathrm{W/cm^2}$. It might be another loss channel I did not consider previously that contributes to the unexplained 12 % loss in the squeezing measurement. As the produced UV light power was greater for cavity 1, loss would be higher for cavity 1 and would thus contribute to the 5 % increased loss of cavity 1 compared to cavity 2.

3.4 Conclusion

In summary, we assembled two homodyne detectors with an improved detection bandwidth compared to the previous design of 1.5 GHz. Using these I was able to detect squeezed states with a squeeze factor of more than −3 dB over a continuous bandwidth of over 700 MHz, as well as quantum noise reduction below the shot noise up to a sideband frequency of 1.4 GHz simultaneously produced by from two monolithic cavities.

There are a number of future improvements that would increase the light source's performance as well as their ease-of-operation. Right now the setup is limited in its squeezing factor by the low effective nonlinearity of cavity 1. It could be increased by exchanging its nonlinear crystal for one that can be operated closer to the design phase matching temperature. This would remove the current limit on the squeeze

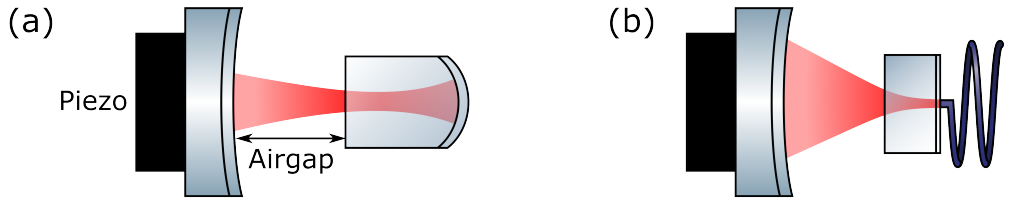

Figure 3.14: Schematic structure of: (a) a hemilithic cavity, (b) a fiber coupled hemilithic cavity.

value and would set the new limiting factor to be the detection efficiency. With optical contributions to the detection efficiency (imperfect mode matching, splitting ratio, photo diode quantum efficiency, etc.) being low, I suspect an undiscovered effect is currently introducing detection loss.

The next biggest opportunity to increase the detected squeezing is increasing the dark noise clearance of both detectors. Over most of the detection band the difference between squeezing and dark noise levels was between 3 and 4 dB for both detectors, the best value was at 30 MHz for cavity 1 with 10 dB. At a difference of 3 dB, half of the total noise power originates from detector dark noise. For a good direct squeezing measurement a difference of 10 dB between squeezing and dark noise would be desirable. This experiment would benefit from the design of a detector which can achieve such a high clearance over a bandwidth of more than 1 GHz. Due to the complex behavior of GHz bandwidth signals a detector with greatly improved performance exceeded the scope of this thesis. A dedicated electrical engineering study might yield improved results.

If a greater squeezing bandwidth is of interest, the finesse of the cavity for the fundamental light could reasonably be lowered by reducing the coupling mirror's reflectivity further. The increased pump power required could still be supplied by the current setup. The design threshold power of a single cavity could reasonably be increased to around 1 W, allowing for a cavity linewidth that is around a factor of two higher.

For easier integration into other experiments it would be desirable to further improve the squeezing cavity's handling. Scanning the cavity length via the temperature is slow, making alignment time-consuming. This weakness of a monolithic cavity could be alleviated by a different cavity architecture. Using a hemilithic design would allow the use of a piezo element for faster length adjustments, also giving the opportunity to implement a more robust length control loop.

In a hemilithic (or semi-monolithic) design, the nonlinear cavity is formed between the one reflectively coated end face of the nonlinear crystal and a coupling mirror on the other side, with an air gap between crystal and mirror (cf. Fig. 3.14a). The mirror position can be actuated via piezo on a micrometer scale to adjust the cavity length much faster than what is possible with temperature adjustment in the monolithic

design, enabling length stabilization onto resonance in the kilohertz regime. The separate mirror also decouples actuation of cavity length and the phase matching condition. The hemilithic design opens up another degree of freedom: The size of the air gap, to adjust the double resonance condition through changes on the millimeter scale due to dispersion in air (wavelength dependent refractive index) even after fabrication of the crystal.

Despite these advantages, developing an appropriate hemilithic design remains challenging. To achieve a high bandwidth, the cavity needs to be of similar length as the current design of around 3 mm depending on the crystal length and air gap size with the additional constraint of the focus being contained inside the crystal. The short length limits the air gap tuning range and in turn the adjustment range of the double resonance. Shifting the focus towards one end of the cavity, as is the case in a hemispherical cavity, might allow to increase the tuning range. In this case, the zone of highest intensity would be near one end of the cavity and the crystal length could be reduced in favor of a bigger air gap tuning range. Overall a hemilithic design seems promising for a high bandwidth squeezed light source as it has advantages for many major issues that monolithic cavities currently have.

When considering a complete redesign of the squeezing cavity, the next step for easy integration into other setups would be to directly couple the produced squeezed light into an optical fiber, as shown in Fig. 3.14b. In a hemilithic design this could be achieved by bonding the fiber directly to the nonlinear crystal to ensure mechanical stability of the connection and coating the interface between fiber and crystal to form one cavity mirror. The cavity mode would need to be matched to the fiber mode with high efficiency, requiring a waist size equal to its mode field diameter of $w_0 = 4.6\,\mu\text{m}$ at the fiber end face. The small waist close to the fiber lends itself to a design where the nonlinear medium is placed as close as possible to the fiber, so that the high-intensity zone is directly exploited for conversion. It follows from the Rayleigh length of 43 µm that the nonlinear medium should be kept short, on the order of a few 100 µm, as the conversion zone is localized around the focus region. This either leaves space for an air gap between medium and a coupling mirror to adjust cavity double resonance if desired, or allows for a very short cavity with high squeezing bandwidth.

Chapter 4

Improved quantum random number generator

Random number generators (RNGs) play a critical role in both classical cryptography and quantum key distribution, where in both cases their property to produce random outcomes, i.e. outcomes that are unknown to any other party, fulfills the requirement for information that is secret from any outside parties. In particular for the QKD protocol I focused on in this thesis, an RNG is required at both Alice's and Bob's station to switch between the two measurement bases at random.

A general abstract model of an RNG, as shown in Fig. 4.1 and has been described in [Kil11], consists of some randomization function that is deterministic but chaotic in its output values in combination with a non-deterministic entropy source. This condition is not satisfied in a basic software-based RNG, which lacks an internal entropy source. To generate random numbers, it instead takes an internal state with some initial entropy and applies the randomization function to it. The generator then updates its internal state by feeding back the generated number in some way. Such a generator can produce a lot of seemingly random outputs by expanding the randomness of the internal state. It is however deterministic given the initial state. If an adversary were able to invert the RNG's randomization function, the only remaining randomness would be that of this seed. Thus, once the RNG has put out more random numbers than the entropy of its initial state, it is potentially insecure, making purely software-based RNGs a poor choice for cryptographic applications.

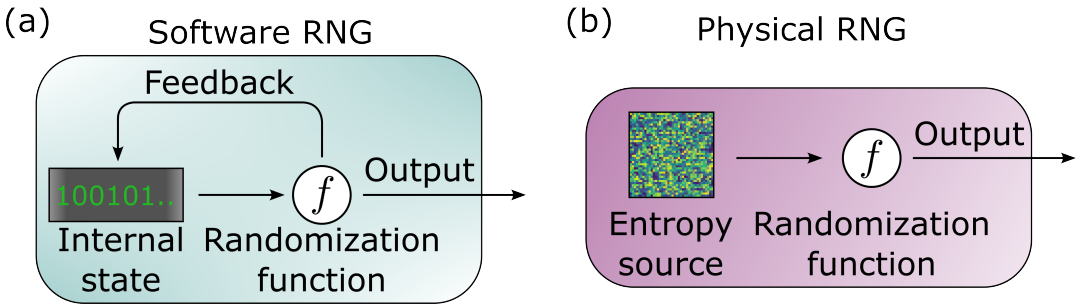

Figure 4.1: Conceptual model of a (a) software RNG and (b) physical RNG.

One approach to achieve a cryptographically secure RNG is to replace or refresh the internal state. The class of physical random number generators achieve this by measuring a chaotic physical system and incorporating it as an entropy source. From a security standpoint quantum systems are one of the best suited physical system for this, as their randomness stems from fundamental uncertainty of quantum states as postulated by quantum mechanics. The subclass of generators based on these systems are trivially called QRNGs.

For physical RNGs the randomization function could in principle be omitted, since its application does not generate any entropy and might instead obscure an insufficient actual entropy content. Some post-processing might however be required to produce uniformly distributed random numbers, as for example many physical processes produce a Gaussian distribution. In the abstract RNG model any post-processing of the measurement outcomes would be considered to be part of the randomization function. To exclude the function's effect on the generator output, the physical system's entropy should be quantified before post-processing and the generator should require only a minimal amount to produce a random output.

A QRNG design has been proposed that can be realized with components already present in this experiment [Gab10]. The basic design shown in Fig. 4.2 consists of a balanced homodyne detector with a blocked signal port such that it performs quadrature measurements $\hat{X}_\phi$ of the vacuum state $|0\rangle$. As a measurement of the vacuum state's quadrature has a non-vanishing variance, it produces random measurement outcomes. The relatively small amount of required components — a laser, a detector, and data acquisition (DAQ) — make the setup simple. As the measured quantum state is the ground state, it is robust and easily prepared experimentally by blocking the detector's signal port. Combined with high bandwidth detectors and a fast DAQ system the design offers potential for a high random number generation rate despite its relative simplicity. Setups with rates of multiple $\mathrm{Gbit\,s^{-1}}$ have been implemented in several experiments [Sym11; Zhe19; Geh21] with varying amounts of use of post-processing and security assumptions, as well as in this group during my master's thesis with a real-time number generation rate of $41.6\,\mathrm{Mbit\,s^{-1}}$ with minimal post-processing. Over the course of an unfinished bachelor's thesis and a master's thesis that I supervised we implemented improvements to the setup that demonstrated that an increase of the data rate to $120\,\mathrm{Mbit\,s^{-1}}$ is feasible. The former thesis focused on improving the existing setup, while the latter implemented a new approach, in which the vacuum state in the signal port was replaced by an anti-squeezed state.

4.1 Improvement of the previous design

In the QRNG setup originally presented in my master's thesis, a balanced homodyne detector generated a signal from a shot noise measurement with a blocked port

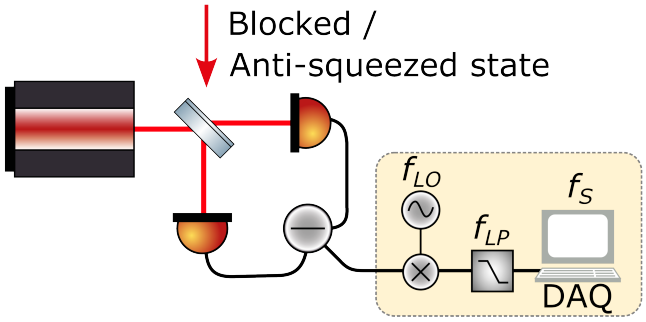

Figure 4.2: QRNG setup based on a balanced homodyne detector. For the results shown in Ch. 4.1 the signal port was blocked, while for the results of Ch. 4.2 an anti-squeezed state was sent into the signal port. The electronic post-processing steps (yellow box) vary depending on the implementation. Shown here are a low-pass filter, frequency generator, and RF mixer.

[Toh19]. The detector's output signal was demodulated to select a frequency band with minimal electronic noise. The data was acquired with a DAQ card with a 16 bit resolution and 250 MHz sampling rate. It was downsampled in post-processing by a factor of 6 to compensate for the reduced bandwidth due to the low-pass filter, which produced a uniform frequency distribution. The acquired data followed a Gaussian distribution, which was converted to a uniform one by dividing the Gaussian distribution into 2^n bins of equal probability, which allowed for the generation of $n = 2$ bits of information per measured sample, similar to the process shown in Fig. 4.3. This was reduced to $n = 1$ to eliminate the remaining classical information by bit-wise addition of half of the data to the other half.

The system's total number generation rate was the product of effective sampling rate and bits of quantum information per sample. The former is the more impactful factor overall as it can be increased linearly by increasing DAQ system's sampling rate in combination with the detector's bandwidth. The potential sample generation rate is maximized when the detector's bandwidth is close to the DAQ system's Nyquist rate.

Increasing the amount of usable entropy per sample requires increasing the quantum-noise-to-electronic-noise ratio and only scales logarithmically with this ratio. The information contained in each sample can be modeled as composed of a quantum part from shot noise and a classical part from electronic noise. As it comes from a classical source, the classical part is assumed to be deterministic and known to an adversary and therefore cannot be used for random number generation. This essentially limits the size of the smallest bin dividing the Gaussian distribution. To quantify the classical information I calculated the Shannon entropy when applying the same binning to quantum noise and electronic noise.

Let me give an intuitive argument: We can model a measurement outcome as

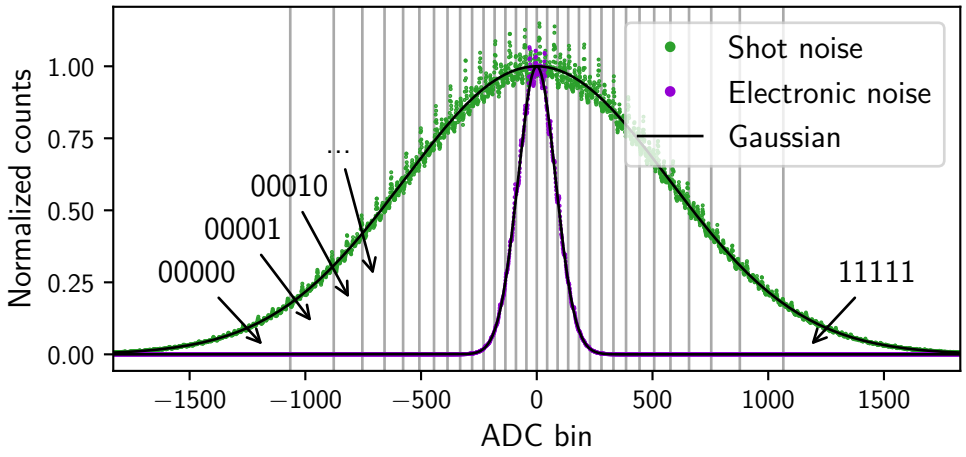

Figure 4.3: Histogram of the shot noise measured with improved laser power compared to the detector's electronic noise. The dotted lines represent the Gaussian distribution with the respective data set's standard deviation. The data sets were normalized to the maximum value of the Gaussian. Vertical gray lines mark the 32 bin edges used to extract $n = 5$ bits per sample and the bit value associated with each bin.

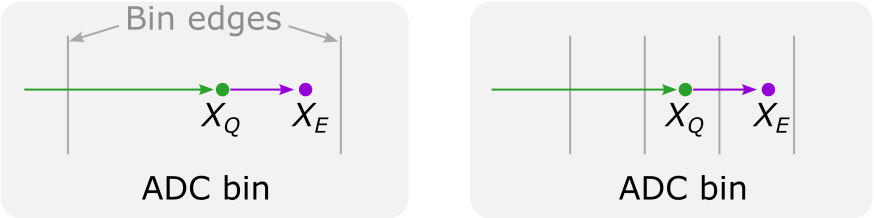

Figure 4.4: Left: Bin width is larger than σ_E. Given that the quantum noise assumes a value X_Q, the probability that the value X_E the electronic noise assumes changes the bin that the measurement value X_M falls into is small. It follows that it contributes little to the overall entropy. Right: Bin width smaller than σ_E. The probability that the electronic noise changes the bin is high, thus it has high contribution to the overall entropy.

the sum of two random variables $X_M = X_Q + X_E$, with X_Q the quantum noise and X_E the electronic noise. When the width of the smallest bins is close to the standard deviation of the electronic noise σ_E, the value that X_E assumes decides into which bin the measurement value falls. The Shannon entropy gained by further dividing the bin then stems only from electronic noise and would be considered classical. This is shown graphically in Fig. 4.4.

If we want to make another division of bins to add another bit of quantum information, the ratio between quantum and electronic noise has to be increased by a factor of 2 in amplitude (6 dB). For a homodyne detector it could be improved by increasing the LO power until just before the detector saturates. It could be further

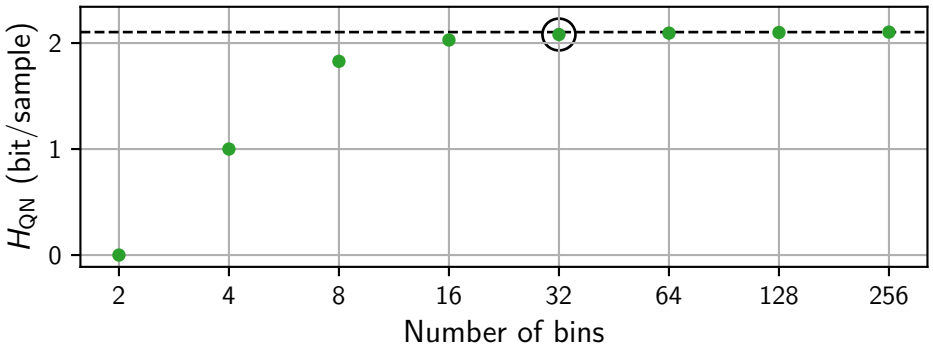

Figure 4.5: Quantum entropy proportion calculated by subtracting the entropy of electronic noise from the total entropy vs number of bins the histogram was divided into. At the highlighted point at 32 bins the extracted entropy only increases very little with additional number of bins.

increased by replacing the vacuum state in the signal port with another quantum state with higher variance, such as an anti-squeezed state.

In a first attempt during the unfinished bachelor's thesis we focused on improving the noise ratio by increasing the LO power. The original setup operated with 1064 nm light. To increase the maximum light power before the detector saturates, we decided to switch the laser wavelength to 1550 nm, following the same argument stated in section 3.1. At the new wavelength we were able to increase the LO power from 5 mW to 24 mW without observing saturation effects. To calculate the noise ratio and entropy content of each sample we acquired 32 Misample of both shot noise and electronic noise. Shown in Fig. 4.3 is the histogram of this measurement. Here the improved noise ratio is visible as the increased standard deviation of the corresponding Gaussian distributions. We achieved a noise ratio of 7 equivalent to 16.9 dB.

We generated n raw bits from each sample by dividing the total noise distribution into 2^n bins of equal sample content. To obtain the amount of entropy from quantum information we modeled the total entropy content of the shot noise measurement as the sum $H_{\text{tot}} = H_{\text{QN}} + H_{\text{EN}}$ of quantum and classical entropy. We estimated the quantum entropy proportion as the difference $H_{\text{QN}} = H_{\text{tot}} - H_{\text{EN}}$ when binning both distributions with the same bin edges. With the improved noise ratio, the quantum entropy content plateaus at $n = 2.1$ bit of quantum information content for 32 bins, which translates to an increase of more than a factor of two over the initial setup. For the data from Fig. 4.3 this is shown in Fig. 4.5. With this improvement the number generation rate could be increased from 41.6 Mbit s^{-1} to 83.3 Mbit s^{-1}. Due to time constraints we did not acquire a large random number sample to apply statistical tests. Since the other characteristics of the generator remained the same (for spectral distribution and autocorrelation see appendix A), it seems reasonable to assume that following the same post-processing steps as in the original setup would lead to an

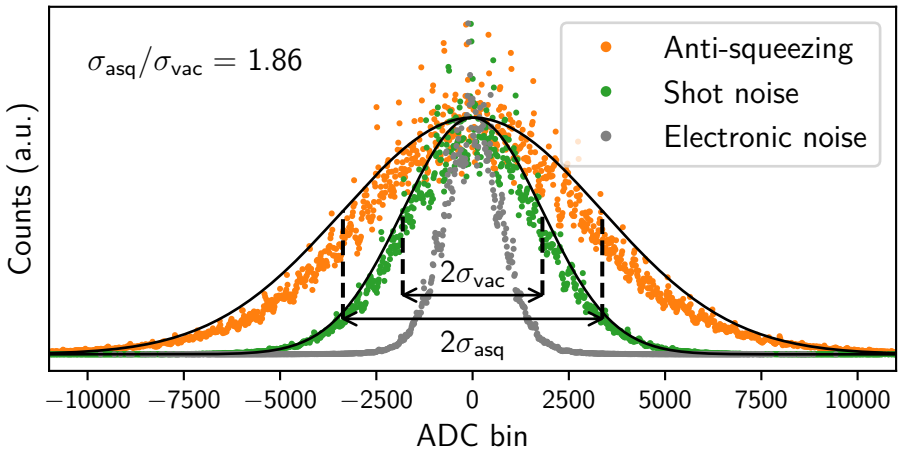

Figure 4.6: Histogram of anti-squeezing-enhanced noise compared to shot noise and electronic noise of the new detector design. Counts were arbitrarily scaled to match the Gaussian distribution with the data's standard deviation.

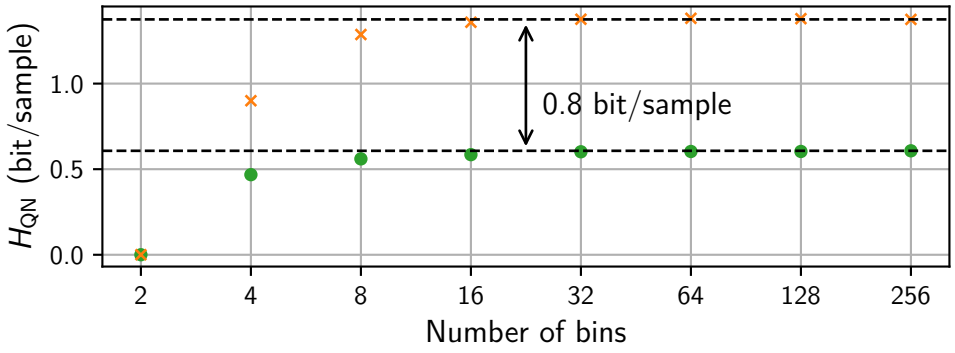

Figure 4.7: Extracted quantum entropy from shot noise (purple) and anti-squeezing-enhanced noise (orange) vs number of bins.

equally random output.

4.2 Anti-squeezing-enhanced QRNG

As part of the master's thesis of Sarah Nolte [Nol22] we explored a new approach to the previous QRNG design to further increase the noise ratio by replacing the vacuum state with an anti-squeezed state. Increases in quantum noise relative to shot noise greater than 20 dB have been achieved with a similar setup [Sch18], as well as by squeezing cavity 2 in this setup at a later time. Additionally, for this project we replaced the detector with the new homodyne detector design introduced in section 3.1 and the analog signal processing electronics of the previous setup with new ones matched to a new DAQ system.

QRNG version	Initial	Improved	Anti-squeezing
What was changed	—	higher LO power	different quantum state
Quantum entropy content n (bit)	1	2.1	+0.8
Generation rate (Mbit s^{-1})	41.6	83.3	120.6

Table 4.1: Performance comparison of the different QRNG versions. Quantum entropy content of the anti-squeezing improved generator is evaluated as an upgrade to the other generators entropy content.

Shown in Fig. 4.6 is the noise histogram with the comparison of shot noise and the variance added by the anti-squeezed state. At the time of the thesis we were limited by the output of squeezing cavity 1, which produced smaller (anti-)squeeze factors than cavity 2. The mean anti-squeeze factor over the frequency range of the measurement was 6.4 dB resulting in an increased standard deviation of 1.86 compared to only shot noise. This resulted in an increase of the entropy content shown in Fig. 4.7 by 0.8 bit/sample. The overall lower quantum entropy content compared to the previous section was due to an increased electronic noise floor from the new homodyne detector design and signal processing electronics. Adding the increased entropy content to the number generation rate of the generator presented in Ch. 4.1 would further increase its generation rate to 120.6 Mbit s^{-1}.

With an anti-squeezed variance of 20 dB, which we demonstrated for cavity 2 at a later time (see Fig. 3.12) the amount of quantum entropy extracted per sample could be increased by another 2 bit compared to the results presented here. This would be an equivalent increase in noise power to increasing the LO power by a factor of $2^6 = 64$ which would certainly saturate the detector. It can however be realized at the same time as maximizing the LO power. Thus, this is a valuable approach that can be implemented with any balanced-homodyne-detector-based generator.

4.3 Conclusion and outlook

Especially for this type of QKD setup, which already includes a balanced homodyne detector and squeezed light source, realizing a balanced homodyne based QRNG design is highly practical, although anti-squeezed states are only already available at Alice's station. With the increased quantum noise power the anti-squeezed state provided, we demonstrated that the random number generation rate of the initial design could have been further improved to 120.6 Mbit s^{-1} with the limited anti-squeezing provided by squeezing cavity 1 or potentially even further to more than 200 Mbit s^{-1} considering the higher anti-squeezing factor cavity 2 could achieve.

This approach to improve the noise ratio is promising and should be explored further in the future with a higher anti-squeeze factor. With a faster DAQ system and

matched electronics that increase the bandwidth of the noise source, reaching random number rates upwards of $1\,\mathrm{Gbit\,s^{-1}}$ with this setup and approach seems feasible. By implementing anti-squeezed states in other setups, e.g. [Sym11; Zhe19; Geh21], improving their rates beyond $10\,\mathrm{Gbit\,s^{-1}}$ seems possible.

Chapter 5

Generation of high bandwidth CV entangled states

Since its appearance in the first theories of quantum mechanics, the concept of entanglement has been heavily discussed for applications in various branches of physics. It has found applications in metrology and as an important resource in the field of quantum information. In particular in QKD it facilitates device independence for increased security of protocols, i.e. making it possible to formulate a protocol without having to impose any assumptions that devices work in a certain way [Ací06; Zha22].

Similar to the repetition rate in DV systems, the bandwidth of a CV entangled state determines the speed at which quantum information tasks can be performed. In addition to applications in quantum computing, high bandwidth of entangled states is relevant in QKD where it impacts the secret key rate.

In general, the key rate is given by the product of information per channel use multiplied and the channel bandwidth, i.e. the rate at which the channel can be used. The information per channel use decreases with increasing channel loss and thus with increasing transmission distance. Increasing the bandwidth gives a secondary way to increase the key rate.

In the following I will present the development of a high bandwidth source of CV entangled states consisting of the two previously shown squeezed light sources to produce a two-mode squeezed state. Sources of two-mode squeezed states have previously been realized with correlations of 11.1 dB below the combined shot noise in Ref. [Zha21] and 10.9 dB below the combined shot noise in Ref. [Ebe13], each measured at 5 MHz and 8 MHz sideband frequency respectively. While the correlations for these sources drop towards higher sideband frequencies, another source that produced significant correlations up to 1.2 GHz has been reported in [Ast16]. I followed a similar approach to generation and detection up to high sideband frequencies.

As an addition to the two squeezing cavities setup in the previous chapter, optimal performance of the entanglement source required stabilization of the relative phase between the two squeezed states. I will present the implementation of this control loop in Ch. 5.1 and characterize the entanglement source's output in Ch. 5.2.

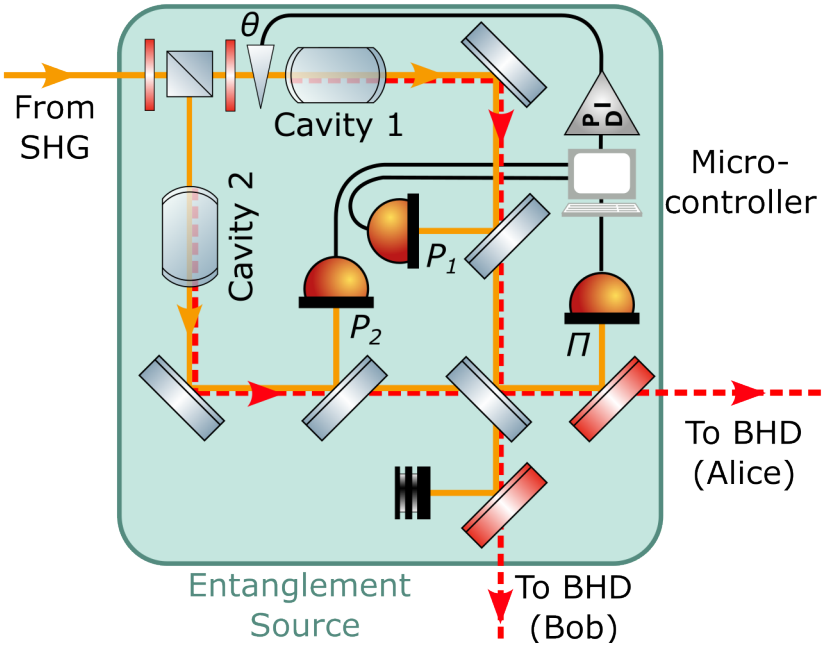

Figure 5.1: Schematic view of the entanglement source including the entanglement phase lock. Pump light and squeezed light from both cavities combined at the entanglement beam splitter in the bottom right.

5.1 Entanglement phase lock

The EPR-Reid criterion for a two-mode squeezed state is optimal when the entanglement phase, i.e the phase difference between the input squeezed modes, is 90°. Experimentally this phase can potentially drift as a result of optical length changes in the paths before combination on the beam splitter, for example due to air turbulence or changes in one of the squeezing cavities' length. The expected phase changes from these sources occur slowly in the frequency range between 0.1 and 10 Hz. For long term measurements it was necessary and for everyday work useful to implement a control loop that stabilized this phase.

The main difficulty in stabilizing the entanglement phase was sensing it without constantly performing full state tomography (e.g. by sweeping the readout phase). To circumvent this problem I implemented a control scheme based on the harmonic pump light transmitted through both cavities, which utilized sensing of the differential pump light phase. An overview of the setup is shown in Fig. 5.1. A part of each cavity's pump beam was transmitted through the cavity and overlapped on the entanglement beam splitter, forming a Mach-Zehnder interferometer and allowing sensing of the phase between the two beams. Since in the PDC process, fundamental and harmonic (pump) light have a fixed phase relation, the pump interferometer output gave an indirect way to monitor the entanglement phase.

To preserve the phase between pump and squeezed fields, both beams needed to experience the same phase fluctuations outside of the PDC cavity, so the two beams from each squeezing cavity needed to co-propagate until interfering on the entanglement beam splitter. Only afterwards could the pump and squeezed field be separated via a dichroic mirror and one of the outputs of the entanglement beam splitter be monitored with a photo diode.

Multiple factors complicated the generation of an error signal from the pump interferometer output. The interferometer input powers P_1, P_2 were unbalanced, the entanglement beam splitter was unbalanced for the pump wavelength $R_{775\,\mathrm{nm}} = 15\,\%$, and the transmitted pump power from one squeezing cavity tended to drift over time. As a result, obtaining a usable error signal required monitoring the interferometer input powers in addition to its output and performing calculations in real time. I will briefly review the theory of how these factors affect the interferometer output signal in Ch. 5.1.1 and present the calculation for generating the error signal in Ch. 5.1.2.

5.1.1 Interference at an unbalanced beam splitter

Let us briefly consider the beam splitter's outputs, which are analogous to the calculation for the balanced homodyne detector from Ch. 2.3.1 with a generalized beam splitter matrix $\tau = \begin{pmatrix} \sqrt{R} & \sqrt{T} \\ \sqrt{T} & -\sqrt{R} \end{pmatrix}$. Using that $R = 1 - T$ we can write down the signal of a photo diode in one output, which is proportional to the photon number

$$\Pi = \langle \hat{c}^\dagger \hat{c} \rangle_\psi = \langle \psi | (1-T)\hat{a}^\dagger \hat{a} + T\hat{b}^\dagger \hat{b} + \sqrt{T(1-T)}(\hat{a}^\dagger \hat{b} + \hat{b}^\dagger \hat{a}) | \psi \rangle \,. \tag{5.1}$$

Assuming both input states to be coherent states $|\psi\rangle = |\alpha\rangle \otimes |\beta\rangle$ and writing their amplitudes in polar form $\alpha = |\alpha| e^{-i\theta_\alpha}, \beta = |\beta| e^{i\theta_\beta}$ we obtain

$$\begin{aligned} \langle \hat{c}^\dagger \hat{c} \rangle_\psi &= (1-T)|\alpha|^2 + T|\beta|^2 + \sqrt{T(1-T)}|\alpha||\beta| \cos\theta & (5.2) \\ &= (1-T)P_1 + TP_2 + \sqrt{T(1-T)P_1 P_2} \cos\theta & (5.3) \end{aligned}$$

where $|\alpha|^2 = P_1, |\beta|^2 = P_2$ and $\theta = \theta_\alpha - \theta_\beta$. The interference signal is a sinusoidal with power-dependent amplitude and offset. For a control loop that only stabilizes Π to a constant value, a change in one of the input powers would result in a shift of the interferometer phase θ.

5.1.2 Generating a power-fluctuation compensated error signal

To compensate for input power changes I calculated an error signal digitally on an *Arduino due* microcontroller. To do so I empirically fitted the behavior of the three signals. I measured one interferometer output Π while ramping its phase, then

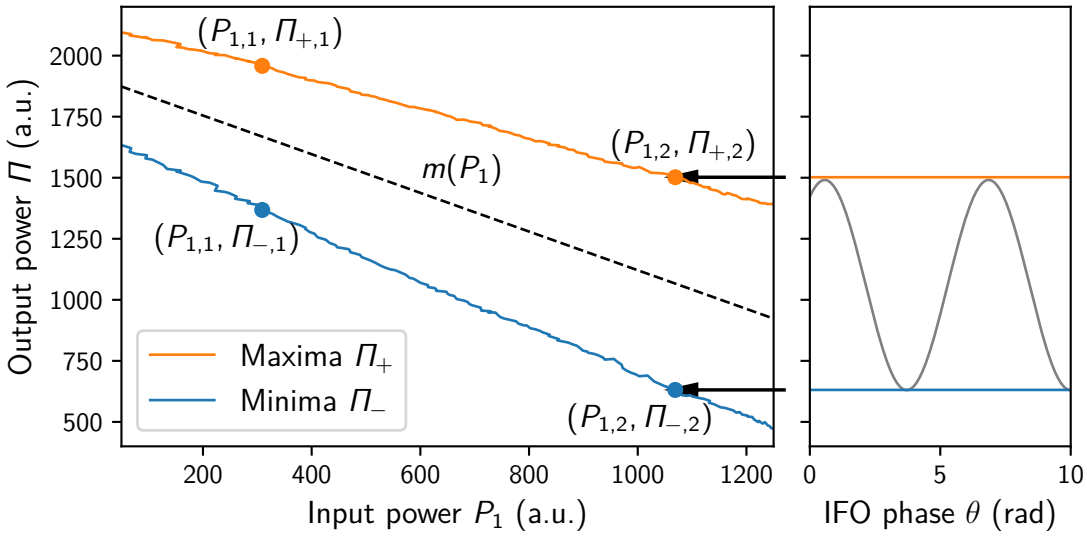

Figure 5.2: Plot of the pump beam interferometer output acquired by the microcontroller. Left: Input power dependence of the extreme values. The plotted points are the minima and maxima of the interference pattern, the dashed line is the power dependent mean value $m(P_1)$. Input and output power contain arbitrary offsets due to the particular electronic and optical setup used. Right: Interference pattern when ramping the interferometer phase θ at a given input power P_1.

slowly changed one of the input powers (P_1) while keeping the other constant and recorded the extreme values of the interference pattern $\Pi_\pm$ and how they changed with input power, shown in Fig. 5.2. For sufficiently high P_1 I observed that the power dependence of the extreme values became linear and I approximated them with a linear function. I modeled the interference signal

$$\Pi(P_1) = g(P_1)\cos(\theta) - m(P_1) \tag{5.4}$$

as a sum of a power dependent mean value $m(P_1) = a_1 P_1 + b_1$ and a power dependent interference term $g(P_1) = a_2 P_1 + b_2$, with free parameters a_1, a_2, b_1, b_2. To determine the parameters I performed a calibration measurement at two different input powers to obtain the two triplets $(P_{1,i}, \Pi_{\pm,i})_{i=1,2}$, then calculated them as

$$a_1 = \frac{(\Pi_{+,1} + \Pi_{-,1}) - (\Pi_{+,2} + \Pi_{-,2})}{2(P_{1,1} - P_{1,2})}, \tag{5.5}$$

$$b_1 = \frac{\Pi_{+,1} + \Pi_{-,1}}{2} - a_1 P_{1,1}, \tag{5.6}$$

$$a_2 = \frac{(\Pi_{+,1} - \Pi_{+,2}) - (a_1 P_1 - a_1 P_2)}{P_{1,1} - P_{1,2}}, \tag{5.7}$$

$$b_2 = \Pi_{+,1} - a_2 P_{1,1}, \tag{5.8}$$

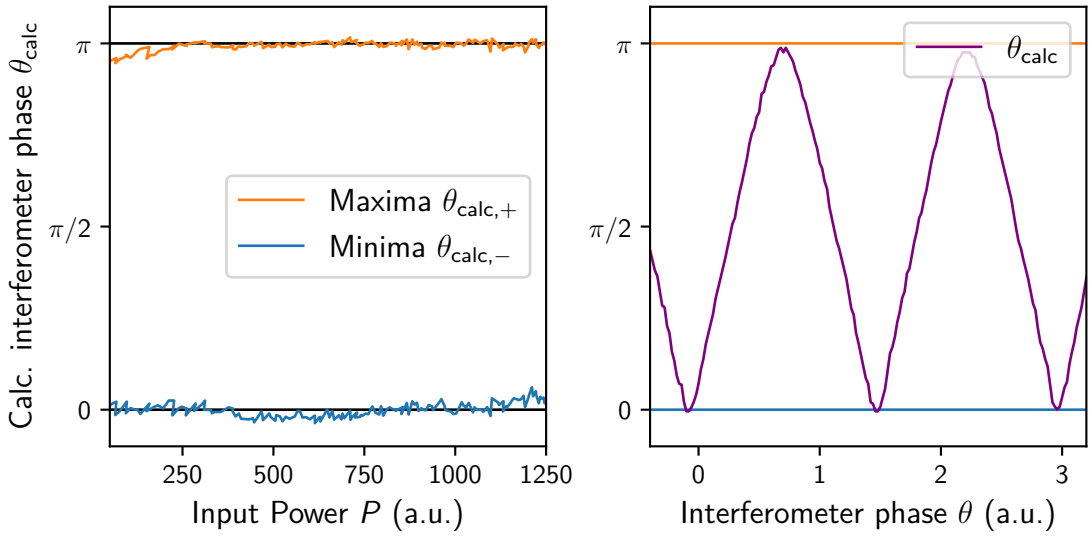

Figure 5.3: Measurement of the calculated interferometer phase. Left: Data of the extreme values as a function of interferometer input power. The calculated cosine amplitude is mostly power independent, with the remaining noise being digitization noise. Right: Calculated interferometer phase that was reconstructed while linearly scanning the interferometer phase θ at a set input power.

where $\Pi_{\pm}$ denote the extreme values of the interference signal where $\cos(\theta) = \pm 1$. Solving Eq. 5.4 for θ allowed to calculate the phase of the interferometer as

$$\theta_{\text{calc}} = \cos^{-1}\left(\frac{\Pi + m}{g}\right), \tag{5.9}$$

which is limited to the domain of the arc cosine between 0 and π, which is different from the interferometer phase θ, which is bounded by 0 and 2π.

The microcontroller performed this calculation and generated a signal which was then sent to an analog proportional-integral-derivative (PID) controller. I automated the calibration procedure digitally and performed it every time before engaging the phase lock. The calculated phase θ_{calc} for a measurement of a linear scan of θ, shown in Fig. 5.3, showed good agreement with the input signal even when changing the transmitted power of one squeezing cavity P_1.

To find the right locking point I first adjusted the anti-squeezing produced at 45 MHz sideband frequency from both squeezing cavities to be the same, then scanned the readout phase of one homodyne detector while tuning the entanglement phase. By scanning the readout phase while monitoring the homodyne output I could obtain the full $\hat{X}, \hat{Y}$ phase space picture, which should be rotationally symmetric. If I observed a modulation on the homodyne signal, either the entanglement phase or the anti-squeeze factor was not well-adjusted. It could be corrected by first changing the entanglement

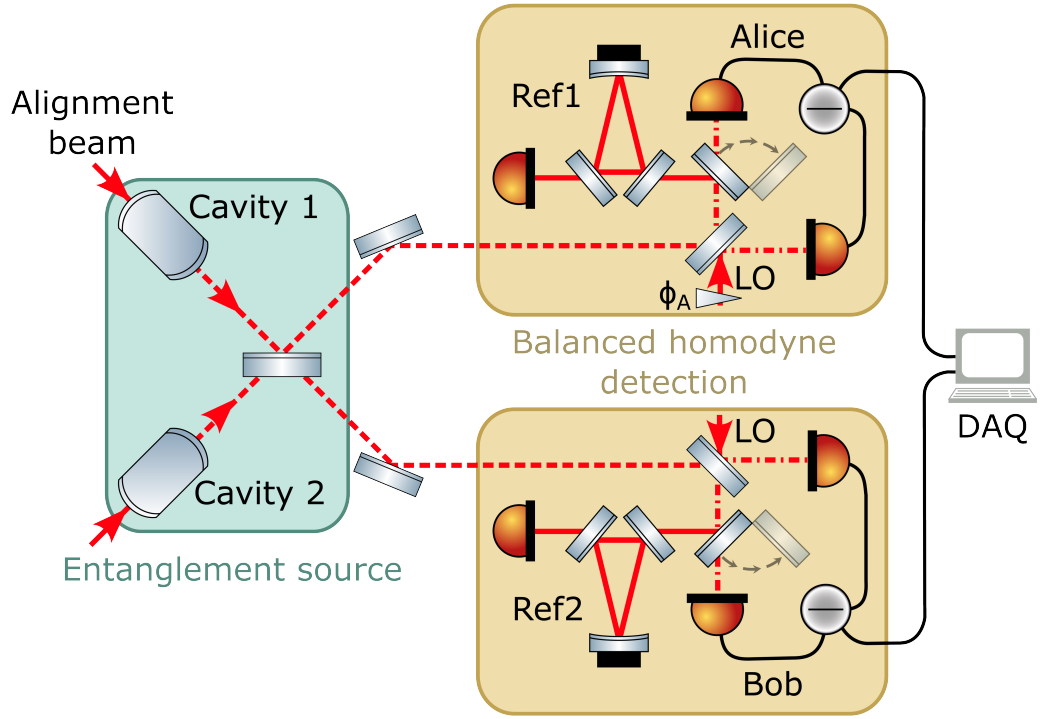

Figure 5.4: Setup for aligning the mode overlap of both squeezing cavities (with flip mirrors) and for the correlation measurement (without). Both detector's signals were captured with a high speed DAQ card. Only Alice's readout phase ϕ_A was tunable.

phase such that the modulation was minimal, then adjust one cavity's pump power until the modulation vanished.

Once the control loop was at the locking point it was able to keep the entanglement phase at the set value over tens of minutes. It was able to compensate for the squeezing cavity's resonance point drifting slightly, which would cause the transmitted harmonic power to change as well. I observed no modulation in the signal of a single homodyne detector over this time period. When an asymmetry while scanning the readout phase appeared, it also coincided with changes in the anti-squeezing levels due to a change in performance of one squeezing cavity.

5.2 Local measurement of high bandwidth entanglement

To characterize the entanglement source I used the setup shown in Fig. 5.4. The two output beams of the entanglement source were each sent onto a balanced homodyne detector located in the same laboratory. To achieve good mode overlap between the squeezed beams, two cavities served as a reference similar to the setup for a single squeezing cavity. The reference cavities were reached via flip mirror in the optical

path before one photo diode of each homodyne detector. Matching both squeezing cavities to a single reference ensured good overlap of the two squeezed modes on the entanglement beam splitter, and between the entangled mode and the LO on the homodyne detector. The second reference cavity was only necessary to ensure mode overlap of the second detector's LO and the entangled mode. Each of the four alignments to the reference cavities (cavity 1 to Ref1, cavity 2 to Ref1, cavity 1 to Ref2, cavity 2 to Ref2) was better than 98 %. For alignment, I used a 1550 nm adjustment beam coupled through the highly reflective side of each squeezing cavity, which was turned off during operation. For operation, I then tuned the squeezed light sources close to resonance one after the other and tuned their squeeze factors as described before in the phase lock section.

To observe correlations and anti-correlations without a control loop to stabilize either Alice's or Bob's readout phases ϕ_A or ϕ_B, I continuously scanned ϕ_A while leaving ϕ_B to potentially drift. The signals of both Alice's and Bob's detector, $\hat{X}_A$ and $\hat{X}_B$ were sampled simultaneously by a two-channel DAQ card *(Teledyne ADQ32-PCIe)* with 2.5 GHz sampling rate for 2.5×10^8 data points. I then blocked the signal port of both detectors and acquired the same number of samples of shot noise for each detector. I analyzed this data set first in the time domain, then in the frequency domain. I will present both investigations in the following.

5.2.1 Time domain analysis

Since the readout phase of one detector was continuously changing over time, I expected the sum and difference of Alice's and Bob's signals to oscillate between correlations and anti-correlations. To observe this oscillation I first filtered the signal and shot noise traces of both detectors with a digital 20001 tap finite impulse response (FIR) band-pass filter at 45 MHz center frequency and $\pm$5 MHz bandwidth. I then normalized each detector's signal to the mean of its filtered shot noise, calculated the sum and difference and corrected them by a factor 2 for the shot noise variance of two detectors. A subset of this data is displayed in Fig. 5.5.

The correction by a factor of 2 allowed a comparison between the single detector signals $\mathrm{Var}(\hat{X}_A(\phi))$ and $\mathrm{Var}(\hat{X}_B)$ and the sum and difference signals. This is equivalent to a normalization to the combined shot noise of the two detectors and produces a picture similar to a typical squeezing measurement, i.e. producing symmetric squeezed and anti-squeezed variances around the shot noise in a lossless measurement.

From Fig. 5.5, we can see that the variances of one detector $\hat{X}_A(\phi_A)$ and $\hat{X}_B$ remain constant at 3 dB above shot noise while changing Alice's readout angle ϕ_A. The constant level confirms an equal anti-squeezing level of the two input states at this sideband frequency. From the sum and difference signal, we observe a variance of 4.2 dB below the combined shot noise at maximum correlation and 5.5 dB above the combined shot noise at maximum anti-correlation corresponding to the squeezed

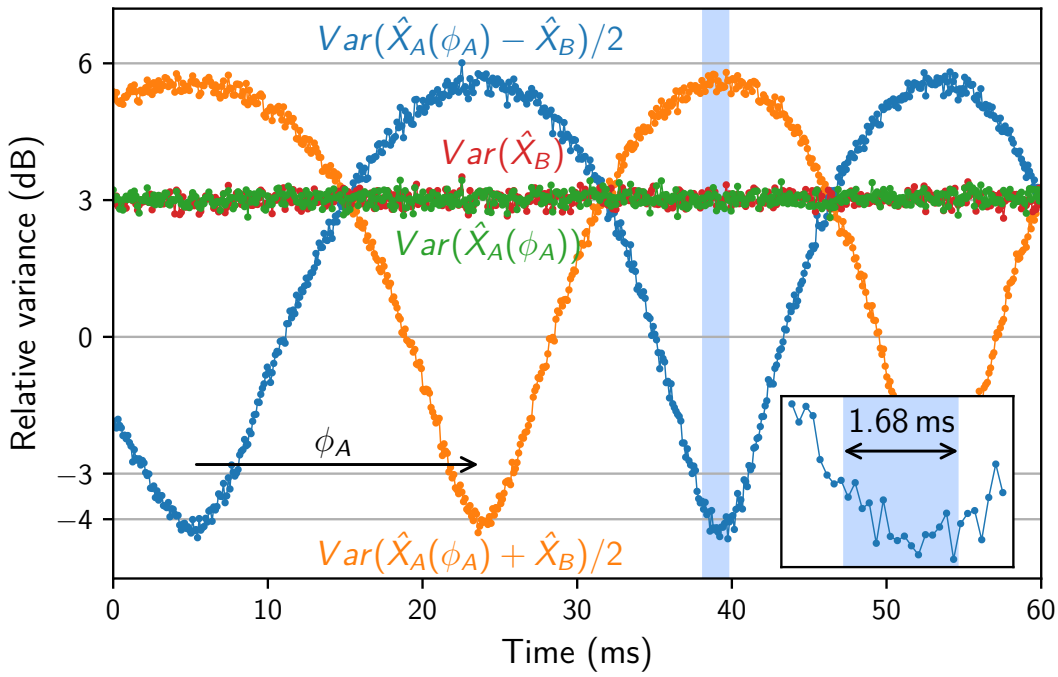

Figure 5.5: Variance of the two homodyne detector signals (green, red) relative to shot noise as well as their sum (blue) and difference (orange) while Alice's readout phase ϕ_A is scanned. The signals were first filtered with a digital (45 ± 5) MHz band-pass filter and normalized to each detector's shot noise level, then added and subtracted. The variance of sum and difference was then corrected by a factor 2. Each point represents the variance of a block of 262 144 measured data points. The data highlighted in blue was used to calculate the spectrum in Fig. 5.7.

and anti-squeezed variances of the input states. A value smaller than 0 dB indicates a possible violation of the Duan criterion, which would prove inseparability and thus entanglement of Alice's and Bob's states, while a value below −3 dB would indicate a possible violation of the EPR-Reid criterion.

Fig. 5.6 shows the same data as in Fig. 5.5 but filtered around (500 ± 100) MHz to show the low-noise frequency band. Two interesting features were visible. First, the extreme values of sum and difference signals had different height. This was caused by electronic noise that was common mode between the detector signals, which canceled out in the difference signal.

The more interesting feature was that the variance $\hat{X}_A$ of Alice's single detector showed a modulation that depends on Alice's readout phase. This indicates that the initial anti-squeezing values in this frequency band where not equal, equivalent to an elliptic phase space representation. It was caused by the different cavity linewidths and subsequently different squeezing bandwidths of squeezing cavities 1 and 2.

It is expected that the ellipticity of Alice's and Bob's state is the same. The fact

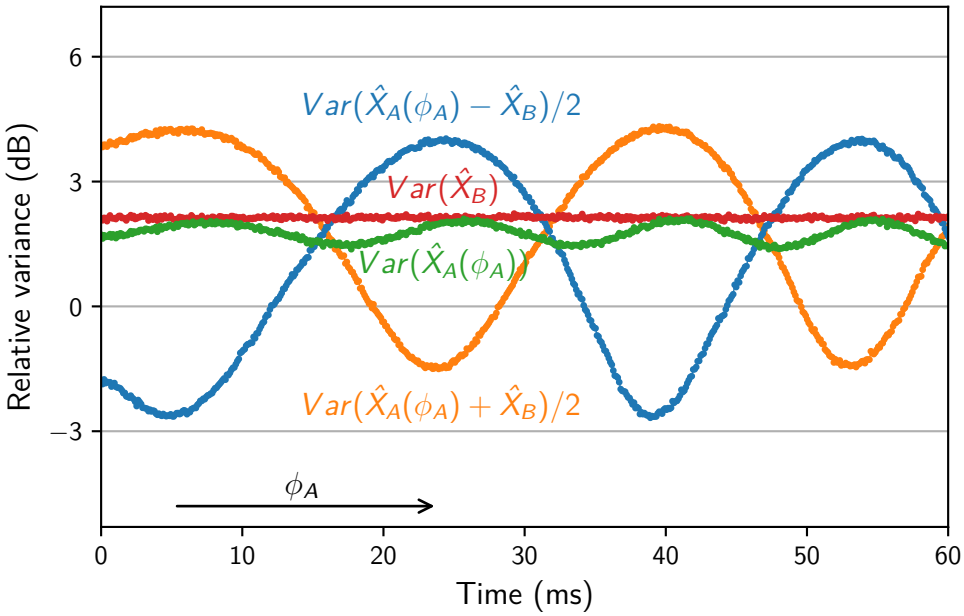

Figure 5.6: Variance of the two homodyne detector signals (green, red) as well as their sum (blue) and difference (orange) relative to shot noise, filtered with a FIR band-pass filter between 400 MHz and 600 MHz.

that no modulation was visible in Bob's signal indicates that his readout phase stayed constant over the measurement time.

The measurement presented here is insufficient to verify a violation of either the Duan or the EPR-Reid criterion in the strict sense. Both require measuring the two orthogonal quadrature pairs $(\hat{X}_A, \hat{X}_B)$. To obtain an accurate value for the other quadrature from a similar measurement, both Alice's and Bob's readout quadrature would need to be changed by 90°. Without a global phase reference or control loop, there was no way to change Bob's quadrature by precisely this amount. However, it is evident from theory and has been shown in previous experiments [Rei89; Ast16; Geh15] that the variances of the orthogonal quadrature pair should be the same for the two-mode squeezed states used here. Given that no asymmetry is visible in Alice's quadrature signal for low sideband frequencies, I therefore argue that it is reasonable to assume a similar variance for the other quadrature pair $(\hat{Y}_A, \hat{Y}_B)$ and thus conclude that these criteria were violated given a value below their respective limits.

For the higher frequency band this is not the case. In that band the observed correlations in the orthogonal quadrature would be smaller, however I argue that they should still be below 0 dB and thus exhibit inseparability. At the time of the measurements I was not aware of the ellipticity in the higher frequency band. It could have been exploited as a reference for both detector's readout phases, allowing for the measurement of both quadrature pairs $(\hat{X}_A, \hat{X}_B)$ and $(\hat{Y}_A, \hat{Y}_B)$ and thus verifying

the Duan and EPR-Reid criteria in the stricter sense.

5.2.2 Frequency domain analysis

From Fig. 5.5 I chose a subset of the data to analyze the relative variance by sideband frequency. As before each signal $\hat{X}_A$ and $\hat{X}_B$ needed to be normalized to their detector's shot noise levels $\hat{X}_{\mathrm{Vac},A}$ and $\hat{X}_{\mathrm{Vac},B}$ to account for possibly different electronic gains. The shot noise level of the detectors was frequency dependent, each with a different dependence, which can be seen in chapter 3.1. This meant that the shot noise normalization needed to be performed by frequency as well. Here I realized this by first calculating the fast Fourier transform (FFT) of Alice's and Bob's quadrature signals and shot noise from the highlighted 4×10^6 data points from Fig. 5.5 in blocks of 4096 points. I then estimated their power spectral density S_{xx} by first normalizing each signal to its frequency dependent shot noise, then adding or subtracting:

$$S_{xx} = \frac{1}{2}\left| E\left[\frac{\mathrm{FFT}(\hat{X}_A)}{\sqrt{\left| E\left[\mathrm{FFT}(\hat{X}_{\mathrm{Vac},A})\right]\right|^2}} \pm \frac{\mathrm{FFT}(\hat{X}_B)}{\sqrt{\left| E\left[\mathrm{FFT}(\hat{X}_{\mathrm{Vac},B})\right]\right|^2}} \right] \right|^2, \tag{5.10}$$

with $E\left[\mathrm{FFT}(\hat{X})\right]$ being the mean value of the FFTs over the 4096 data point blocks. The factor of $\frac{1}{2}$ denotes normalization to the sum of both detector's shot noise variances. The sampling frequency of 2.5 GHz limits the highest resolvable frequency to 1.25 GHz, and the choice of block size of 4096 points corresponds to a frequency resolution of 610 kHz. The spectra are shown in Fig. 5.7.

The curves derived from raw data (see the lighter colors) show that the sum and difference traces cross above 1 GHz. When comparing this to the homodyne detector's sensitivity curves from Fig. 3.1, the crossing occurs in the same frequency range that both detectors electronics show a self-induced oscillation. Such an electronic resonance likely lead to a delay of electronic signals at this frequency.

To compensate for this, I optimized the delay between Alice's and Bob's data set for each frequency in a range of 25 samples around the nominal zero-delay to minimize the variance of the difference curve. This yielded the solid blue and orange curves. This optimization only significantly affected the curves above 1 GHz which is in agreement with the explanation of a delay from a resonance at that frequency.

Notably this rules out optical effects as the cause for the crossing, such as readout phase noise or a frequency dependent rotation of the entangled state. In the case of phase noise one would expect that the correlations would be destroyed physically similar to how loss affects the two-mode squeezed state. Similarly, if the entangled state were to experience a frequency dependent rotation, the detectors would measure

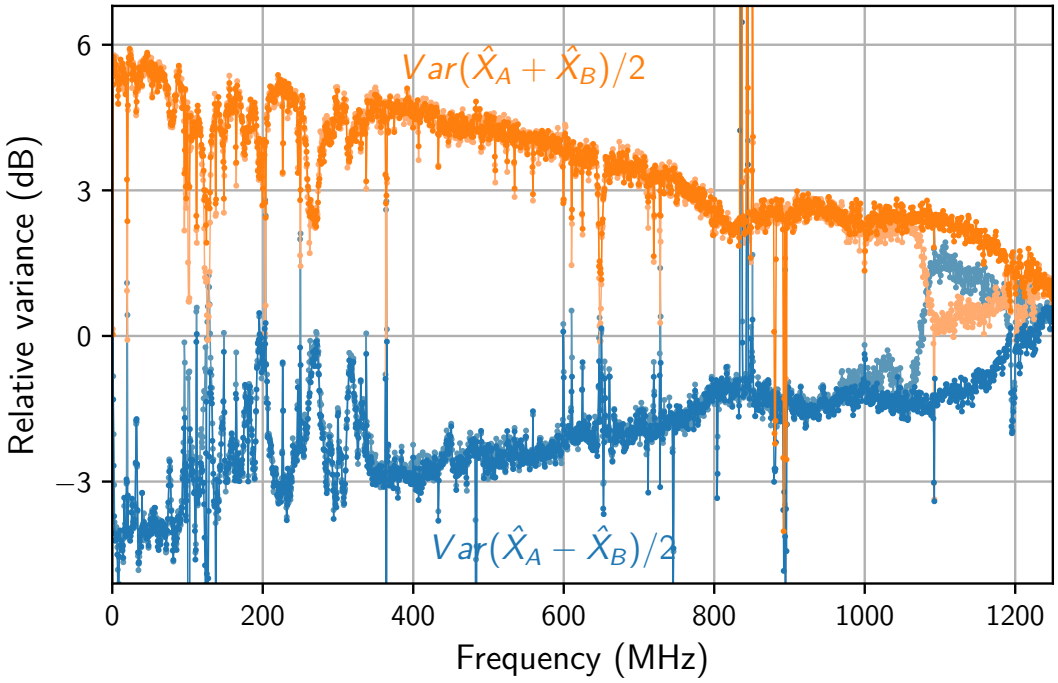

Figure 5.7: Variance of sum and difference of the homodyne detector signals as a function of sideband frequency. It was calculated from 4×10^6 data points from the highlighted region in Fig. 5.5. To obtain the curves shown in solid color I optimized the delay between the time series data at each frequency point for minimal variance of the difference signal. This optimization only significantly impacted the data above 1 GHz. The lighter curves show the uncorrected data.

different non-entangled quadratures, which would also lead to a loss of the correlations before acquiring the data. In both cases the optimal (anti-) squeezing levels would not be recoverable in post-processing.

After this correction the data showed a variance below the combined shot noise up to above 1 GHz. The low frequency part of the spectrum is dominated by electronic noise of the detectors between 100 and 350 MHz. A dark noise level for this measurement was not recorded. However, the peaks correlated well with those from the squeezing measurements from Fig. 3.12 and remote entanglement measurement from Fig. 5.7. Above 350 MHz the frequency band up to about 600 MHz is free of electronic noise peaks. Here it showed a variance of −2.8 dB to −2.2 dB relative to the combined shot noise level. With improved initial squeezing this gives a 250 MHz wide frequency band for generating raw samples for key generation at the same rate.

The symmetric dips in correlation and anti-correlation at 850 MHz and 1000 MHz, one each previously observed in a single squeezing source's spectrum in Fig. 3.12, were again present in this measurement.

I argue that from this measurement we can infer a violation of the Duan criterion

and thus inseparability up to 1 GHz sideband frequency and a violation of the EPR-Reid criterion for a smaller frequency band up to 100 MHz.

5.3 Summary

In this chapter I presented the setup of the entanglement source consisting of two monolithic squeezed light sources. The source demonstrated peak correlations of -4 dB below shot noise around 45 MHz in a local entanglement measurement, allowing us to infer a violation of the EPR-Reid criterion. In the frequency band between 350 and 600 MHz, which was free of noise peaks, it reached correlations of below -2.2 dB. The mostly uniform spectral distribution in this frequency band was promising for key generation. With an improved initial squeeze factor of squeezing cavity 1 to that of cavity 2 it would be possible to achieve the 3 dB level below the combined shot noise required by the EPR-Reid criterion in this low noise frequency band and thus greatly increasing the source's EPR-bandwidth.

While stronger correlations have been achieved from a 20 MHz bandwidth source in Ref. [Geh15], this source improves upon the low frequency performance of the previous GHz bandwidth entanglement source by 1 dB while retaining a similar if slightly improved response in the higher frequency range to the source from Ref. [Ast16]. Importantly for the following chapter, this improvement enables the use of this source for a one-sided device independent QKD protocol.

Chapter 6

CV entanglement distribution

In QKD there are three common approaches to transmitting a quantum state of light, either by sending the light through free-space in-atmosphere, through vacuum between satellites, or through optical fiber. In-atmosphere free-space transmission has two major problems in conjunction with a two-mode squeezed state: Turbulence in air distorts the entangled beam's spatial profile. For homodyne detection the signal beam needs to be overlapped with a phase reference. Distortions of the spatial profile reduce the mode overlap with the phase reference leading to reduced detection efficiency. Additionally, the air itself absorbs a significant part of the light depending on atmospheric conditions such as humidity and presence of aerosols. Communication with a channel loss of more than 25 dB [Urs07] has been achieved for a similar transmission distance in atmosphere between two ground stations and attenuation is typically expected to be greater than 15 dB depending on distance [Deq21]. In an inter satellite transmission scenario these factors are removed, though two satellite-to-ground transmissions through atmosphere are still required to connect two terrestrial stations. This way for any transmission length the distance that the quantum state needs to propagate through atmosphere can be reduced to two satellite-to-ground transmissions. The channel loss for inter-satellite communication is however also significant with reported values of 40 dB [Lia17] over 53 km.

For a protocol based on a two-mode squeezed state it is critical that any loss is minimized. A violation of the EPR-Reid inequality requires less than $3\,\mathrm{dB} \triangleq 50\,\%$ of total loss. Propagation through a single mode optical fiber is comparatively low loss and keeps the light in the fiber mode, which simplifies preserving the spatial mode profile. Therefore, it is the best option for transmitting the entangled state.

Phase fluctuations or phase noise can occur in an optical fiber due to several processes, which differ both in their frequency range and the mechanism that produces them. Here I want to discuss a selection of effects that were the most important for this experiment. The following overview is ordered with ascending frequency.

Thermal perturbations generate a phase shift via the thermo-optic coefficient of the material in the sub-hertz to hertz frequency range. Outside a laboratory setting the environment temperature typically changes slowly with the time of day. Despite its slow speed the phase change caused by temperature changes needs to be compensated

to achieve continuous operation as it causes tens of thousands of wavelengths shift in a 1 km long fiber per degree Celsius. This can be achieved by acting on a part of the fiber that is located in a laboratory via a controlled temperature change or via mechanical stress acting on the fiber. However, the actuators need to have a large dynamic range to compensate the environmental changes.

Acoustic noise can couple to the light transmitted through a fiber via its photo-elasticity. This property causes the fiber's refractive index to change when exposed to mechanical stress. Static stress sources, such as bending the fiber during deployment, generally lead to a static change. The major contribution to phase noise from this channel is thus acoustic waves as they cause a periodic refractive index change at their acoustic frequency. This noise channel is especially relevant as optical fiber cables are often deployed in acoustically noisy environments, through cellars next to machinery and below roadways. Typical acoustic sources produce noise roughly between 100 Hz and 100 kHz, including seismic sources the lower range extends into the sub-hertz range and overlaps with thermal perturbations. Due to the relatively low frequency, this noise can potentially be compensated by active phase stabilization for example via fiber-coupled electro-optic modulator (EOM) given a sufficiently fast error signal.

Guided acoustic wave Brillouin scattering (GAWBS) is a process that produces frequency changes in the hundreds-of-megahertz range and has been investigated in several experiments [She85; Tak20]. To understand this process it is useful to model the fiber as a long, narrow cylinder made of fused silica. The cylinder's thermally exited vibrational modes interact with the light by inducing density fluctuations that affect its phase and polarization. In the particle picture a phonon and a photon combine in a forward scattering process, producing a photon with increased energy and shifted frequency. The likelihood of the scattering process is scales with the light power.

In a gigahertz bandwidth measurement GAWBS contaminates a large part of the spectrum, so to distribute entanglement it needs to be avoided. Detecting a continuous variable state requires a phase reference at the detector. The most straightforward way to realize is by sending a bright beam in addition to the entangled state. Sending the bright phase reference beam along the same fiber, for example via polarization multiplexing, would not be a viable option as the phase reference would scatter into the entangled mode. In a recent experiment polarization multiplexing was used to transmit a weak pilot tone as a phase reference, which was then used to stabilize a laser at the remote station [Sul22]. They minimized scattering into the entangled mode by using low optical power for the pilot beam.

Transmitting the phase reference alongside the entangled state by frequency multiplexing could be an option, i.e. by shifting the light frequency by more than the width of the GAWBS spectrum (by a few GHz), however it would require high

frequency electronics that can be challenging to realize. Towards higher frequencies this approach is limited by stimulated Brillouin scattering which covers a band around 10 GHz [Tav20].

The solution we opted for was to send the phase reference through a separate second fiber deployed in proximity to the first. In this arrangement both fibers experienced almost the same thermal and acoustic perturbations, so that phase noise from these sources is mostly common mode and cancels out at the detector. Phase noise from GAWBS is only produced in the phase reference fiber and does not contribute in homodyne detection.

The quantum link used here consisted of two 1 km long *Corning SMF-28* low-loss single-mode optical fibers that we deployed connecting the Institut für Quantenphysik (IQP) and the Zentrum für optische Quantentechnologien (ZOQ), two separate buildings on the campus Bahrenfeld of the University of Hamburg connected by underground pipes. The total length of fiber deployed in noisy environment was approx. 100 m. Leaving the controlled laboratory environment introduced new thermal and acoustic noise sources and demonstrated a scenario closer to an applied setting.

6.1 Characterization of phase noise introduced by the optical fiber link

To test how well the assumptions above were fulfilled we characterized the phase noise introduced by fiber on a bright phase reference transmitted through optical fiber during the time of Sophie Verclas' master's thesis [Ver21]. The experimental setup shown in Fig. 6.1 consisted of a fiber Mach-Zehnder interferometer, the two arms of which consisted of the 1 km long fibers connecting the IQP and ZOQ. The two fibers were deployed in proximity to each other, so noise picked up from external sources would be common mode. We were specifically interested how well the slower thermal drifts and acoustic noise could be passively reduced by this approach and if noise from GAWBS would be sufficiently small for a weak signal beam.

6.1.1 Phase noise in a Mach-Zehnder interferometer

First let us have a look at how phase noise affects a Mach-Zehnder interferometer's output. Consider the balanced output beam splitter of the interferometer with two coherent states $|\alpha\rangle, |\beta\rangle$ as inputs. We can start with Eq. 2.70 from homodyne detection where the intensity I_c, I_d in the beam splitter's outputs is given by

$$I_c - I_d \sim \langle \hat{n}_\gamma - \hat{n}_\delta \rangle = \langle \hat{c}^\dagger \hat{c} - \hat{d}^\dagger \hat{d} \rangle = \langle \hat{a}^\dagger \hat{b} + \hat{b}^\dagger \hat{a} \rangle \,. \tag{6.1}$$

For the case of two coherent inputs this becomes

$$\langle \hat{n}_\gamma - \hat{n}_\delta \rangle = \alpha^\star \beta + \beta^\star \alpha. \tag{6.2}$$

We can now split both coherent state's amplitudes into a mean value and a noise term $\alpha \to (|\alpha| + |\delta\alpha|)e^{-i(\phi_\alpha + \delta\phi_\alpha)}$. The noise terms are split into an amplitude noise term $|\delta\alpha|$ and a phase noise term $\delta\phi_\alpha$. With this we obtain

$$\langle \hat{n}_\gamma - \hat{n}_\delta \rangle = 2(|\alpha||\beta| + |\alpha||\delta\beta| + |\beta||\delta\alpha| + |\delta\alpha||\delta\beta|)\cos(\phi + \delta\phi) \tag{6.3}$$

with $\phi = \phi_\beta - \phi_\alpha$ and $\delta\phi = \delta\phi_\beta - \delta\phi_\alpha$. Assuming that the noise terms are small compared to the mean ($|\delta\alpha| \ll |\alpha|$, $\delta\phi_\alpha \ll 1$ and the same for β) we can neglect the last term consisting only of the product of noise terms and approximate the cosine term as $\cos(\phi + \delta\phi) = \cos(\phi) - \delta\phi \sin(\phi)$. The difference signal then reads

$$\langle \hat{n}_\gamma - \hat{n}_\delta \rangle = 2(|\alpha||\beta| + |\alpha||\delta\beta| + |\beta||\delta\alpha|)(\cos(\phi) - \delta\phi \sin(\phi)). \tag{6.4}$$

This expression gives two terms that oscillate 90° out of phase to each other with respect to the phase ϕ. They can be interpreted as a phase and an amplitude quadrature and give a result reminiscent of that for homodyne detection from Eq. 2.72, especially in the case that one amplitude is zero. However, we can see that the result contains noise terms of both beams instead of only those of the signal beam. Phase noise terms $\delta\phi$ are only present in the sine term, so the optimal sensitivity to phase noise is reached at mid-fringe ($\phi = 90°$).

6.1.2 Excess noise measurements

We thus set up a Mach-Zehnder interferometer stabilized to mid-fringe to measure the excess noise introduced by the optical fibers. The experimental setup is shown in Fig. 6.1 consisting of the two previously mentioned 1 km long optical fibers in a fiber Mach-Zehnder interferometer configuration read out by two photo diodes.

We realized a control loop to stabilize the interferometer to mid-fringe for maximum sensitivity to phase fluctuations. It used the difference of the photo diodes signal as the error signal, which was fed back onto the phase of one interferometer arm via a piezo mounted mirror. The actuation range of the piezo spanned approx. 2 µm, equivalent to 1.3 interferometer fringes. A phase drift from a temperature change of 0.2 mK in a single 1 km long fiber would cause a phase shift than is larger than this actuation range. Due to the proximal deployment of the fibers making the phase drifts common mode, the control loop was able to compensate phase drifts for tens of seconds before running out of the piezo's range. If desired, the setup's phase shifting range could be extended by combining the piezo with a slower fiber-based phase shifter that uses either temperature or stress-induced refractive index change.

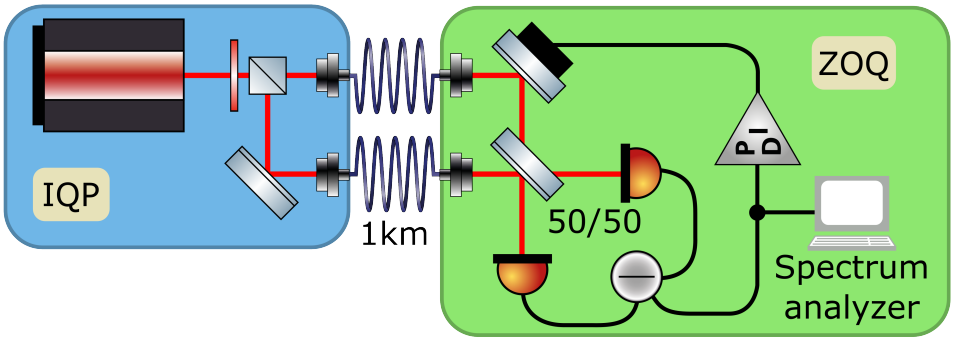

Figure 6.1: Fiber interferometer setup used to characterize the phase noise introduced by the fiber link.

The higher dynamic range of these devices spanning tens of fringes at a slower speed would complement the faster actuation achieved by the piezo.

The minimum noise contribution in this measurement is given by the shot noise of both input beams which is independent of the light power. When the light power of both interferometer arms is doubled, the shot noise contributions to $\delta\alpha$ and $\delta\beta$ will stay the same, while the amplitudes α and β increase by a factor $\sqrt{2}$. In a power spectral density measurement this would lead to a difference of 3 dB between two traces. We expected other noise sources to be power dependent to some degree, which would lead to a more than 3 dB increase. We can thus detect excess phase noise by changing both input powers in equal proportions.

We recorded the photo diodes difference signal with a spectrum analyzer while doubling the power in each interferometer arm between 0.35 and 2.8 mW, shown in Fig. 6.2, for frequencies above 5 MHz. Above 1 GHz the difference signal scales with 3 dB. From this we can conclude that the interferometer is shot noise limited in this frequency range. Below that frequency a comb of similarly spaced major noise peaks was visible, overlaid with a second comb with smaller width and amplitude. Similar spectra have previously been observed and attributed to GAWBS in [She85]. They offered a theoretical description stating that the major peaks can be described by modeling the fiber as a cylinder with a diameter a equal to the cladding diameter. The frequency Ω_m of the radial eigenmode R_{0m} of this cylinder corresponds to the frequency shift the transmitted light experiences due to GAWBS. In [She85] they calculated the frequencies as

$$\Omega_m = \frac{V_d y_m}{2\pi a}, \tag{6.5}$$

where y_m is the m-th zero of the function $(1-\alpha^2)J_0(y) - \alpha^2 J_2(y) = 0$, with $J_n(y)$ the n-th Bessel function of the first kind. Here $\alpha = V_s/V_d$ is the ratio of transversal and longitudinal speed of sound. To fit this to the data we assumed a value for the transversal speed of sound in fused silica of $V_s = 3790\,\mathrm{m\,s^{-1}}$ and the longitudinal

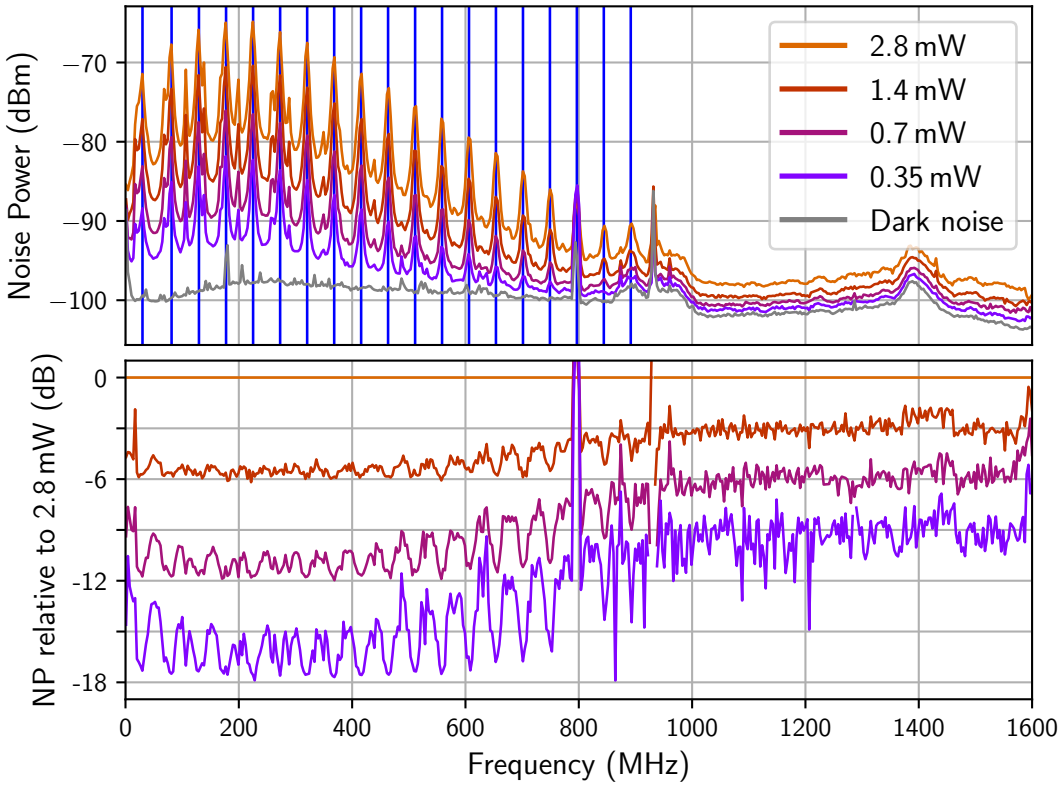

Figure 6.2: Photo current difference by frequency when doubling the Mach-Zehnder interferometer power. The vertical lines denote the position of the first 19 vibrational modes of a fused silica cylinder with 125.5 µm diameter. The given power values are the light power transmitted through each interferometer arm. The lower plot is normalized to the highest optical power. Acquired via spectrum analyzer, RBW = 300 kHz

speed of $V_d = 5970\,\mathrm{m\,s^{-1}}$. The vertical lines in Fig. 6.2 correspond to the first 19 radial vibrational modes. For $a_{\mathrm{optimal}} = 125.5\,\mu\mathrm{m}$ we observed optimal agreement with the measurement data. The nominal cladding diameter given by the manufacturer was $a = (125.0 \pm 0.7)\,\mu\mathrm{m}$, so the fitted value is in good agreement. In [She85] the more complex structure of smaller side peaks has also been modeled via the mixed torsional-radial modes TR_{2m}. However, the frequencies obtained from this calculation did not fit the peaks we observed.

Additionally, we observed that the noise amplitude decreased when reducing the light power. We theorized that the phase noise due to GAWBS vanishes when reducing the light power in the fiber by a sufficient factor, which should be the case for a two-mode squeezed state. In the scenario where we transmit a bright LO through one fiber and one part of the entangled state as a signal field through the other, phase noise from GAWBS should only be picked up by the LO. With the negligible

optical power of the two-mode squeezed state the requirement for the homodyne approximation for Eq. 2.72 is fulfilled. As a result the LO's phase noise does not contribute to the resulting measurement. Thus, the output signal only contains the quadrature variance of the signal field, unaffected by GAWBS.

We did not quantify the amount of residual phase noise in the hundreds-MHz band for low light powers. Instead, it was verified to be small from the remote entanglement measurement shown in figures 6.5 and 6.6. Most notably the evenly spaced phase noise peaks one would expect from GAWBS were not prominently visible in that measurement and thus the approach of transmitting the LO separate from the entanglement was effective.

6.2 Remote detection of entangled states distributed via fiber

Preparing for remote detection of the entangled states required some adjustment of the setup, shown in Fig. 6.3. Firstly, Bob's detection station needed to be moved to the remote laboratory. Secondly, for transmission of the entangled state to Bob's station it was important to ensure that the coupling efficiency of the state into the fiber was as high as possible. To achieve this I coupled light from an auxiliary laser located in the remote laboratory through the backside of the fiber, then matched this light to one of the squeezing cavities as a reference. As both squeezing cavities' outputs were matched onto the same reference cavity at Alice's homodyne detector (see Fig. 5.4) this produced a coupling efficiency close to 95 %.

While data acquisition in the local measurement was handled by a single two-channel DAQ card, remote detection required a separate DAQ card at Alice's and Bob's station. I used the same model DAQ card as before, which supported a higher sampling rate of 5 GHz in single channel mode. To ensure both stations perform a measurement on the same state in the same time basis both DAQ cards needed to be synchronized. The DAQ cards used were the same model as for the local measurement, which supported synchronization of their internal clocks by transmitting a slow 10 MHz signal. It was also convenient to distribute a trigger signal in addition to the clock to align the start of data acquisition. Both signals were provided to each station via two 70 m long coaxial cables deployed next to the optical fibers.

The channel length difference between cable and fiber introduced a constant delay between the data of each station. I compensated this constant delay of 40 µs in the following results by digitally shifting the data sets of each station. By searching for maximum correlation between the data sets while scanning the delay (shown in Fig. 6.4), I observed that the delay changed over the acquisition time by another 2000 sample/s due to misaligned clock frequencies of the DAQ cards, meaning the clock frequencies were different by 4×10^{-7}. It was unclear if this was due to

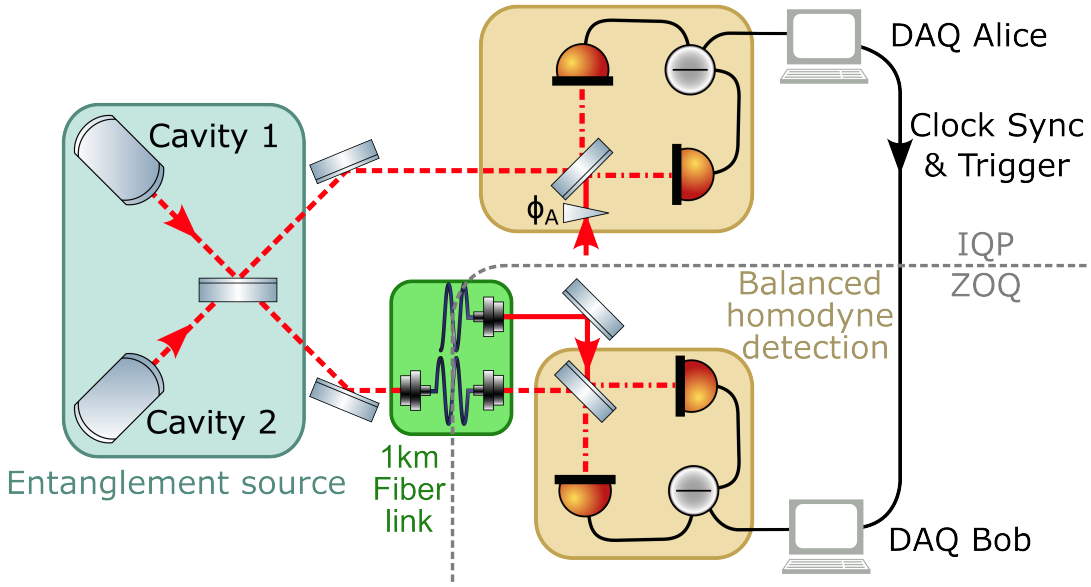

Figure 6.3: Setup for remote detection of the distributed two-mode squeezed state. Alice's and Bob's measurement stations were located in different buildings connected by two 1 km long optical fibers (for LO and entangled state) and two 70 m long coaxial cables (for DAQ clock synchronization and trigger signal).

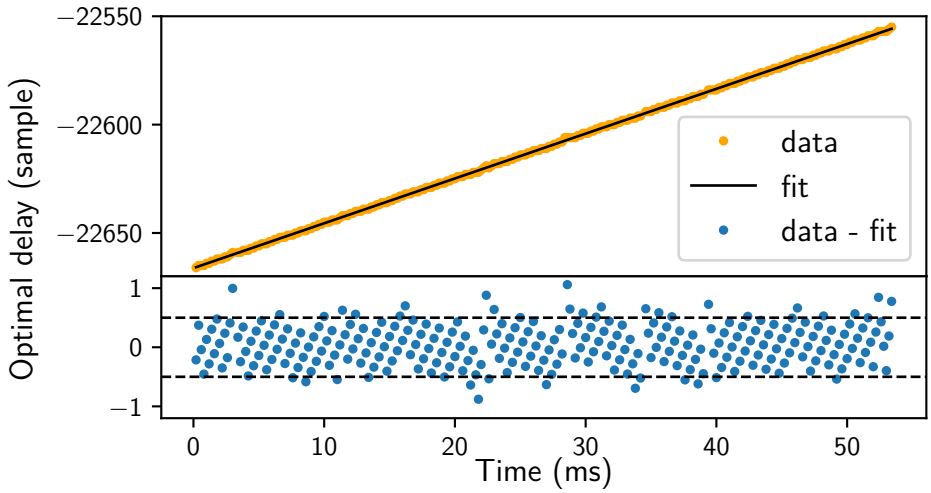

Figure 6.4: Delay between Alice's and Bob's homodyne signal at which the correlation was maximal, calculated as the maximum of the variance of sum and difference of 250 000 data points. I fitted the data with a linear function and shifted the data sets with respect to each other by this delay. The figure's lower part shows, that the deviation from the linear function is less than half of a sample (dashed lines) for most of the data set.

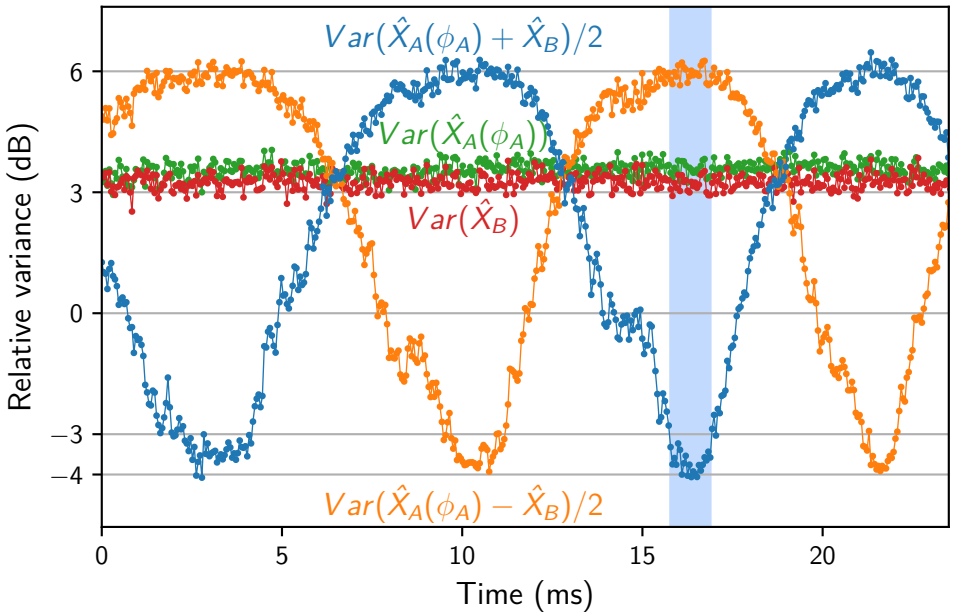

Figure 6.5: Variance relative to shot noise of Alice's (green) and Bob's (red) simultaneous quadrature measurements, as well as the noise power of the sum (orange) and difference signal (blue) filtered in the (45 ± 5) MHz band. Each point in this graphic represents the variance of 262 144 data points. The blue shaded area indicates the set of 6×10^6 samples from which the spectrum in Fig. 6.6 was calculated. A value below -3 dB indicates a possible violation of the EPR-Reid criterion.

improper setup of the DAQ cards or this was the accuracy of the DAQ system's clock synchronization function. I removed the delay in post-processing by modeling it as a linear function and shifted the data sets based on that. Delays of a fraction of a sample were rounded to the nearest sample.

For convenience in an application these signals could be transmitted via the optical fiber that carried the LO by frequency multiplexing. In another experiment [Haj23] a beam at 1310 nm was sent alongside a squeezed beam at 1550 nm and separated at the receiver station as a trigger signal for data acquisition. This would remove the requirement for additional cables while also removing the constant delay due to different channel lengths.

Shown in Fig. 6.5 are the variances of the quadrature signals recorded by Alice's and Bob's homodyne detectors, as well as of the sum and difference signals in the (45 ± 5) MHz band. During this measurement the readout phase of Alice's homodyne was scanned linearly. Bob's readout phase was not actively stabilized and experienced phase drifts.

After fiber transmission Alice's and Bob's signal showed correlations of between 3.5 dB and 4 dB below the combined shot noise of both detectors, indicating that a violation of the EPR-Reid criterion could possibly be shown in this frequency band.

The fact that this could still be observed indicated a low amount of additional loss induced by the fiber and gave a low bound on the amplitude of high frequency phase noise.

Compared to the local measurement presented in the previous chapter (Ch. 5.2), the remotely detected entangled states experienced loss from the transmission through the fiber link. This can be seen in the variance of Bob's signal when compared to Alice's. Assuming both were initially equal as seen in the local measurement, the variance of Bob's signal was reduced by 0.26 dB, which is equivalent to additional detection loss of 10.6 % caused by the fiber link.

The asymmetry of squeezed and anti-squeezed variance in the local and remote measurement at 45 MHz offered another way to estimate the loss. This yielded an additional detection loss between 9.7 % and 15.5 % depending on which maximum-minimum pair from Fig. 6.5 was considered, which in this case were the ones at 3 ms and 10 ms respectively.

For the sources of detection loss I considered the following contributions. Most of the loss was expected to originate from the fiber. The signal beam was coupled into and out of the fiber using a coupler with an AR coated ($R < 0.05\,\%$) aspherical lens. According to the manufacturer the performance of aspherical lenses as a collimator is imperfect, which would in this case manifests as light being lost when coupling into the fiber and after coupling out of it as lowered interference contrast at the homodyne detector. The lens quality was not specified, I assumed a loss value of 2 % per coupler. Each end face of the fiber was coated with an AR coating done in house, which was not characterized. I assumed a loss of 0.1 % at each surface. For propagation loss the manufacturer specified a value of $0.18\,\mathrm{dB\,km^{-1}} \triangleq 4\,\%\,\mathrm{km^{-1}}$ inside the fiber. Together with the coupling efficiency around 95 % these loss sources add up to a total expected additional detection loss of 12.8 % from transmission through the fiber link. This is in agreement with the range obtained from the measurements.

Assuming the loss figure per length from above we can estimate the distance limit at which correlations become insufficient to achieve one-sided device independence. We can solve Eq. 2.73 for η and assume the maximum value of correlations of 3.9 dB below combined shot noise as the initial squeezing value $\mathrm{Var}(\hat{X})_{\xi_{\mathrm{vac}}}$ and the 3 dB cutoff as $\mathrm{Var}(\hat{X})_{\xi_{\mathrm{vac},\eta}}$. We see that the limit is achieved when incurring an additional loss of 0.88 dB, equivalent to an additional 4.8 km of channel length. With the current loss factors, a one-sided device independent protocol would thus be limited to a maximum distance of 5.8 km.

In addition to classical loss, the transmission introduced phase noise with a frequency on the order of 1 kHz on Bob's readout phase, which was visible when comparing the shape of sum and difference signal to the local measurement. The linear scan of Alice's readout phase was interspersed with phase changes of small amplitude happening on a 1 ms timescale. The amount of high frequency phase noise

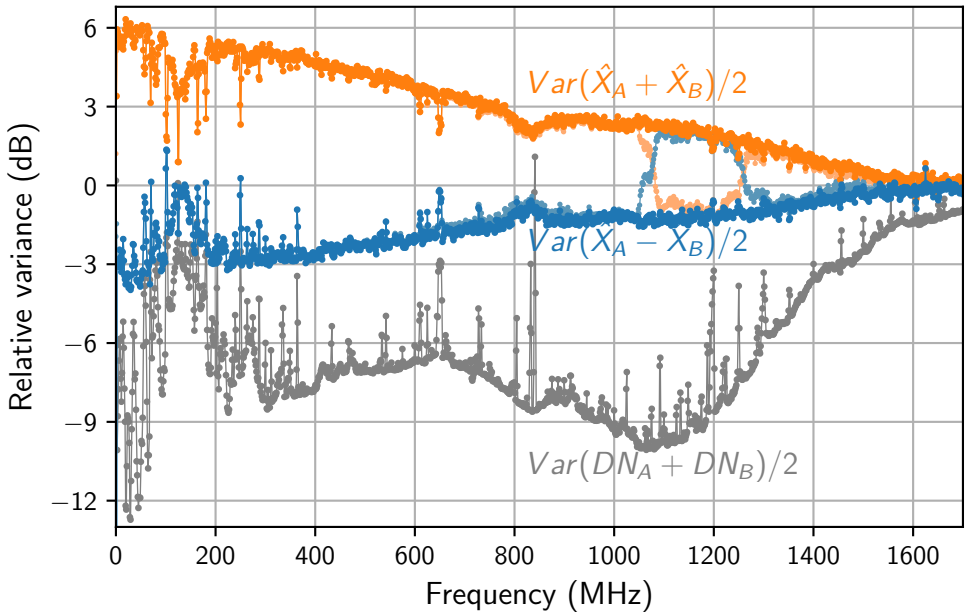

Figure 6.6: Variance of the distributed two-mode squeezed states by frequency relative to the shot noise calculated from a 1.2 ms long subset of data using FFT in blocks of 4096 points, see Eq. 5.10, with the delay between the detectors optimized for each FFT frequency. Lighter colors show the raw data. The variance of the sum of detector dark noises is shown in gray. The inset shows the low MHz part of the spectrum, where the relative variance was below −3 dB.

was small as the maximum correlation achieved compared to the local measurement was not significantly reduced.

To search for higher frequency phase noise I performed the same FFT-based frequency analysis method as previously described for the local measurement. This allowed me to calculate the power spectral density at maximum correlation shown in Fig. 6.6 from the highlighted 1.2 ms long subset of data. Compared to the local measurement, no additional high frequency noise sources were visible. Several of the narrow peaks from electronic noise that were visible previously were no longer present here. Of particular note was that the periodic structure of peaks one would expect from GAWBS was also not visible. Despite transmission through the optical fiber, the 270 MHz wide noise-free frequency band around 500 MHz from the local measurement remained intact. With a higher initial squeeze factor this would provide an ideal band for key generation. With the current setup the range around (45 ± 5) MHz showed potentially EPR-like correlations that allow for use in the one-sided device independent QKD protocol.

As the sampling rate for this measurement was 5 GHz, twice that of the local measurement, the maximum resolvable frequency was doubled. The extended range allowed to correlate the crossing of the two graphs between 1050 MHz and 1250 MHz

with an electronic resonance of the homodyne detectors in the same range. The resonance caused a phase shift in the electronic signals in this frequency range which changed correlation to anti-correlation. By performing the delay optimization between Alice's and Bob's signal at each frequency, the same as in the local measurement in Fig. 5.7, I was able to recover the (anti-) squeezing levels. In contrast, the symmetric dip around 120 MHz is unaffected by the optimized delay. Instead, here correlations were likely lost due to a high contribution of electronic noise from the two detectors.

6.2.1 Generating a raw key

With the previously presented experimental setup we can not generate a key in the stricter sense of the QKD protocol, as no way of obtaining full information of the quantum state was implemented yet. The (anti-) correlated data from Fig. 6.5 can still be used to illustrate the process and to estimate a raw key rate.

In the following I refer to a raw key as a bit string that is highly correlated between Alice and Bob, and refer to a corrected raw key as one that has been corrected for error and can be further post-processed and condensed in length to remove information that was leaked to an eavesdropper. In the following I present a simple approach to generate a raw key.

The basic concept for generating a key from the correlated data is identical to the process for the QRNG presented in Ch. 4.1. The two mode squeezed state in the homodyne detector's input locally behaves the same as a single mode anti-squeezed state that experienced 50 % of loss. The same signal- and post-processing steps as for the QRNG can be applied to a uniform frequency band from Fig. 6.6 by demodulating (mixing and low-pass filtering) and downsampling to remove correlations between samples. Given that Alice and Bob perform the same operations on their measurements, they each obtain Gaussian noise with a uniform frequency distribution that is correlated. They can then each perform binning to generate a raw key string from the Gaussian noise.

In contrast to signal-processing steps of the QRNG presented before, I performed the steps for this measurement entirely digitally. To obtain only the frequency band around (45 ± 5) MHz that showed EPR-like correlations I demodulated the data by multiplying with a 45 MHz sinusoidal signal, then applying a 20 001 tap FIR low-pass filter with 5 MHz bandwidth. Downsampling the data by a factor of 500 (sampling rate / bandwidth) removed correlations introduced by filtering, resulting in the mostly white noise spectra shown in Fig. 6.7.

Shown in Fig. 6.8 is a way to present the correlations that relates to the binning process. Shown there is the distribution of measurement outcomes of Bob $\hat{X}_B$ conditioned on Alice measuring an outcome $\hat{X}_A < \gamma$. In this picture correlation between the data sets is visible from the mean value of Bob's distribution being non-zero, meaning that Bob was likely to measure a value close to Alice's with some

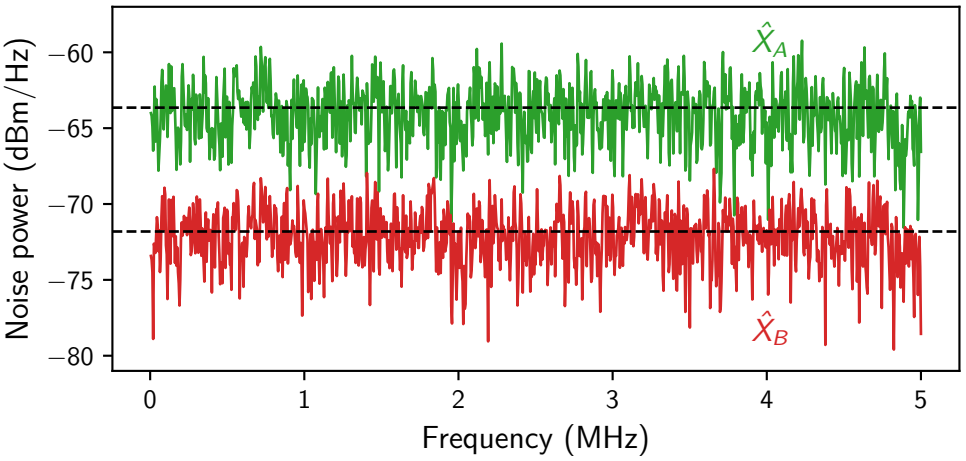

Figure 6.7: Power spectral density calculated from filtered and down sampled data of Alice's and Bob's homodyne detector signals $\hat{X}_A$ and $\hat{X}_B$. For visibility Bob's spectrum was moved lower by 8 dBm, both spectra have the same mean noise level.

residual uncertainty. When dividing both Alice's and Bob's distribution into bins, e.g. as shown in this case into 2 bins, values of Bob that get sorted into a bin different from Alice's (indicated by red area) cause a bit error in the raw key that needs to be corrected in the error correction step. The proportion of bit errors to total samples gave the bit error rate (BER).

The amount of bit errors can be reduced by discarding samples of Alice (and possibly Bob) that assumed values close to a bin edge. This however reduced the amount of samples that can be used to generate a key. Finding the optimum between cutoff distance and number of bins to use vs the bit error rate presents an optimization problem that has been considered in the case of other experiments [Geh15]. Due to time constraints and the limited correlation strength here I chose a simple approach: 2 bins for key generation and a simple optimization for the two cutoff distances γ_A and γ_B for Alice's and Bob's samples shown in Fig. 6.9. The data used for key generation also included the symmetrical subset $\hat{X}_B$ when $\hat{X}_A > -\gamma_A$.

For the data shown above I performed the binning for variable γ_A and γ_B and corrected the obtained raw key length by a factor for typical performance of error correction algorithms. Here I assumed an efficiency of $1.2H(p_{\mathrm{BER}})$, which has been reported for a low-density parity check algorithm [Dix14], where $H(X)$ is the binary entropy function and p_{BER} is the bit error rate of the raw key. Under these assumptions I obtained the optimal values $\gamma_A = -0.62, \gamma_B = -0.6$. With a bit error rate of 4.7 % this totaled a corrected raw key length of 18.2 kbit generated from the four minima of the relative noise power in Fig. 5.5 or a key rate of 336 kbit s^{-1}.

It should be noted that the raw key rate estimates given here are higher than the final key rate. Missing steps for a complete implementation of the QKD protocol

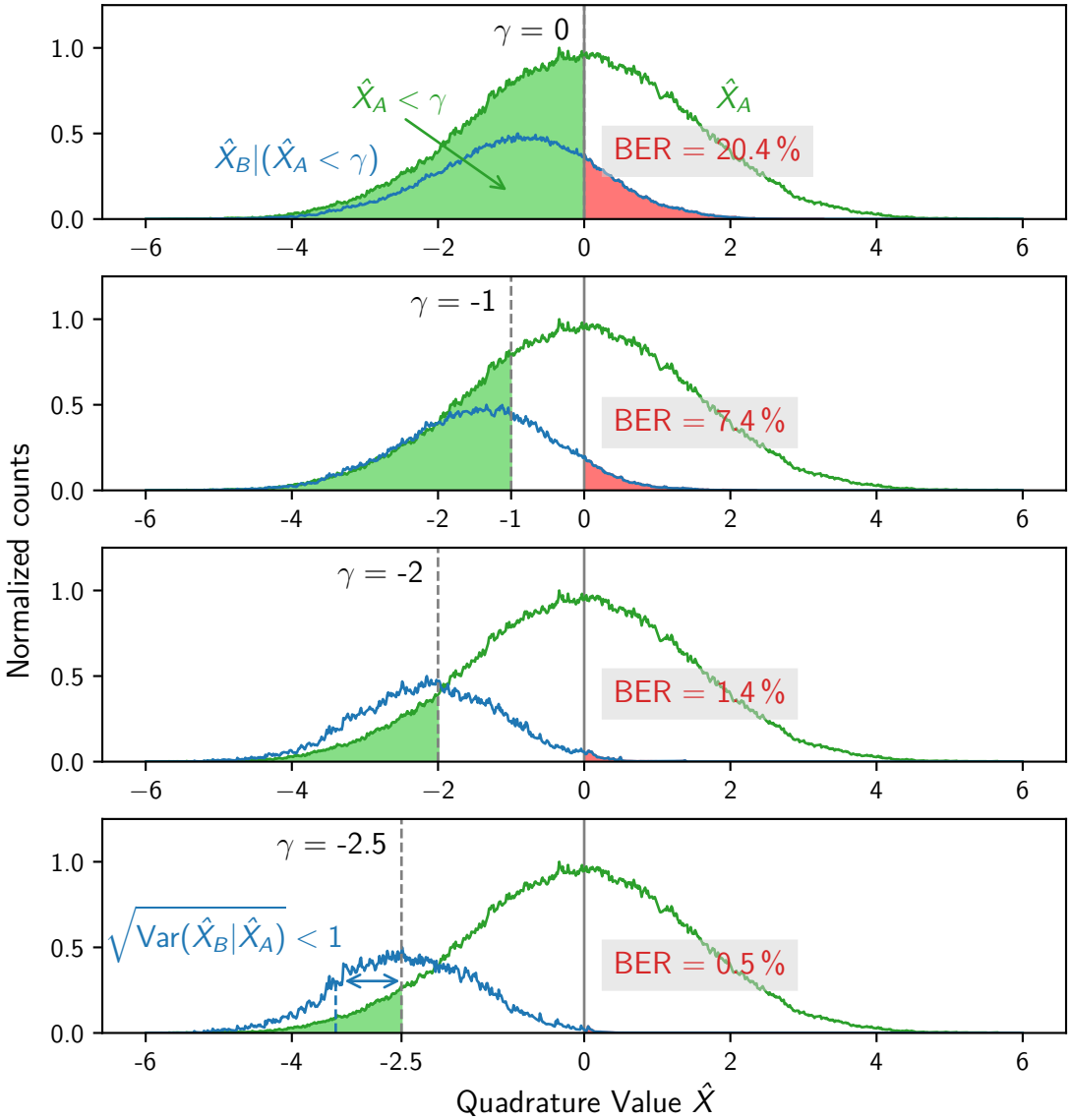

Figure 6.8: Histograms of Bob's data conditioned on Alice's measurement being smaller than the cutoff γ. Alice's full measurement data $\hat{X}_A$ is shown in green as a reference. Shown in blue is the subset of Bob's data $\hat{X}_B$ conditioned on Alice measuring a value $\hat{X}_A < \gamma$, which is indicated by the green area. The area highlighted in red corresponds to values of Bob falling into a bin different from Alice resulting in a bit error. The green histogram is normalized such that its maximum value is 1, the blue histogram such that it is 0.5.

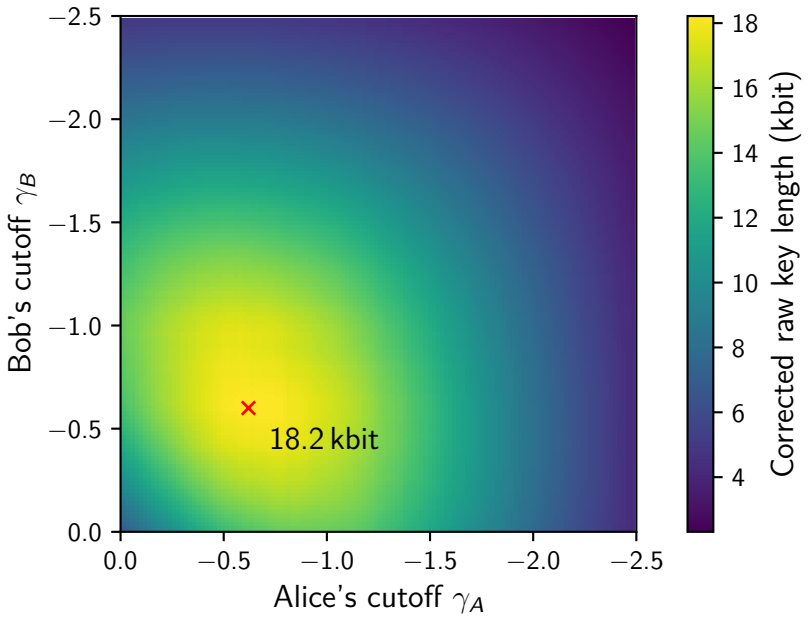

Figure 6.9: Corrected raw key length for different quadrature cutoff pairs of Alice and Bob, also taking into account the error correction efficiency of $1.2H(p_{\text{BER}})$. The cross marks the maximum key length.

are sifting and privacy amplification, as well as the parameter estimation on which the error correction efficiency greatly depends. In the sifting step 50 % of all samples would be discarded or used for parameter estimation, together with a small subset of the remaining samples. Depending on the amount of leaked information obtained in the parameter estimation step the key length is additionally reduced. For the similar setup implementing this protocol [Geh15] they analyzed these contributions for a higher initial squeeze factor and obtained a final key rate per bandwidth between 0.5 and 0.1 bit/sample depending on channel loss. For the entanglement achieved here I expect the final key rate per bandwidth to be lower than that. Assuming a value at the lower range of 0.1 bit/sample at a bandwidth of 10 MHz would yield a final key rate around 10 kbit s^{-1} under consideration of the wrong readout phase for 90 % of the measurement time.

Fig. 6.8 is directly related to quantum steering. Steering is equivalent to a violation of the EPR-Reid criterion and is present when the conditional variance $\text{Var}(\hat{X}_B|\hat{X}_A) < 1$ (read $\hat{X}_B$ given $\hat{X}_A$). This means that Alice can predict Bob's measurement outcome given her own, with a variance of less than the variance of the vacuum state. In this figure this can be observed for $\gamma \leq -2$.

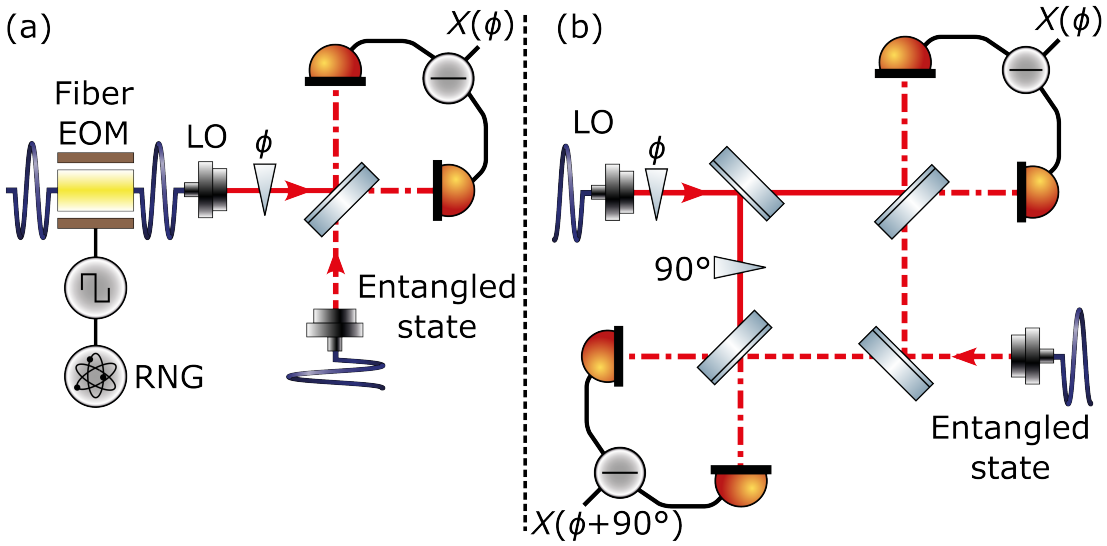

Figure 6.10: Setups to obtain full information about the quantum state: (a) Fast switching of the readout phase between the two orthogonal quadratures via fiber coupled EOM. (b) Q-function homodyne detector. This would replace the single homodyne detector at each measurement station.

6.2.2 Future improvements

For future implementation in a QKD scheme there are several things that need to be adjusted to utilize the high bandwidth of the entangled states. The QKD protocol discussed here requires that both Alice and Bob gather information on the full quantum state while the protocol is running. This could be achieved in two ways.

The first way that was originally suggested in Ref. [Fur12] for this protocol and which I considered throughout this thesis was to switch each detector's readout quadrature for each sample between $\hat{X}$ and $\hat{Y}$ at random. This would require a fast and accurate shift of the LO phase at each station by 90° at the same speed that samples are generated. Fast switching speeds of several hundred MHz could be realized with a fiber coupled EOM. Due to the high required speed, generating the signal required for driving the EOM might additionally require a custom implementation on a field programmable gate array.

A different way to monitor the full quantum state would be to change the detection scheme at one or both stations to a Q-function homodyne detector setup [Ral99] (there called heterodyne detection). For this the incoming state is split up equally and sent onto two homodyne detectors that respectively monitor the orthogonal quadratures $\hat{X}$ and $\hat{Y}$ simultaneously. Although this would require stabilizing the relative phase of the two detectors, it would be possible to obtain full state information without further use of complex electronics.

Either of these ways also requires the relative readout phase to be stabilized to

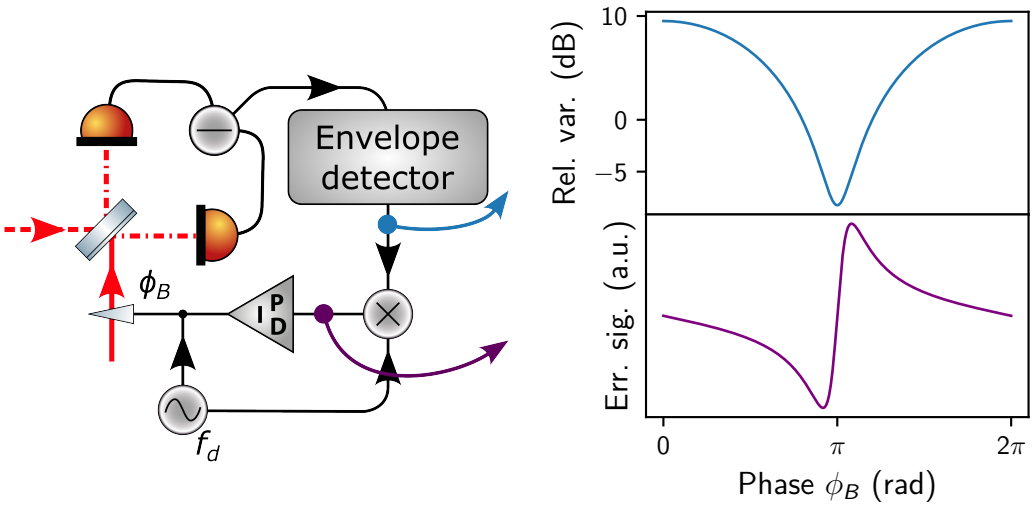

Figure 6.11: Schematic description of a dither lock for a squeezing measurement. From the squeezing measurement (blue) its derivative (purple) can be obtained by quickly dithering the readout phase, then demodulating the homodyne signal at the dither frequency.

work effectively. To achieve this at the remote station a proof of concept has recently been realized [Sul22] that transmitted a weak frequency shifted beam alongside a squeezed field through an optical fiber. Using the frequency shifted beam as a reference a separate laser at the receiver station was stabilized in both phase and frequency to the original laser source. That experiment did not require a secondary fiber to transmit a LO and instead generated it locally at the receiver station.

Another approach that is currently being implemented is a noise-based dither lock [Ver25], the basic concept is shown in Fig. 6.11. For the example of a squeezed state, it works by estimating the variance of the homodyne signal in a given frequency band while slightly changing (dithering) the readout phase ϕ_B at a lower frequency. Demodulating the signal at the dither frequency f_d yields the signal's derivative, which can then be used to stabilize the readout phase to a minimum (or maximum) of the variance of the squeezed state.

Applying this approach to the detection of entanglement requires a part of Alice's homodyne detector's signal to be sent to Bob's station via a public channel. By combining it with his own signal, Bob can recover a signal equivalent to the squeezing case, at which point he can realize the same variance estimation and dithering approach as for a squeezed state. Because the frequency band used for phase stabilization is sent to Bob via a classical channel, it has to be excluded from key generation.

Taking into account that the readout phase was not stabilized in the above measurement, the expected bandwidth could be increased further if the entire measurement was taken at maximum correlation. In the measurement from Fig. 6.5 the

readout phase was optimal for about 10 % of the samples. A stabilized readout phase would thus increase the corrected raw key rate by a factor of 10.

The currently usable bandwidth was limited greatly by the −3 dB bandwidth of the entanglement source. This was affected only slightly by loss from transmission through the fiber and instead limited by the squeeze factor of cavity 1. By improving it to performing at the same squeeze factor as what was demonstrated by cavity 2, the −3 dB bandwidth after fiber transmission could plausibly reach 600 MHz covering the noise-free frequency band. This would increase the sample generation bandwidth to 250 MHz and thus the raw key rate by another factor of 25.

6.3 Summary

In this chapter I presented the distribution of GHz bandwidth two-mode squeezed states and a LO as phase reference for the measurement via 1 km of optical fiber between two separate buildings on the Campus Bahrenfeld. Deploying the two fibers in proximity reduced low frequency phase drifts to a manageable level that could be compensated for tens of seconds, demonstrating the feasibility to implement a readout phase stabilization in the future. In spite of the added phase noise from leaving the controlled laboratory environment and low optical losses from coupling into the optical fiber, correlations with a peak value of −3.9 dB below shot noise were visible around 45 MHz sideband frequency, demonstrating that a violation of the EPR-Reid criterion in a 10 MHz band can be inferred. With the additional implementation of readout phase switching or another way to obtain full information of the quantum state, a one-sided device independent QKD protocol can be realized with this setup. With its current loss sources the setup could achieve the correlations required for a one-sided device independent protocol over a distance of up to 5.8 km.

As an estimate for an attainable key rate I generated a raw shared key pair from the time series data gathered from this measurement at 336 kbit s^{-1} taking into account the efficiency of common error correction algorithms. The final key rate of 10 kbit s^{-1} was computed as an estimate that included readout phase switching and further post-processing steps with an efficiency taken from a similar experiment.

With a stabilized readout phase which is currently being implemented, this estimate could be increased by a factor of 10. An improvement of the squeeze factor of cavity 1 to that of cavity 2 would further increase the −3 dB bandwidth of the entanglement source and thus greatly improve the key rate by another factor of 25. These improvements appear manageable and would push the corrected key rate to around 50 Mbit s^{-1} and the estimated final key rate to around 2.5 Mbit s^{-1} with one-sided device independent security.

Chapter 7

Conclusion and discussion

In this thesis I demonstrated the generation, distribution, and detection of a two-mode squeezed state with GHz bandwidth over 1 km optical fiber. The inferred violation of the EPR-Reid criterion in the presence of extra noise introduced by fiber transmission combined with the improved QRNG implementation pave the way for realizing a CV one-sided device independent (OsDI) QKD protocol in its entirety.

While this is the first demonstration towards a CV OsDI QKD protocol that leaves the laboratory environment, implementations of protocols from other categories (DV, device-independent) have been fully realized. Most implementations focused on achieving larger distances. Two useful points of comparison are: A CV QKD protocol that reached a similar key rate of $1\,\mathrm{Mbit\,s^{-1}}$ a longer distance of 25 km without OsDI security [Hua15]. While the protocol is less resilient, it gives a key rate benchmark for standard QKD protocols. A DV twin-field QKD protocol which achieved a measurement-device-independent key rate of $0.32\,\mathrm{bit\,s^{-1}}$ over 615 km and simulated a key rate of $5\,\mathrm{kbit\,s^{-1}}$ at their lowest distance of 250 km [Zho23].

In the context of these implementations the estimated performance of this protocol is best compared to the (DV) twin-field protocol. Over short distances the estimated key rate of the OsDI protocol is higher, however the twin field protocol does not share its strict upper distance limit of approx. 5 km. As such, its applications lie in building a quantum network between the buildings of a government campus or a data center, connecting e.g. the German government campus spanning 3.8 km or the White House and the Pentagon (separated by 3.4 km). The main wavelength of 1550 nm allows to integrate this protocol into existing fiber infrastructure. Additional advances in fiber technology that reduce transmission loss, or the successful implementation of a quantum repeater could extend the distance limit to cover a typical metropolitan area.

While development of large-scale quantum computers compromises the security of a large portion of currently implemented cryptosystems, QKD offers a way to achieve secure communication. The demonstration of a CV OsDI protocol's viability over a short distance provides an additional scenario that QKD can cover, adding to a list spanning from schemes between satellites, free space communication in-atmosphere, to long distance fiber optics. With this variety QKD can assure security and confidentiality once current encryption methods prove insufficient.

Appendix A

Additional QRNG characteristics

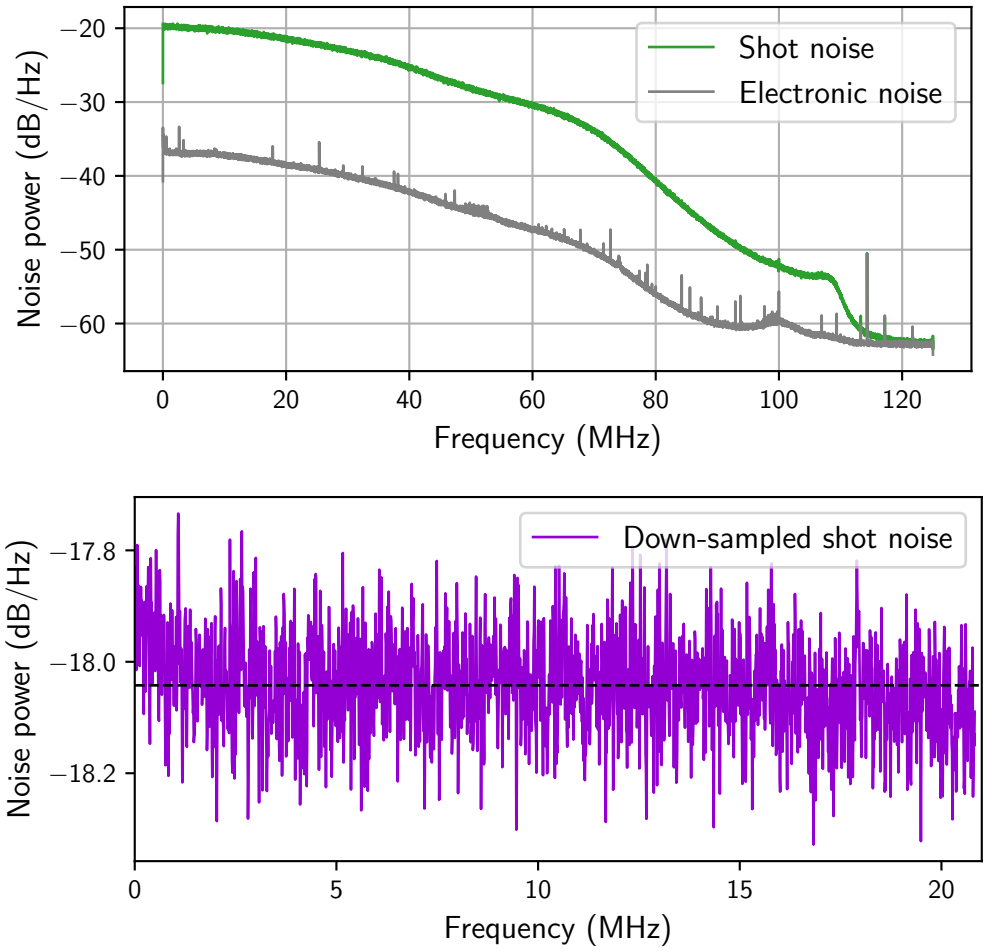

Figure A.1: Power spectral density calculated from shot noise data before and after lowering the sampling rate by a factor of 6 in post-processing for the initial QRNG design. After lowering the sampling rate the spectral distribution became close to uniform. A slightly raised low frequency contribution and slightly lowered high frequency contribution remained visible.

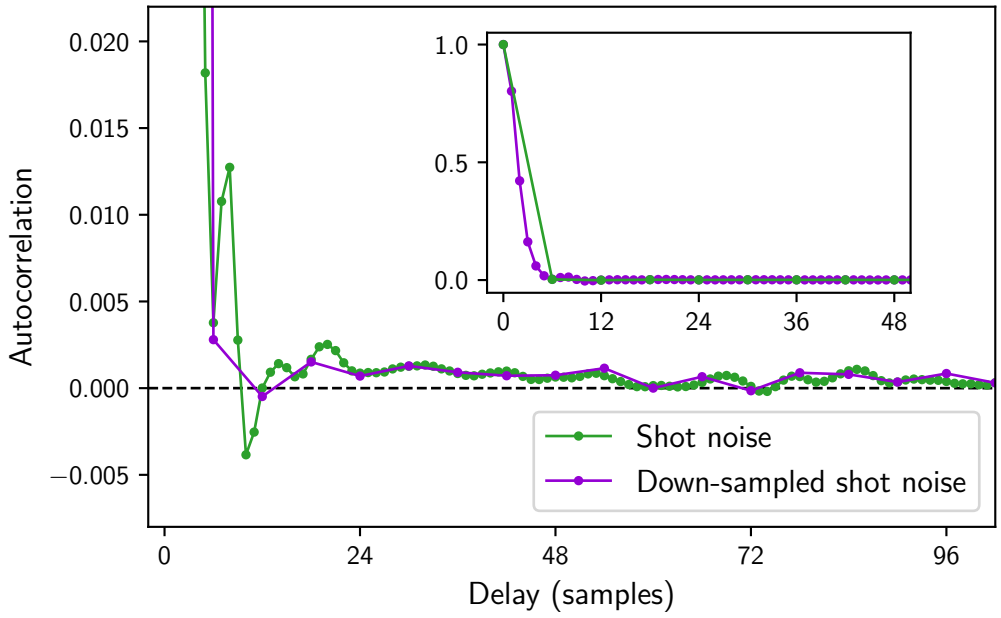

Figure A.2: Autocorrelation before and after lowering the sampling rate by a factor of 6. The inset shows a zoomed-out view of the first 50 delays.
The autocorrelation gives a measure, how similar a signal looks to itself when shifted by τ samples. A value of (-1 or) 1 means perfect (anti-) correlation. For a sinusoidal signal the autocorrelation function assumes these values after $n/2$ or n periods respectively. It also indicates how well data points with delay τ are independent of each other.
We intentionally limited the bandwidth of the shot noise signal by low-pass filtering. This caused correlation between successive samples. The filter type (Bessel filter) was chosen such that correlations vanish quickly for higher delays. This plot shows that for up to a 5 sample delay data points were significantly correlated, while for the 6th it was minimal, with the value 6 being given by the filter bandwidth. Ripples with an (in theory) periodic zero crossing every 6 samples were also visible, minimized by the choice of filter shape. By lowering the sampling rate the correlated samples are discarded, leaving a minimally correlated signal.

Appendix B

Raw key randomness characteristics

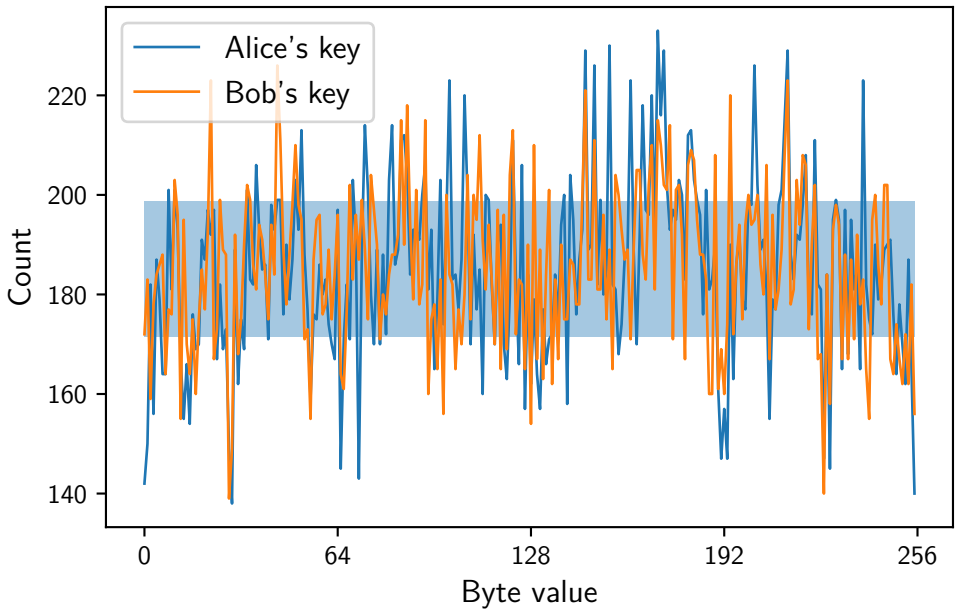

Figure B.1: Histogram of how often each byte value appears in the raw key from section 6.2.1. Shaded in blue is the 1σ area of a binomial distribution with probability $p = 1/256$ and the same sample size n as the data.
Although the sample size is very small, the histogram gives an indication of some regularity in the raw key. The byte values 0 and 255 (bit strings 00000000 and 11111111) appear less often in Alice's key by three standard deviations, indicating that long runs of the same bin were less likely than expected from a uniform distribution. This was likely due to the slight noise peaks from electronic noise visible in figure 6.7. While this is on the edge of being statistically significant, it is likely that it would become more clearly visible for a larger sample size.
These electronic noise peaks were not present in Bob's measurement and as a result the statistics of his key look more regular, although the sample size is far too small to be certain.

Appendix C

Homodyne detector circuit design

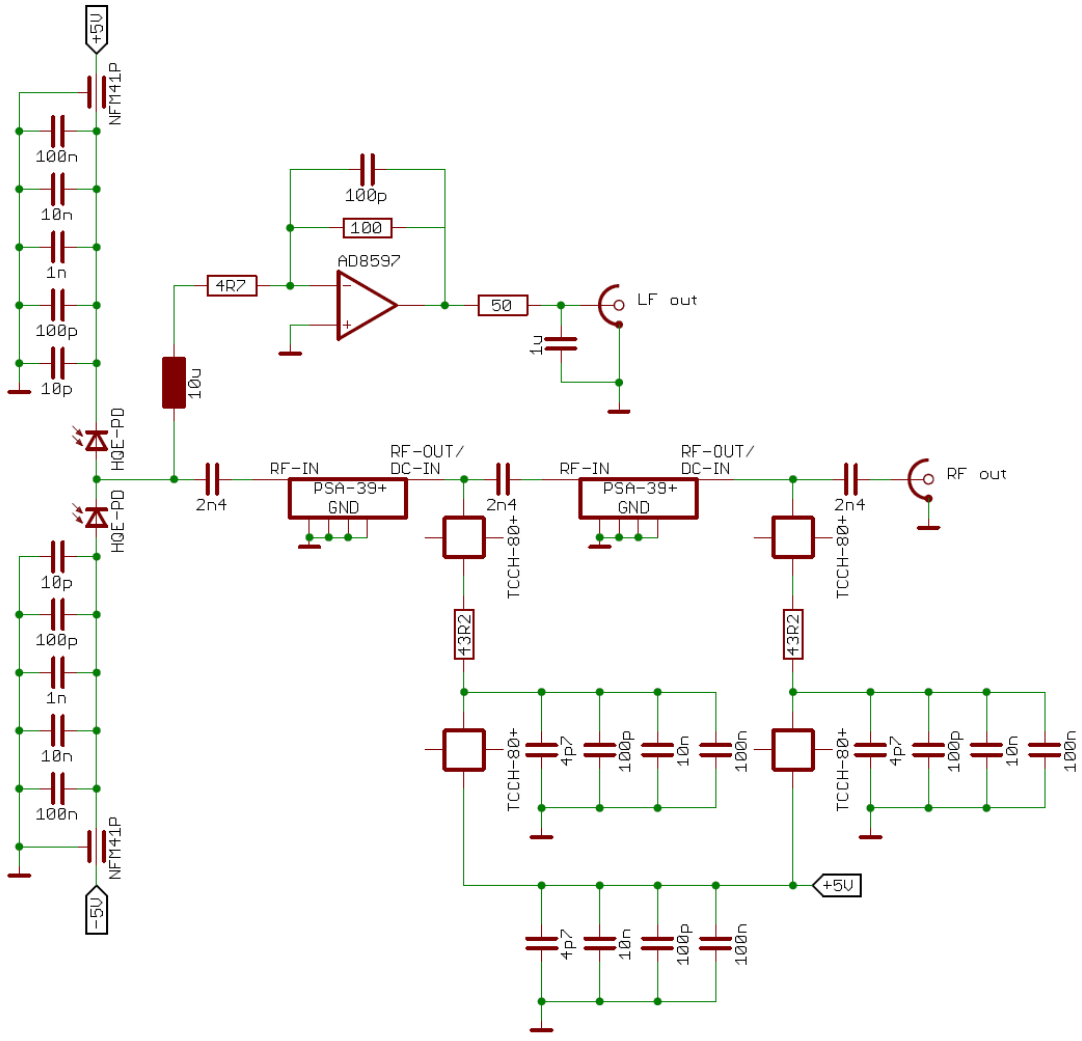

Figure C.1: Circuit design of the improved GHz bandwidth homodyne detector. The primary improvements in this design were the PSA-39+ radio frequency amplifiers providing gain over a high bandwidth, buffered supply and bias voltages, and multi layer PCB.

Bibliography

[Ací06] Antonio Acín, Nicolas Gisin, and Lluis Masanes. "From Bell's Theorem to Secure Quantum Key Distribution." In: *Phys. Rev. Lett.* 97 (12 Sept. 2006), p. 120405. DOI: 10.1103/PhysRevLett.97.120405.

[Aru19] Frank Arute et al. "Quantum supremacy using a programmable superconducting processor." In: *Nature* 574.7779 (Oct. 2019), pp. 505–510.

[Ast11] Stefan Ast et al. "High-efficiency frequency doubling of continuous-wave laser light." In: *Opt. Lett.* 36.17 (Sept. 2011), pp. 3467–3469. DOI: 10.1364/OL.36.003467.

[Ast13] Stefan Ast, Moritz Mehmet, and Roman Schnabel. "High-bandwidth squeezed light at 1550 nm from a compact monolithic PPKTP cavity." In: *Opt. Express* 21.11 (June 2013), pp. 13572–13579. DOI: 10.1364/OE.21.013572.

[Ast15] Stefan Ast. "New approaches in squeezed light generation." PhD thesis. 2015.

[Ast16] Stefan Ast et al. "Gaussian entanglement distribution with gigahertz bandwidth." In: *Opt. Lett.* 41.21 (Nov. 2016), pp. 5094–5097. DOI: 10.1364/OL.41.005094.

[Bac04] Hans Bachor and Timothy Cameron Ralph. *A guide to experiments in quantum optics*. English. 2nd. Vol. 1. Germany: Wiley-VCH Verlag GmbH, 2004. ISBN: 3527403930. DOI: 10.1002/9783527619238.

[Bau16] Christoph Baune. "Frequency up-conversion of nonclassical states of light." PhD thesis. 2016.

[Bel64] J. S. Bell. "On the Einstein Podolsky Rosen paradox." In: *Physics Physique Fizika* 1 (3 Nov. 1964), pp. 195–200. DOI: 10.1103/PhysicsPhysiqueFizika.1.195.

[Ben14] Charles H. Bennett and Gilles Brassard. "Quantum cryptography: Public key distribution and coin tossing." In: *Theoretical Computer Science* 560 (2014). Theoretical Aspects of Quantum Cryptography – celebrating 30 years of BB84, pp. 7–11. ISSN: 0304-3975. DOI: https://doi.org/10.1016/j.tcs.2014.05.025.

[Boy08] Robert W. Boyd. *Nonlinear Optics, Third Edition*. 3rd. USA: Academic Press, Inc., 2008. ISBN: 0123694701.

[Cav09] E. G. Cavalcanti et al. "Experimental criteria for steering and the Einstein-Podolsky-Rosen paradox." In: *Phys. Rev. A* 80 (3 Sept. 2009), p. 032112. DOI: 10.1103/PhysRevA.80.032112.

[Coh19] Claude Cohen-Tannoudji, Bernard Diu, and Franck Laloë. *Band 1 Quantenmechanik*. Berlin, Boston: De Gruyter, 2019. ISBN: 978-3-110-63873-8. DOI: doi:10.1515/9783110638738.

[Deq21] Daniele Dequal et al. "Feasibility of satellite-to-ground continuous-variable quantum key distribution." In: *npj Quantum Information* 7.1 (Jan. 2021), p. 3.

[Dix14] A R Dixon and H Sato. "High speed and adaptable error correction for megabit/s rate quantum key distribution." In: *Scientific Reports* 4.1 (Dec. 2014), p. 7275.

[Dua00] Lu-Ming Duan et al. "Inseparability Criterion for Continuous Variable Systems." In: *Phys. Rev. Lett.* 84 (12 Mar. 2000), pp. 2722–2725. DOI: 10.1103/PhysRevLett.84.2722.

[Ebe13] Tobias Eberle, Vitus Händchen, and Roman Schnabel. "Stable control of 10 dB two-mode squeezed vacuum states of light." In: *Opt. Express* 21.9 (May 2013), pp. 11546–11553. DOI: 10.1364/OE.21.011546.

[Ein35] A. Einstein, B. Podolsky, and N. Rosen. "Can Quantum-Mechanical Description of Physical Reality Be Considered Complete?" In: *Phys. Rev.* 47 (10 May 1935), pp. 777–780. DOI: 10.1103/PhysRev.47.777.

[Fur12] F. Furrer et al. "Continuous Variable Quantum Key Distribution: Finite-Key Analysis of Composable Security against Coherent Attacks." In: *Phys. Rev. Lett.* 109 (10 Sept. 2012), p. 100502. DOI: 10.1103/PhysRevLett.109.100502.

[Gab10] Christian Gabriel et al. "A generator for unique quantum random numbers based on vacuum states." In: *Nature Photonics* 4.10 (Oct. 2010), pp. 711–715. ISSN: 1749-4893. DOI: 10.1038/nphoton.2010.197.

[Geh13] Tobias Gehring. "Realization of Finite-Size Quantum Key Distribution based on Einstein-Podolsky-Rosen Entangled Light." PhD thesis. 2013.

[Geh15] Tobias Gehring et al. "Implementation of continuous-variable quantum key distribution with composable and one-sided-device-independent security against coherent attacks." In: *Nature Communications* 6.1 (Oct. 2015), p. 8795.

[Geh21] Tobias Gehring et al. "Homodyne-based quantum random number generator at 2.9 Gbps secure against quantum side-information." In: *Nature Communications* 12.1 (Jan. 2021), p. 605. ISSN: 2041-1723. DOI: 10.1038/s41467-020-20813-w.

[Ger05] Christopher C. Gerry and Peter L. Knight. *Introductory Quantum Optics*. 2nd ed. Cambridge University Press, 2005.

[Hag24] Malte Hagemann. "Development of a Tunable and Compact Source of Squeezed States of Light." PhD thesis. 2024.

[Haj23] A. A. E. Hajomer et al. "Squeezed light coexistence with classical communication over 10 km optical fiber." In: *49th European Conference on Optical Communications (ECOC 2023)*. Vol. 2023. 2023, pp. 530–533. DOI: 10.1049/icp.2023.2235.

[Hua15] Duan Huang et al. "Continuous-variable quantum key distribution with 1 Mbps secure key rate." In: *Opt. Express* 23.13 (June 2015), pp. 17511–17519. DOI: 10.1364/OE.23.017511.

[Imp89] R. Impagliazzo, L. A. Levin, and M. Luby. "Pseudo-random generation from one-way functions." In: *Proceedings of the Twenty-First Annual ACM Symposium on Theory of Computing*. STOC '89. Seattle, Washington, USA: Association for Computing Machinery, 1989, pp. 12–24. ISBN: 0897913078. DOI: 10.1145/73007.73009.

[Kas20] Takahiro Kashiwazaki et al. "Continuous-wave 6-dB-squeezed light with 2.5-THz-bandwidth from single-mode PPLN waveguide." In: *APL Photonics* 5.3 (Mar. 2020), p. 036104. ISSN: 2378-0967. DOI: 10.1063/1.5142437.

[Kat02] Kiyoshi Kato and Eiko Takaoka. "Sellmeier and thermo-optic dispersion formulas for KTP." In: *Appl. Opt.* 41.24 (Aug. 2002), pp. 5040–5044. DOI: 10.1364/AO.41.005040.

[Kil11] Wolfgang Killmann and Werner Schindler. *A proposal for: Functionality classes for random number generators*. Accessed: 2024-12-10. 2011.

[Kim02] M. S. Kim et al. "Entanglement by a beam splitter: Nonclassicality as a prerequisite for entanglement." In: *Phys. Rev. A* 65 (3 Feb. 2002), p. 032323. DOI: 10.1103/PhysRevA.65.032323.

[Lar19] Mikkel V. Larsen et al. "Deterministic generation of a two-dimensional cluster state." In: *Science* 366.6463 (2019), pp. 369–372. DOI: 10.1126/science.aay4354.

[Las07] Nico Lastzka and Roman Schnabel. "The Gouy phase shift in nonlinear interactions of waves." In: *Opt. Express* 15.12 (June 2007), pp. 7211–7217. DOI: 10.1364/OE.15.007211.

[Las10] Nico Lastzka. "Numerical modelling of classical and quantum effects in non-linear optical systems." PhD thesis. 2010.

[Lia17] Sheng-Kai Liao et al. "Long-distance free-space quantum key distribution in daylight towards inter-satellite communication." In: *Nature Photonics* 11.8 (Aug. 2017), pp. 509–513.

[Nol22] Sarah Marie Nolte. "Continuous Quantum Random Number Generation with Squeezed Light." 2022.

[Oel16] E. Oelker et al. "Ultra-low phase noise squeezed vacuum source for gravitational wave detectors." In: *Optica* 3.7 (July 2016), pp. 682–685. DOI: 10.1364/OPTICA.3.000682.

[Pir17] Stefano Pirandola et al. "Fundamental limits of repeaterless quantum communications." In: *Nature Communications* 8.1 (Apr. 2017), p. 15043. ISSN: 2041-1723. DOI: 10.1038/ncomms15043.

[Ral99] T. C. Ralph. "Continuous variable quantum cryptography." In: *Phys. Rev. A* 61 (1 Dec. 1999), p. 010303. DOI: 10.1103/PhysRevA.61.010303. URL: https://link.aps.org/doi/10.1103/PhysRevA.61.010303.

[Rei89] M. D. Reid. "Demonstration of the Einstein-Podolsky-Rosen paradox using nondegenerate parametric amplification." In: *Phys. Rev. A* 40 (2 July 1989), pp. 913–923. DOI: 10.1103/PhysRevA.40.913.

[Sam12] Aiko Samblowski. "State Preparation for Quantum Information Science and Metrology." PhD thesis. 2012.

[Sar90] F Sarvar, NJ Poole, and PA Witting. "PCB glass-fibre laminates: Thermal conductivity measurements and their effect on simulation." In: *Journal of electronic materials* 19.12 (1990), pp. 1345–1350.

[Sch07] Franz Schwabl. *Quantum Mechanics*. Springer, 2007. ISBN: 978-3-540-71932-8.

[Sch18] Axel Schönbeck, Fabian Thies, and Roman Schnabel. "13 dB squeezed vacuum states at 1550 nm from 12 mW external pump power at 775 nm." In: *Opt. Lett.* 43.1 (Jan. 2018), pp. 110–113. DOI: 10.1364/OL.43.000110.

[She85] R. M. Shelby, M. D. Levenson, and P. W. Bayer. "Guided acoustic-wave Brillouin scattering." In: *Phys. Rev. B* 31 (8 Apr. 1985), pp. 5244–5252. DOI: 10.1103/PhysRevB.31.5244.

[Sho94] P.W. Shor. "Algorithms for quantum computation: discrete logarithms and factoring." In: *Proceedings 35th Annual Symposium on Foundations of Computer Science*. 1994, pp. 124–134. DOI: 10.1109/SFCS.1994.365700.

[Smi16] Arlee V. Smith, Jesse J. Smith, and Binh T. Do. *Thermo-optic and thermal expansion coefficients of RTP and KTP crystals over 300-350 K*. 2016. arXiv: 1607.03964.

[Sta] National Institute of Standards and Technology. *Thermal Conductivity of Selected Materials*. Accessed: 2024-06-25. URL: https://srd.nist.gov/NSRDS/NSRDS-NBS-8.pdf.

[Sul22] I Suleiman et al. "40 km fiber transmission of squeezed light measured with a real local oscillator." In: *Quantum Science and Technology* 7.4 (July 2022), p. 045003. DOI: 10.1088/2058-9565/ac7ba1.

[Sym11] T. Symul, S. M. Assad, and P. K. Lam. "Real time demonstration of high bitrate quantum random number generation with coherent laser light." In: *Applied Physics Letters* 98.23 (June 2011), p. 231103. ISSN: 0003-6951. DOI: 10.1063/1.3597793.

[Tak20] Naoya Takefushi et al. "GAWBS phase noise characteristics in multi-core fibers for digital coherent transmission." In: *Opt. Express* 28.15 (July 2020), pp. 23012–23022. DOI: 10.1364/OE.399202.

[Tak23] Kan Takase et al. "Gottesman-Kitaev-Preskill qubit synthesizer for propagating light." In: *npj Quantum Information* 9.1 (Oct. 2023), p. 98. ISSN: 2056-6387. DOI: 10.1038/s41534-023-00772-y.

[Tav20] A.A. Tavleev et al. "Determination of Sound Speed in Optical Fibers Based on the Stimulated Mandelstam-Brillion Scatering Effect." In: *Sensors & Transducers* 247 (Dec. 2020).

[Toh19] Benedict Tohermes. "Continuous Quantum Random Number Generation." 2019.

[Toh24] Benedict Tohermes, Sophie Verclas, and Roman Schnabel. "Directly measured squeeze factors over GHz bandwidth from monolithic ppKTP resonators." In: Submitted to New Journal of Physics (2024). DOI: https://doi.org/10.48550/arXiv.2412.03221.

[Urs07] R Ursin et al. "Entanglement-based quantum communication over 144 km." In: *Nature Physics* 3.7 (July 2007), pp. 481–486.

[Ver21] Sophie R. Verclas. "Fiber-based Distribution of Quantum States for Quantum Key Distribution." 2021.

[Ver25] Sophie Verclas et al. "Fiber distribution of phase-stabilized GHz-bandwidth squeezed vacuum states of light between two buildings." In: Submitted to Optica (May 2025).

[Wal08] D. F. Walls and Gerard J. Milburn. *Quantum Optics*. Springer, 2008. ISBN: 978-3-540-28573-1.

[Wal16] Nathan Walk et al. "Experimental demonstration of Gaussian protocols for one-sided device-independent quantum key distribution." In: *Optica* 3.6 (June 2016), pp. 634–642. DOI: 10.1364/OPTICA.3.000634.

[Wan17] Yajun Wang et al. "Determination of blue-light-induced infrared absorption based on mode-matching efficiency in an optical parametric oscillator." In: *Scientific Reports* 7.1 (Feb. 2017), p. 41405. ISSN: 2045-2322. DOI: 10.1038/srep41405.

[Wis07] H. M. Wiseman, S. J. Jones, and A. C. Doherty. "Steering, Entanglement, Nonlocality, and the Einstein-Podolsky-Rosen Paradox." In: *Phys. Rev. Lett.* 98 (14 Apr. 2007), p. 140402. DOI: 10.1103/PhysRevLett.98.140402.

[Yuk08] Mitsuyoshi Yukawa et al. "Experimental generation of four-mode continuous-variable cluster states." In: *Phys. Rev. A* 78 (1 July 2008), p. 012301. DOI: 10.1103/PhysRevA.78.012301.

[Zha21] Wenhui Zhang et al. "Precise control of squeezing angle to generate 11 dB entangled state." In: *Opt. Express* 29.15 (July 2021), pp. 24315–24325. DOI: 10.1364/OE.428501.

[Zha22] Wei Zhang et al. "A device-independent quantum key distribution system for distant users." In: *Nature* 607.7920 (July 2022), pp. 687–691.

[Zhe19] Ziyong Zheng et al. "6 Gbps real-time optical quantum random number generator based on vacuum fluctuation." In: *Review of Scientific Instruments* 90.4 (Apr. 2019), p. 043105. ISSN: 0034-6748. DOI: 10.1063/1.5078547.

[Zho20] Han-Sen Zhong et al. "Quantum computational advantage using photons." In: *Science* 370.6523 (2020), pp. 1460–1463. DOI: 10.1126/science.abe8770.

[Zho23] Lai Zhou et al. "Twin-field quantum key distribution without optical frequency dissemination." In: *Nature Communications* 14.1 (Feb. 2023), p. 928. ISSN: 2041-1723. DOI: 10.1038/s41467-023-36573-2.

Acknowledgments

Every PhD thesis is a massive undertaking with lots of obstacles on the way towards its completion. Some of them are cleared easily by clever thinking or putting in enough work, at times however it can seem like they are insurmountable and you are just banging your head against a brick wall. When I encountered one of these huge roadblocks the prospect of continuing often seemed daunting. In these moments I was extremely lucky to have support from the awesome people around me to help me progress when feeling stuck on one of those roadblocks, be it with a better approach towards clearing it, being there to vent the frustration, or motivating me to just keep getting at it. Because with some brick wall problems, all you can do is keep banging your head against it until it breaks (the wall, not the head). Here I want to take the time to thank all those who supported me in finishing this thesis. A few of them I want to thank by name:

Professor Roman Schnabel for providing me the opportunity to work on such an intriguing topic. Your door was always open for me to get advice on how to best proceed with the project.

Sophie Verclas for many hours of working in the lab together during her master's and PhD time and later continuing the experiment, as well as Sarah Nolte, who joined the project as a master's student in between. Working together, even remote as it was, was immensely motivating especially during the COVID-time.

My family who supported me over the entire time of my studies and who where always understanding of how time consuming the work was.

Mikhail Korobko for help on interpreting my results, preparing for conferences and writing this thesis. Your advice was invaluable, be it about the intricacies of quantum mechanics or how to put food on my plate correctly.

Julian Gurs, Jonas Rittmeyer, and Max Hachmann for many an evening after work spent discussing project roadblocks or intriguing project ideas, and pushing me to keep banging my head against those metaphorical walls, as well as Stephan Grebien for being my data post-processing discussion partner.

Alexander Franke, Maik Schröder, Pascal Gewecke, and Justin Hohmann who were great company all the way from the start of our master's to the end of our PhDs.

Jascha Zander, Axel Schönbeck, and Jan Südbeck for showing me the ropes of handling squeezers and taking a look when nothing seemed to work.

And many thanks to the rest of the group for proofreading and letting me experience the wonderful working atmosphere during my thesis! My time working with you has truly been a pleasure!

Eidesstattliche Versicherung

Hiermit versichere ich an Eides statt, die vorliegende Dissertationsschrift selbst verfasst und keine anderen als die angegebenen Hilfsmittel und Quellen benutzt zu haben.

Sofern im Zuge der Erstellung der vorliegenden Dissertationsschrift generative Künstliche Intelligenz (gKI) basierte elektronische Hilfsmittel verwendet wurden, versichere ich, dass meine eigene Leistung im Vordergrund stand und dass eine vollständige Dokumentation aller verwendeten Hilfsmittel gemäß der Guten wissenschaftlichen Praxis vorliegt. Ich trage die Verantwortung für eventuell durch die gKI generierte fehlerhafte oder verzerrte Inhalte, fehlerhafte Referenzen, Verstöße gegen das Datenschutz- und Urheberrecht oder Plagiate.

Hamburg, den _____

_____

Unterschrift der Doktorandin / des Doktoranden